DISS. ETH No. 27648

DEVELOPMENT OF TECHNIQUES FOR NEUROIMAGING AT NANOSCALE

A thesis submitted to attain the degree of

Doctor of Sciences of ETH ZURICH

(Dr. sc. ETH Zürich)

Presented by

HUNG TRI TRAN

M.Sc. in Material Science and Engineering, Gwangju Institute of Science and Technology (GIST), Republic of Korea

Born on 23.04.1990

Citizen of the Socialist Republic of Vietnam

Accepted on the recommendation of:

Prof. Dr. Gebhard F. X. Schertler, examiner

Prof. Dr. Marco Stampanoni, co-examiner

Dr. Celestino Padeste, co-examiner

Prof. Dr. Takashi Ishikawa, scientific advisor

2021

Acknowledgements

This work would not have been possible without the help and support of great people. First of all, I would like to express my gratitude and appreciation to my doctoral advisor, Prof. Dr. Gebhard F.X. Schertler for giving me opportunity to be his PhD student and conduct this research at Paul Scherrer Institute. He always takes good care of his students and tries to support them with the best conditions to finish their studies. He also shares with us his visions and gives us valuable advice, not only for ongoing research but also for our future, our career. I also would like to thank Dr. Oliver Bunk for his financial support for my project so I could finish it in extended time. I would like to thank Dr. Sarah Shahmoradian for her great idea to initiate the project and plan the experiments. Especially, in the beginning, she gave my work a clear direction. I would also like to deeply thank my scientific supervisor Prof. Takashi Ishikawa for his mentorship and constant support. He is always thoughtful, open-minded in discussions and gave me best support whenever I needed help or advice. Especially, I would like to extend my most gratitude to Dr. Celestino Padeste for tremendous help and supervision. He is very patient in guiding me though my research step-by-step from the beginning with his great scientific experience and knowledge. I also enjoy discussion with him since he always provides me with the encouragement and freedom to test my own ideas, and with suggestions to overcome many obstacles. I would also like to thank my scientific committee member, Prof. Marco Stampanoni for providing me great comments, guidance and support during my PhD study. I would like to thank Prof. G.V. Shivashankar for providing me great support, suggestions and best conditions to finish my research at Laboratory for Nanoscale Biology. I am very thankful to Dr. Vitaliy Guzenko, Dario Theodor Marty, Christopher Dennis Wild and Konrad Vogelsang at the Laboratory for Micro-and Nanotechnology for their great support and introduction for me to use the special equipment in their laboratory. They provided constant maintenance and quick response to my questions and problems and they helped me in particular experiments. I would like to thank Dr. Philipp Berger for his supervision and support for my cell culture as well as for scientific discussions. I also would like to thank Dr. Wilma van de Berg and her team (Amsterdam UMC, Vrije

Universiteit Amsterdam, Amsterdam, Netherlands) for a great collaboration. She prepared and provided the valuable biological samples for our research and her expertise in neuroscience. I would like to thank Dr. Mirko Holler, Dr. Esther H. R. Tsai, Dr. Ana Diaz, Dr. Manuel Guizar-Sicairos, and Dr. Joerg Raabe for a great collaboration in the human brain X-ray imaging project. They developed the Cryo-ptychographic X-ray computed tomography method at Paul Scherrer Institute and contributed significantly to my project by performing the measurement, imaging of my samples. I also would like to extend my gratitude to Dr. Miriam Lucas at ScopeM (ETH) for her collaboration in the patterning project. She helped us to prepare, process and analyze my delicate samples by freeze substitution, Focus Ion Beam – Scanning Electron Microscopy and Serial sectioning – Transmission Electron Microscopy for ultrastructural imaging. I would like to thank Prof. Dr. Eline Pecho-Vrieseling and Dr. Margarita Dinamarca Ceballos (University of Basel) for a collaboration to support the culturing of primary neurons on my platforms. I am very much thankful to my colleagues at Laboratory for Nanoscale Biology and Laboratory of Biomolecular Research for supporting me to carry my daily experiments and for great working environment.

Last but not least, I would also like to extend my gratitude towards my family and my wife for their patience, love, belief and support for all the long period of time that I am away from home.

Villigen, 28.04.2021

Abstract

A wide range of diseases is associated with alterations of the brain morphology. Multiscale three-dimensional visualization of continuous volumes of unstained brain tissue is important to gain insight to pathologically relevant processes of neurological diseases.

Many pathological processes in neurodegenerative disorders affect myelinated axons, which are a critical part of the neuronal circuitry. Cryo-ptychographic X-ray computed tomography (cryo-PXCT) in the multi-keV energy range is an emerging technology, which provides phase contrast at high sensitivity, allowing label-free and non-destructive three-dimensional imaging of relatively large continuous volumes of tissue. The first part of this thesis reports a pipeline for cryo-PXCT of hydrated and unstained biological human brain tissue of volumes beyond what is typical for X-ray imaging, combined with complementary methods. Four samples of a Parkinson's diseased human brain and five control samples from a non-diseased human brain were imaged using cryo-PXCT. In both cases, specific features were distinguished, such as neuromelanin-containing neurons, lipid and melanic pigments, blood vessels and red blood cells, and nuclei of other brain cells. In the diseased samples, several swellings containing dense granular material were observed, which were resembling clustered vesicles between the myelin sheaths arising from the cytoplasm of the parent oligodendrocyte, rather than the axoplasm. The pathological relevance of such swollen axons in adjacent tissue sections was further investigated by immunofluorescence microscopy for phosphorylated alpha-synuclein. Since cryo-PXCT is non-destructive, the large dataset volumes were used to guide further investigation of such swollen axons by correlative electron microscopy and immunogold labeling post X-ray imaging, a possibility demonstrated for the first time. Interestingly, protein antigenicity and ultrastructure of the tissue were preserved after the X-ray measurement. As many pathological processes in neurodegeneration affect myelinated axons, this work sets an unprecedented foundation for studies addressing axonal integrity and disease-related changes in unstained brain tissues.

The extreme complexity of the human brain prevents performing precise analysis of specific components of neuronal networks, for example, of the individual neurons' interactions in specified circuits. The second part of this thesis reports on the development of a novel compartmentalized neuronal co-culture platform allowing simulation of parts of neuronal networks with higher variable control. Polymer microstructures were fabricated on top of sapphire discs, which can direct the outgrowth of neurites originating from two distinct groups of neurons growing in different compartments. This was demonstrated using two populations of neurons expressing either EGFP or mCherry, which also facilitates the analysis of the specific interactions between two sets of cells. The design of device permits direct observation of neuritic processes within microchannels by optical microscopy with high spatial and temporal resolution to investigate the response of neurites projections to the guidance cues. Furthermore, the cell culture platform is compatible with high-pressure freezing. This allows cryo-preservation of reconstructed neuronal networks at near-native vitreous state for high resolution analysis by electron microscopy. Following freeze substitution, it is possible to process the resin-embedded neuronal networks via conventional methods for ultrastructural imaging via electron microscopy. Several key features of the embedded neuronal networks, including mitochondria, synaptic vesicles, axonal terminals, microtubules, with well-preserved ultrastructures were observed at high resolution using Focused Ion Beam – Scanning Electron Microscopy (FIB-SEM) and Serial sectioning - Transmission Electron Microscopy (TEM). These results demonstrate the compatibility of the platforms with both optical microscopy and electron microscopy. For future studies, the presented platform can be extended to disease models to allow investigating neurodegenerative processes at the nanoscale as well as pharmacological testing and drug screening.

In summary, the techniques for neuroimaging reported in this thesis can be considered as essential tools for investigating the ultrastructure of sub-cellular processes within neuronal networks in normal and disease conditions.

Zusammenfassung

Viele neurologische Erkrankungen sind mit morphologischen Veränderungen von Gehirnstrukturen verbunden. Die dreidimensionale Visualisierung kontinuierlicher Volumina von nicht spezifisch angefärbtem Hirngewebe über mehrere Grössenskalen ist wichtig, um Einblicke in pathologisch relevante Prozesse dieser Erkrankungen zu erhalten.

Pathologische Prozesse bei neurodegenerativen Erkrankungen betreffen oft myelinisierte Axone, welche zentrale Bestandteile der neuronalen Schaltkreise sind. Die ptychographische Röntgen-Computertomographie bei cryo-Temperaturen (cryo-ptychographic X-ray computed tomography, cryo-PXCT) im Energiebereich von mehreren keV ist ein neuartiges und vielversprechendes bildgebendes Verfahren, welches Phasenkontrast-Information bei hoher Empfindlichkeit liefert. Es ermöglicht eine markierungs- und zerstörungsfreie dreidimensionale Abbildung relativ großer kontinuierlicher Proben-Volumina, z.B. von Gewebeproben. Der erste Teil dieser Arbeit beschreibt eine Pipeline für cryo-PXCT von hydratisiertem und nicht angefärbtem biologischem menschlichem Gehirngewebe, in Kombination mit komplementären Methoden. Vier Proben aus an Parkinson erkranktem menschlichem Gehirn und fünf Kontrollproben eines gesunden Gehirns wurden mittels cryo-PXCT abgebildet. In beiden Fällen konnten Gehirn-spezifische Merkmale identifiziert werden, wie Neuromelanin-haltige Neuronen, Lipid- und Melaninpigmente, Blutgefäße und rote Blutkörperchen sowie Zellkerne anderer Gehirnzellen. In den Proben von Erkrankten wurden mehrere Schwellungen beobachtet, die dichtes, körniges Material enthielten. Diese erschienen als gruppierte Vesikel zwischen den Myelinhüllen, die vermutlich eher aus dem Zytoplasma der ursprünglichen Oligodendrozyten stammten als aus dem Axoplasma. Die pathologische Relevanz dieser gequollenen Axone in benachbarten Gewebeschnitten wurde für die Immunfluoreszenzmikroskopie von phosphoryliertem Alpha-Synuclein in Kombination mit multispektraler Bildgebung weiter untersucht. Da cryo-PXCT zerstörungsfrei ist, konnten die Bild-Daten der grossen Probenvolumina verwendet werden, um die geschwollenen Axone durch anschliessende Immunogold-Markierung und die korrelative Elektronenmikroskopie zu lokalisieren. Dieses Verfahren wurde hier erstmals erfolgreich angewendet. Interessanterweise blieben die Protein-Antigenität und die Ultrastruktur des Gewebes nach der Röntgenmessung erhalten. Da viele pathologische Prozesse bei der Neurodegeneration myelinisierte Axone betreffen, bildet diese Arbeit eine wegweisende Grundlage für zukünftige

Studien, die sich mit der Integrität der Axone und krankheitsbedingten Veränderungen in nicht angefärbten Hirngeweben befassen.

Die extreme Komplexität des menschlichen Gehirns verhindert die genaue Analyse bestimmter Komponenten neuronaler Netzwerke, beispielsweise der Interaktionen einzelner Neuronen in bestimmten Schaltkreisen. Der zweite Teil dieser Arbeit berichtet über die Entwicklung einer neuartigen in Kompartimente unterteilten Plattform für Co-Kulturen von Nervenzellen, welche die Simulation von Teilen neuronaler Netzwerke unter Kontrolle mehrerer Variablen ermöglicht. Auf Saphirsubstraten wurden Polymermikrostrukturen hergestellt, die das Wachstum von Neuriten leiten können. Diese stammen zum Beispiel von zwei unterschiedlichen Gruppen von Neuronen, die in den verschiedenen Kompartimenten auf dem Saphir-Träger wachsen. Dies wurde unter Verwendung von zwei Populationen von Neuronen demonstriert, welche entweder EGFP oder mCherry exprimieren, ein Ansatz, der auch die Analyse der spezifischen Wechselwirkungen zwischen zwei Populationen von Zellen vereinfachen wird. Das Design der Substrate ermöglicht die direkte Beobachtung neuronaler Prozesse innerhalb von Mikrokanälen durch optische Mikroskopie mit hoher räumlicher und zeitlicher Auflösung, um die Reaktion von Neuriten-Ausläufern auf externe Signale zu untersuchen. Darüber hinaus ist die Zellkulturplattform mit Hochdruckgefrierprozessen kompatibel. Dies ermöglicht die Cryo-Konservierung rekonstruierter neuronaler Netzwerke in einem nahezu ursprünglichen Zustand, und die weitere Bearbeitung der Proben für die hochauflösende Analyse mittels Elektronenmikroskopie. Nach einer Gefriersubstitution ist es möglich, die in Harz eingebetteten neuronalen Netzwerke mit herkömmlichen Methoden für die Untersuchung der Ultrastruktur mittels Elektronenmikroskopie zu verarbeiten. Mehrere Schlüsselmerkmale der eingebetteten neuronalen Netzwerke, einschließlich Mitochondrien, synaptischer Vesikel, axonaler Terminals und Mikrotubuli mit gut erhaltenen Ultrastrukturen konnten mit hoher Auflösung abgebildet werden. Zum einen erfolgte dies mittels sequenziellem Abtrag mit einem fokussierten Ionenstrahl und anschliessender Rasterelektronenmikroskopie (FIB-SEM), und zum anderen durch serielles Schneiden mittels Ultra-Mikrotom und anschliessende Transmissionselektronenmikroskopie (TEM). Diese Ergebnisse demonstrieren die Kompatibilität der Plattform mit der optischen Mikroskopie wie auch mit der Elektronenmikroskopie. Für künftige Studien könnte die vorgestellte Plattform für die Untersuchung von Krankheitsmodellen erweitert werden. Dies würde die

Untersuchung neurodegenerativer Prozesse im Nanobereich sowie pharmakologische Tests und Wirkstoff-Screenings ermöglichen.

Zusammenfassend können die in dieser Arbeit beschriebenen Techniken als wesentliche Instrumente zur Untersuchung der Ultrastruktur subzellulärer Prozesse in neuronalen Netzwerken unter normalen und Krankheitsbedingungen angesehen werden.

Abbreviations

AD	Alzheimer's disease
ALS	amyotrophic lateral sclerosis
aSyn	alpha-synuclein
cryo-PXCT	Cryo-ptychographic X-ray computed tomography
DMA	Dystrophic myelinated axon
FIB-SEM	Focused Ion Beam – Scanning Electron Microscopy
HD	Huntington's disease
MC	methylcellulose
MSA	multiple systems atrophy
OMNY	tOMography Nano crYo
PD	Parkinson's diseased
SEM	Scanning Electron Microscopy
SNc	substantia nigra pars compacta
SNpc	substantia nigra pars compacta
SWiA	swollen in axoplasm
SWiM	swollen in myelin
TEM	Transmission electron microscopy
UA	uranyl acetate
PDMS	Polydimethylsiloxane

Contents

Acknowledgements ..... **i**

Abstract ..... **iii**

Zusammenfassung ..... **v**

Abbreviations ..... **viii**

List of Figures ..... **xi**

List of Tables ..... **xii**

Chapter 1 General Introduction **1**

Chapter 2 Abnormalities in Axonal Architecture of Frozen-Hydrated Human Brain using Label-Free X-Ray Nanotomography Imaging **9**

2.1 Introduction 9

2.2 Methods 13

2.2.1 Human Postmortem Brain Tissue Samples 13

2.2.2 Safety Considerations for Tissue Handling 14

2.2.3 Tissue Preparation for Cryo-PXCT Imaging 14

2.2.4 Cryo-PXCT Data Collection and Tomogram Reconstruction 16

2.2.5 Immuno-Electron Microscopy After Cryo-PXCT Imaging 17

2.2.6 3D Color Segmentation and Statistical Analysis of Dystrophic Myelinated Axons (DMAs) 18

2.3 Results 19

2.3.1 Cryo-PXCT Imaging 19

2.3.2 3-D Segmentation and Quantification 22

2.3.3 Correlative Electron Microscopy 34

2.4 Discussion 44

2.5 Conclusion 48

Chapter 3 A Compartmentalized Neuronal Cell-Culture Platform Compatible with Cryo-Fixation by High-pressure Freezing for Ultrastructural Imaging **49**

3.1 Introduction 49
3.2 Methods 52
3.2.1 Fabrication of microstructures on sapphire discs 52
3.2.2 Fabrication of the PDMS chamber 53
3.2.3 Cell cultures 54
3.2.4 Immunostaining 54
3.2.5 Lentivirus production and transfection 55
3.2.6 SEM imaging of neuron cultures 56
3.2.7 High pressure freezing 56
3.2.8 Freeze substitution 56
3.2.9 Ultrastructural imaging 57
3.3 Results 58
3.3.1 Neuron co-culture system: Device concept and fabrication 58
3.3.2 Cell culture 67
3.3.2.1 Culturing PC 12 cells 67
3.3.2.2 Culturing of postnatal hippocampal neurons 69
3.3.2.3 Culturing of embryonic striatal neurons 71
3.3.3 Ultrastructural imaging 74
3.3.3.1 Focus Ion Beam – Scanning Electron Microscopy (FIB-SEM) 74
3.3.3.2 Serial sectioning - Transmission Electron Microscopy (TEM) 75
3.4 Discussion 78
3.5 Conclusion 81
Chapter 4 General conclusion 83
Supplementary Material 89
References 94

List of Figures

Figure 1.1: Multiscale hierarchical organization of brain networks. 2

Figure 1.2: Complex neural circuit networks in the human brain. 3

Figure 1.3: Myelinated axons in a nervous system. 4

Figure 1.4: A typical compartmentalized neuronal culture platform. 6

Figure 2.1: Electron microscopy reveals Lewy neurites in substantial nigra of PD human brain contain vesicular structures and disrupted cytoskeletal elements. 10

Figure 2.2: tOMography Nano crYo (OMNY) instrument for cryo-PXCT. 11

Figure 2.3: Human brain imaged by cryo-PXCT using OMNY. 21

Figure 2.4: Segmentation of cellular features in human brain tissue tomograms. 24

Figure 2.5: Tissue components in 3D color-segmented cryo-PXCT datasets of non-demented control human brain. 26

Figure 2.6: Tissue components in 3D color-segmented cryo-PXCT tomograms of PD human brain. 27

Figure 2.7: Dystrophic myelinated axons (DMAs) by cryo-PXCT in PD human brain. 28

Figure 2.8: 3D color representations of DMAs in Parkinson's diseased human brain by cryo-PXCT. 29

Figure 2.9: Schematic model of different types of dystrophic myelinated axons (DMAs) as observed by cryo-PXCT in Parkinson's diseased human brain. 31

Figure 2.10: Type and abundance of DMA observed in cryo-PXCT tomograms of Parkinson's diseased human brain. 32

Figure 2.11: Measurements of DMAs in cryo-PXCT tomograms of Parkinson's diseased human brain. 33

Figure 2.12: Simplified schematic workflow for tissue imaging by cryo-PXCT and downstream post-processing. 36

Figure 2.13: Electron microscopy of ultrathin tissue sections post cryo-PXCT imaging of non-demented control human brain. 38

Figure 2.14: Immuno-electron microscopy of ultrathin tissue sections post cryo-PXCT imaging of non-demented control human brain. 40

Figure 2.15: Immuno-electron microscopy of ultrathin tissue sections post cryo-PXCT imaging of PD human brain. 42

Figure 3.1: Schematic of the microstructured sapphire discs used as cell-growth substrates. 59

Figure 3.2: A sample holder to improve spin-coating process on the 6mm sapphire discs. 60

Figure 3.3: Defects of the structures. 61

Figure 3.4: Formation of edge beads on the edge of sapphire disc after drying the photoresist thin film. 61

Figure 3.5: Removing edge beads manually by aceton-dipped cotton swap. 62

Figure 3.6: Parallel ridges structures with multiple designs on sapphire discs. .. 62

Figure 3.7: Schematic illustration of an assembled device allowing compartmentalized co-culture of different cell populations. 64

Figure 3.8: Pictures of an assembled PDMS device. 65

Figure 3.9: Experimental workflow for ultrastructural imaging. 66

Figure 3.10: Differentiation of PC12 cells on collagen coated sapphire disc. 68

Figure 3.11: Live imaging of 5 DIV differentiated PC12 growing on a structured and collagen coated sapphire disc inside PDMS chamber. 68

Figure 3.12: Live imaging of differentiated PC12 cells growing on a structured sapphire disc coated with collagen type IV. 69

Figure 3.13: Live imaging of 14 DIV postnatal hippocampal neurons growing on a structured and Poly-L-Lysine coated sapphire disc inside PDMS chamber. 70

Figure 3.14: Live imaging of 21 DIV postnatal hippocampal neurons growing on a structured and Poly-L-Lysine coated sapphire disc. 71

Figure 3.15: 15 DIV striatal neurons growing on glass coverslips. 72

Figure 3.16: 14 DIV embryonic striatal neurons which were growing on Poly-L-Lysine coated-patterned sapphire disc. 73

Figure 3.17: Ultrastructural analysis of resin-embedded embryonic striatal neurons by FIB-SEM. 75

Figure 3.18: Light microscope of embedded neuronal networks in Epon resin block. 76

Figure 3.19: Ultrastructural analysis of resin-embedded embryonic striatal neuron obtained by serial sectioning – TEM. 77

Figure 4.1: An automated tape-collecting ultramicrotome system. 85

List of Tables

Table 2.1: Imaging parameters and characteristics of biological samples imaged by cryo-PXCT using OMNY. 20

Table 2.2: Clinical and pathological characteristics of brain donors. 20

Chapter 1 General Introduction

"*The brain is the last and grandest biological frontier, the most complex thing we have yet discovered in our universe. It contains hundreds of billions of cells interlinked through trillions of connections. The brain boggles the mind." – James D. Watson, Nobel Laureate and co-discoverer of the structure of DNA*.

The human brain is the largest brain relative to body size of all among primates and mammals in general. It contains approximately 100 billion neurons and 10- to 50-fold more glial cells[1]. Multi-scale visualization of the hierarchical organization of human brain is highly desired in neuroscience. The micro- and nanomorphology of the neuronal network is tightly linked with the brain's functionality, from the macroscopic level, i.e., specialized populations of neurons, to the nanoscopic level, i.e., synaptic connections between individual neurons (**Figure 1.1**). Large-scale, label-free 3D imaging at nanoscale resolution of near-native state tissues can reveal new insights to such hierarchically organized neuronal structures.

The human brain consists of extremely complex neural circuits, wherein interconnected neurons are organized to perform distinct functions (**Figure 1.2**). Neurons communicate via their extensions known as neurites (dendrites or axons). Dendrites are cytoplasmic extensions of neurons which are designed to receive signals from other neurons. Dendrites extend hundred micrometers from the soma and they usually branch extensively into tree-like structures. In addition, they are also studded with small protrusion with various shapes, called dendritic spines, along their length. Axons are long processes emerging from the soma and are involved in transmitting signals to other cells. They are morphologically different from dendrites and can be distinguished by their longer length, non-spiny, untapered and unbranched (at the distal end only when they reach target) shape. Axons are often wrapped in segments of lipid membrane sheaths known as myelin. Myelin sheaths are essentially flattened portions of extensions of the cell membrane of oligodendrocytes in the central

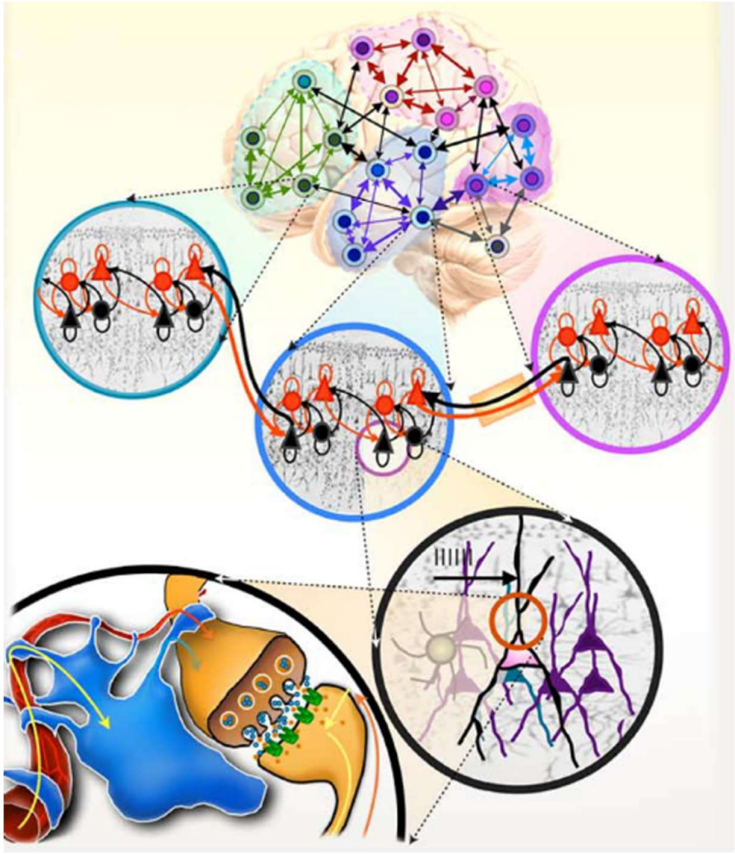

Figure 1.1: Multiscale hierarchical organization of brain networks.

The scheme illustrates the complex organization of the human brain from the macroscopic to the nanoscopic level. Neurons are organized into specialized populations, and their functions are determined by their intrinsic properties and extrinsic connections. These brain areas are well-connected with each other via dense neuronal networks and individual neurons communicate via synaptic connections between them. The synapse dysfunction is the common pathological feature of many neurological diseases. Scheme reprinted from *Park and Friston, 2013*[2].

nervous system or Schwann cells in the peripheral nervous system (**Figure 1.3**). The high lipid content of myelin sheaths encasing the axon serves to enhance conduction velocity[3]. The compact myelin sheath increases the local resistance and enables saltatory conduction by segregation of voltage-gated Na^+ channels at nodes of Ranvier (gaps between adjacent sheaths where the axonal membrane are not wrapped and insulated by myelin) to allow action potential propagation along myelinated fibers[4]. In addition, myelin also provides stabilizing the long-term integrity of axon as well as metabolic support. Oligodendrocytes have been found to supply lactate to adapt to neuronal energy demands through monocarboxylate transporters at the adaxonal membrane of the myelin sheath and on axon[5–7]. Myelinated

axons are a critical part of the neuronal circuitry and constitute approximately 40% of the human brain[8].

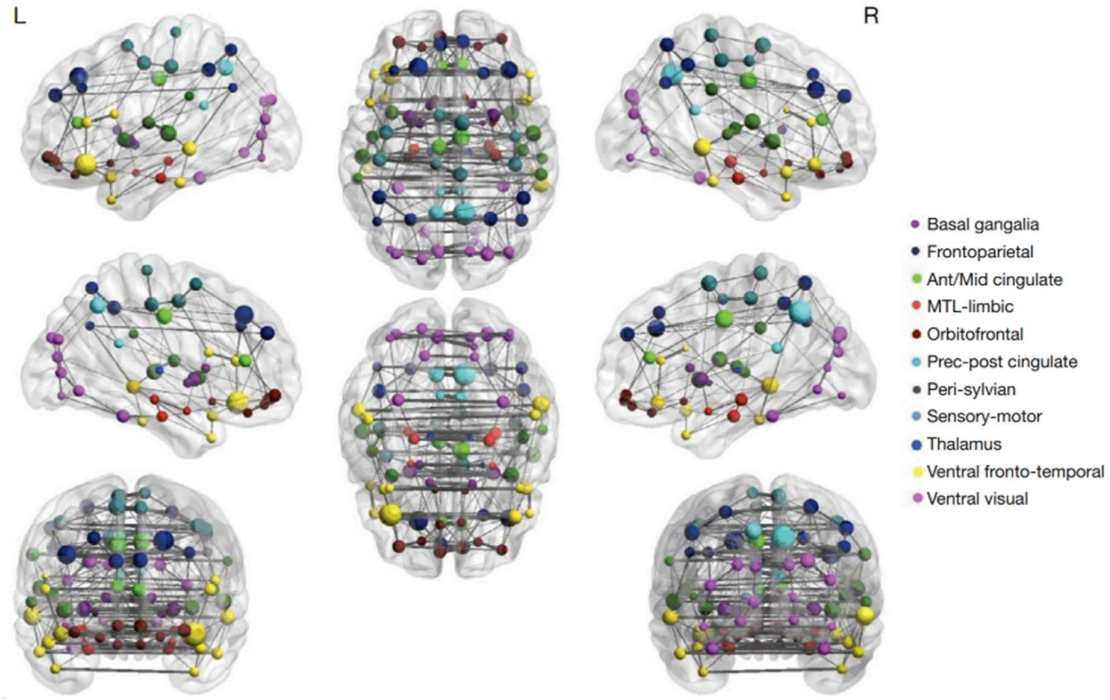

Figure 1.2: Complex neural circuit networks in the human brain.

The scheme shows the large-scale functional organization. The different functional regions of the brain are interconnected by dense neural circuit networks, which are represented by modules (segregated functional subnetworks) and nodes (functional areas). The nodes' sizes represent their connectivity profile. Scheme reprinted from *Menon, 2015*[9].

Neurites, especially myelinated axons, are a critical functional component of brain cells, serving as highways of cross-communication. They relay physical cargo (neurotransmitters) and electrical signals from one neuron to another. Pathologically related aggregation processes within the axons can cause a localized swelling that interferes with normal trafficking[10]. Alzheimer's disease, Parkinson's disease, and multiple sclerosis are a few examples of such diseases[11–15] in which the axonal integrity is affected. The ability to image several axons and their inner contents at once is particularly advantageous when applied to diseased and degenerative brain conditions in which neurites are pathologically involved or affected. Capturing a wide and inclusive view of features in normal and dystrophic axons

within the tissue can permit new insights to the axonal component of pathology in neurodegenerative diseases, which is not well understood.

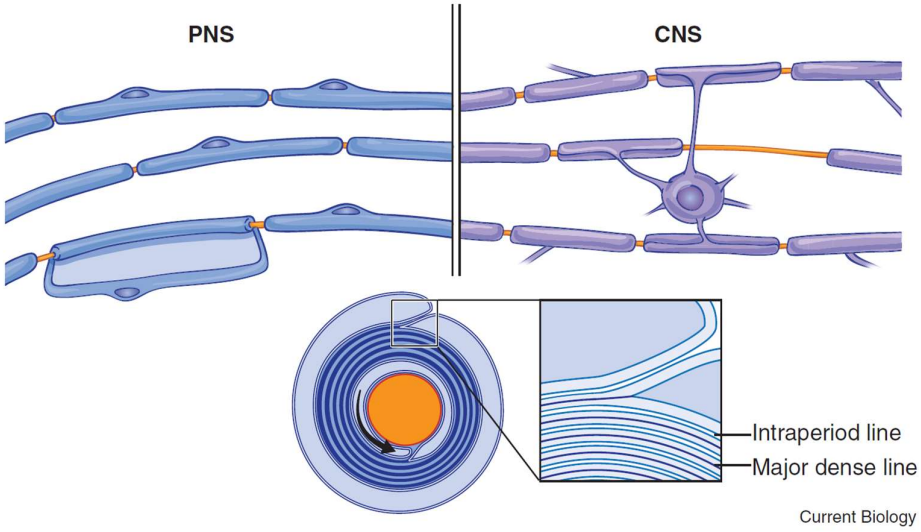

Figure 1.3: Myelinated axons in a nervous system.

Myelin sheaths around axons in the peripheral nervous system (PNS) are formed by Schwann cells and by oligodendrocytes in the central nervous system (CNS). Orange: axons, Purple: oligodendrocytes, Blue: Schwann cells. Scheme reprinted from *Salzer and Zalc, 2016*[16].

Additionally, several human brain disorders, including neurodegeneration diseases such as Alzheimer's [17–19], Huntington's [20–23] and Parkinson's diseases [24–26], have also been attributed to dysfunctions in neural circuitries. Progressive neuronal cell death is thought to be linked in part to abnormal cell-cell communication between subpopulations of neurons in the brain, seen as alterations in synaptic function as well as disrupted intracellular signaling. Particular neuronal subpopulations and specific circuits exhibit selective vulnerability, such as the corticostriatal circuit in Huntington's disease and the nigrostriatal circuit in Parkinson's disease, and the entorhinal cortex and hippocampal CA1 projection neurons in Alzheimer's disease[27]. Non-cell-autonomous and circuit-based mechanisms are important to consider in pathogenesis. For example, the excitation of striatial medium-sized spiny neurons is controlled by a combination of glutamatergic inputs from the neocortex and dopaminergic inputs from the substantia nigra pars compacta[28,29]. The cortical projections exhibit early hyperexcitation in Huntington's disease, and can lead to a toxic convergence of signals onto the striatal

medium-sized spiny neurons, thereby enhancing their vulnerability to the effects of the mutant Huntingtin protein[30].

The extreme complexity of the brain prevents us from visualizing and monitoring individual neurites or the interactions and communication between specific neurons *in vivo.* For example, it is estimated that each substantia nigra pars compacta (SNc) dopaminergic neuron gives rise to 100.000–250.000 synapses at the level of the striatum[31]. Therefore, artificial cell culture systems that can recapitulate central parts of such circuits may mimic a more physiologically-relevant state, and thereby help serve as a platform towards better understanding cellular processes and molecular mechanisms underlying such diseases, towards ultimately developing better therapeutic approaches.

The research reported here focused on two distinct nanoscale imaging techniques to address the above needs for neuroscience: (a) a 3-D imaging approach to investigate tissue samples from different healthy and diseased brains and (b) a neuron co-culture platform to reconstruct neuronal networks *in vitro*. The first approach involves application of cryo-PXCT to analyze human brain samples (Parkinson's diseased and control) and identify novel pathological structures. Cryo-PXCT is a technique pioneered at Paul Scherrer Institut over the past ten years. The method allows imaging of larger volumes (up to tens of µm in size) at high resolution otherwise only possible via destructive techniques. The imaging of such large volumes allowed finding intra-axonal swellings at the nanometer scale in multiple regions of the Parkinson's diseased (PD) brain, which were not present in the control brain. These axonal swellings occur mainly within the myelin sheaths, rather than in the cytosol of the axon itself. This finding calls for a closer look at processes within the myelin sheath for PD, and to the brain cells from which myelin arises (oligodendrocytes), rather than just the neuron itself. Cryo-PXCT is a non-destructive method. This opens the possibility to characterize the same samples again using cross-sectioning and electron microscopy after cryo-PXCT imaging, and allows resolving previously defined regions of interest in the large volume at higher resolution. This could be demonstrated in the present study. Additionally, it was demonstrated that the cellular structures including nuclei and their membranes were not destroyed by the X-ray measurement.

The other approach involves development of a compartmentalized platform for neurons co-culture for ultrastructural imaging. Typically, compartmentalized neuronal culture platforms consist of microfluidic devices that can be assembled on a variety of substrates for neuron cultures, including silicon, glass, quartz, or polystyrene. The microfluidic devices are usually fabricated by replication process with various designs using Polydimethylsiloxane (PDMS) to meet specific needs for *in vitro* experimental approaches. The main components of microfluidic devices are isolated chambers for separately co-culturing of different neuron populations and microchannels to direct the growth of axons and dendrites (**Figure 1.4**). The microchannel structures allow guiding neurites originated from different neuron groups to grow further away from their soma and interact and establish synapse connections within the channels. The platform developed here supports growth of neural cells and allows reconstruction of neuronal circuit *in vitro* to simplify complex nervous system for further studies. It is compatible with both visualizing individual neurites more clearly by light microscopy and enabling for downstream electron microscopy. Moreover, it is possible to pharmacologically manipulate neural cell cultures to develop neurological disease models in the future for better understanding the disease conditions in a physiologically relevant state at ultrastructural level and in order to potentially monitor and detect the diseases at an early stage.

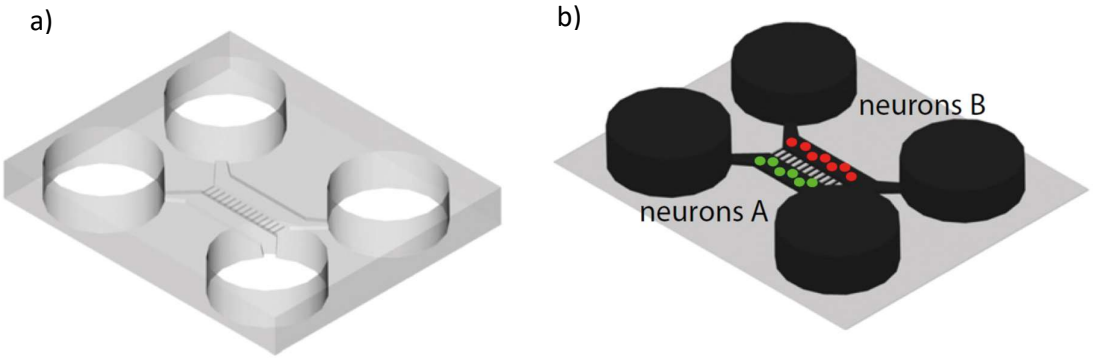

Figure 1.4: A typical compartmentalized neuronal culture platform.

(a) PDMS microfluidic device of separate chambers for isolated plating of different neuron groups. The two compartments are connected through microchannel structures. (b) Microfluidic device assembled on a compatible substrate for neuron cultures. Neurons A and B attach and grow on separated areas and project neurites to microchannels to form synapse connections. The cell culture media is shown in black for visualization. Scheme reprinted from *Taylor, 2010*[32].

The developed imaging techniques as well as the neuronal culture platform will serve as useful tools to overcome major limitations in the neuroscience to study different aspects of nervous system, extending from fundamental understanding of neurobiology to more complicated biological processes in neurological diseases.

Chapter 2 Abnormalities in Axonal Architecture of Frozen-Hydrated Human Brain using Label-Free X-Ray Nanotomography Imaging

This chapter is based on a published paper in *Frontiers in Neuroscience*; *Hung Tri Tran, Esther H. R. Tsai, Amanda J. Lewis, Tim Moors, J. G. J. M. Bol, Iman Rostami, Ana Diaz, Allert J. Jonker, Manuel Guizar-Sicairos, Joerg Raabe, Henning Stahlberg, Wilma D. J. van de Berg, Mirko Holler, Sarah H. Shahmoradian, Front. Neurosci.* ***14****, (2020)*[33].

2.1 Introduction

Parkinson's disease (PD) is a complex neurodegenerative disease, in which the axonal component of pathology is not well understood. While axonal pathology, including swollen (dystrophic) axons and alterations in axonal transport, have been extensively noted in Parkinson's disease patients, animal and cell culture-based models, little is known beyond the facts that they can appear physically swollen, have slower vesicular transport and contain aggregated material including alpha-synuclein (aSyn), beta-synuclein, and gamma-synuclein[34–42]. Correlative light and electron microscopy of Parkinson's diseased human brain tissue sections has recently shown such dystrophic axons, specifically Lewy neurites, to contain vesicular structures, dysmorphic mitochondria and disrupted cytoskeletal elements (**Figure 2.1**)[43]. However, imaging several dystrophic axons and their contained ultrastructures simultaneously is not efficient using electron microscopy alone.

Synchrotron-based X-ray micro-tomography is an imaging technique that can be used to map neural circuits in brain tissue with reported resolutions of down to 1 µm, using heavy-metal staining such as silver nitrate for contrast enhancement and oftentimes plastic- or paraffin-embedding for rigid preservation[44,45]. Phase contrast has also been used in propagation-based X-ray imaging to obtain high-quality 3D images of myelinated axons[46]. However, the resolution in these techniques is insufficient for a detailed morphological characterization of axons. Lens-based X-ray microscopy makes use of X-ray optics for magnification, as in holo-tomography, for example[47]. At the water window, i.e., at photon energies between 281 and 533 eV, carbon-rich structures in biological tissue exhibit a high contrast compared to water. In this way,

biological matter can be imaged in 3D at a resolution of about 30 nm, albeit with a depth limited to a couple of micrometers[48,49].

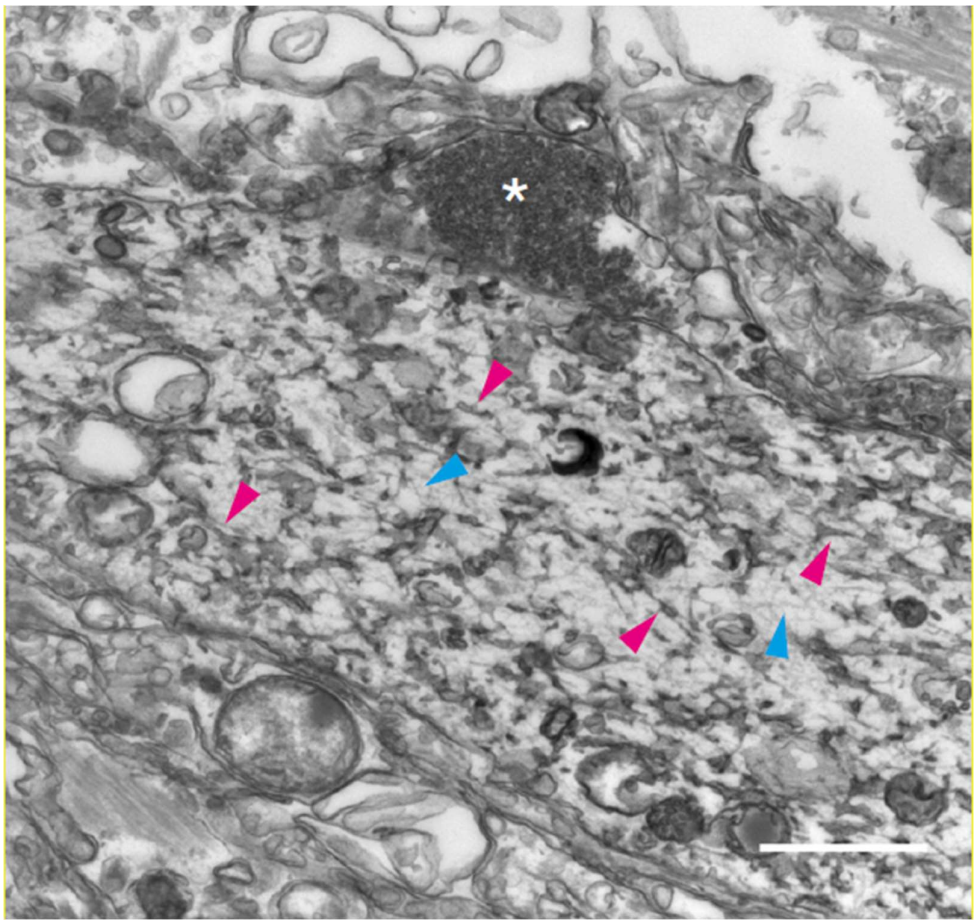

Figure 2.1: Electron microscopy reveals Lewy neurites in substantial nigra of PD human brain contain vesicular structures and disrupted cytoskeletal elements.

Pink arrow heads: Tubulovesicular structures; Blue arrow heads: Filaments and disrupted cytoskeletal elements; White asterisk: Clusters of vesicles. Scale bar: 1 µm. Figure adapted from *Shahmoradian, 2019*[43].

However, for imaging myelinated axons, volumes of several tens of micrometers are required while preserving a high spatial resolution, for which harder X-rays with photon energies above about 2 keV are necessary. Despite the difficulty to fabricate optimally efficient lenses for hard X-rays, lens-based microscopy of neural tissue has been demonstrated[50]. Additionally, propagation-based hard X-ray microscopy can be achieved by using a divergent beam to

produce magnified images[51,52] which allowed resolving myelinated axons within resin-embedded nerves specimens[52,53].

In contrast, ptychographic X-ray computed tomography (PXCT) is a lens-less technique in which spatial resolution is not limited by imaging optics. It currently allows reaching a resolution down to about 15 nm in 3D[54,55] on specimens that exhibit small features with sufficient density contrast. PXCT is an imaging method that employs data collection modes, where a sample is scanned at different positions and orientations through a confined coherent X-ray beam (**Figure 2.2**). In PXCT coherent diffraction patterns in the far field are recorded in a way that consecutive illuminated areas are partially overlapping. Applied iterative phase retrieval algorithms converge in a robust way and can be used to reconstruct the complex-valued transmissivity of the samples[56]. The phase images are aligned and combined[57,58] for 3D tomographic reconstruction of the specimen.

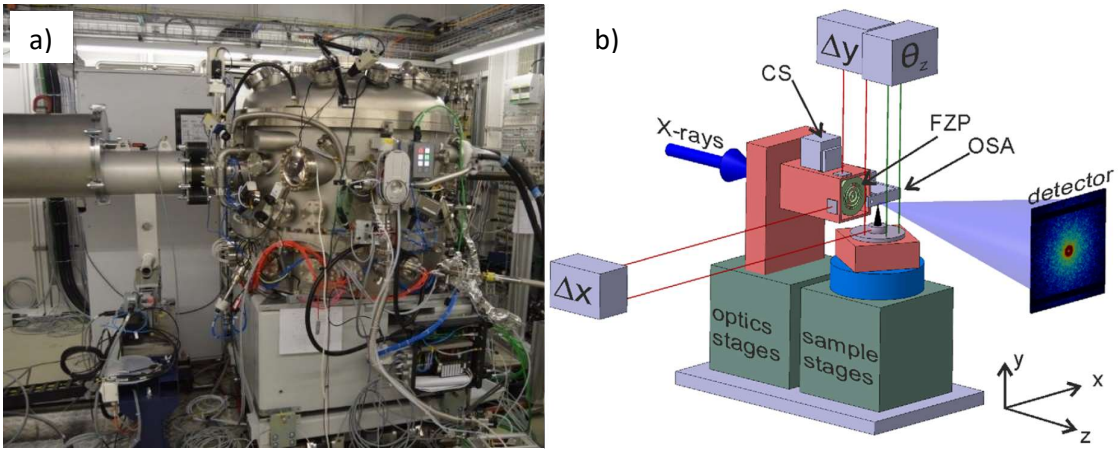

Figure 2.2: tOMography Nano crYo (OMNY) instrument for cryo-PXCT.

(a) Image of OMNY instrument at the cSAXS beamline, PSI; the instrument is placed inside a 110 cm diameter vacuum chamber, which allows minimizing X-ray scattering and absorption. The x-ray beam is coming in from the right; the flight tube with the detector at the end is placed on the left. Image reproduced from www.psi.ch/en/sls/csaxs/endstations. (b) Schematic representation of OMNY instrument setup for tomography. The sample stages allow ptychographic measurements of samples at different rotation angles around the y-axis. CS: central stop; FZP: Fresnel zone plate; OSA: order-sorting aperture; Δx, Δy: relative position of sample and optics, θz: wobble angle of the sample stage. Scheme reprinted from *Holler, 2014*[54].

As density contrast is small in biological samples for hard X-rays, resolution has been typically limited to the 100 nm range in both stained, resin-embedded and frozen- hydrated specimens[59–61]. However, the sensitivity of PXCT is high enough to visualize ultrastructural features in fully hydrated samples without requiring heavy metal staining for contrast purposes, or destruction of material (ion beam milling, sectioning) for accessing tissue depths[61]. These are important factors for enabling multi-scale downstream processing in a relatively minimally perturbed state. The OMNY instrument[62] set up at the Swiss Light Source at Paul Scherrer Institut allows cryo-PXCT measurements of biological samples in cryo-conditions and under vacuum, forming a powerful label-free microscopy technique.

All of the resulting ultrastructural information from cryo-PXCT data can be correlated to electron density, directly interpretable from the grayscale values of the tomographic data, which can be, in turn, related to its local mass density using reasonable assumptions about the stoichiometric composition[59]. This is useful for attributing an identity to each ultrastructural feature within the complex and crowded tissue landscape. Cryo-PXCT at photon energies between about 6 and 8 keV has the ability to provide information across relatively large volumes of unstained tissue, enabling the imaging of multiple cell bodies and the tracking of morphological intracellular changes along the lengths of radiating structures such as cellular extensions; in the case of brain tissue, along the length of neuronal processes.

Using cryo-PXCT, the visualization of tissue contents including myelinated axons at a resolution in the 100 nm range is independent of pre-marking selected features using pigment- based or fluorescent labels[63–66]. This enables a wide and inclusive view of numerous features existing in the tissue, including normal and dystrophic axons, which are otherwise easily missed or unintentionally excluded.

Cryo-PXCT enables the simultaneous visualization of several axons and the subtleties within and throughout each axon that are easily missed unless visualizing a continuous length, i.e., across tens of microns, up to $(100\ \mu m)^3$. Such subtleties include, but are not limited to, disruptions or abnormalities within the myelin sheath wrappings at specific points along the length of the axon, or abnormalities within the axon itself.

Beyond generating a 3D picture of multiple axons and brain cells to recognize pathologically relevant features, cryo-PXCT allows for the tissue to remain intact at the nanoscale after

imaging. This aspect opens up the unique possibility of downstream processing of selected features of interest by higher resolution techniques such as electron microscopy, as also shown here, or gaining biochemical information by different spectroscopic-based imaging approaches, such as Fourier-transform infrared spectroscopy (FTIR), coherent anti-Stokes Raman spectroscopy (CARS), and matrix-assisted laser desorption/ionization mass spectroscopy imaging (MALDI-IMS).

Starting with several chemically fixed, hydrated tissue blocks from a postmortem Parkinson's diseased human brain and from a control/non-demented human brain, we processed and imaged these by cryo-PXCT, followed by cryo-ultramicrotomy and cryo-immunogold labeling and electron microscopy. We thus demonstrate a multi-scale imaging pipeline using cryo-PXCT followed by immuno-electron microscopy, with a cross investigation of pathological features of interest using fluorescence microscopy combined with multispectral imaging.

2.2 Methods

2.2.1 Human Postmortem Brain Tissue Samples

Post-mortem brain tissue samples from Donors A and B (Table 2.2) with clinical diagnosis PD with dementia (PDD) and brain tissue samples from non-demented patients as controls (Donors C-E, Table 2.2) were obtained from the Netherlands Brain Bank (NBB; Table 2.2) and the Normal Aging Brain Collection (Dept. Anatomy and Neurosciences, VUmc), respectively. Tissues were collected using a rapid autopsy protocol (NBB), which was performed by Dr. Wilma D. J. van de Berg (Vrije Universiteit Amsterdam, Amsterdam, Netherlands). Brain tissues from Donors B and D (Table 2.2) were used for cryo-PXCT and electron microscopy studies, while tissues from all donors were used for optical microscopy studies. All protocols of the Netherlands Brain Bank (NBB), Netherlands Institute for Neuroscience, Amsterdam (open access; see text footnote 1), and of the Normal Aging Brain Collection (NABC), VU University Medical Center, Amsterdam, were approved by the Medical Ethical Committee (METC), VU University Medical Center, Amsterdam, the Netherlands. For brain samples and/or bio samples obtained from the NBB, all material has been collected from donors for or from whom a written informed consent for a brain autopsy and the use of the material and clinical information for research purposes was obtained by the NBB. For brain samples obtained from NABC, all material has been collected from donors for or from whom a written informed

consent for an autopsy and the use of the material and clinical information for teaching and research purposes was obtained by the department of Anatomy and Neurosciences, VUmc, the Netherlands. For samples from both brain banks, detailed neuropathological and clinical information was made available, in compliance with local ethical and legal guidelines, and all protocols were approved by the local institutional review board. At autopsy, 0.5 cm-thick adjacent brain slices of the SNpc were collected. Cubes of ~1–2 mm^3 of the ventral part of the SNpc were dissected and fixed for 6 h in a mixture of 2% paraformaldehyde/2.5% glutaraldehyde in 0.15 M cacodylate buffer with 2 mM calcium chloride, pH 7.4 and then washed with PBS. The PD brain donor fulfilled the United Kingdom Parkinson's Disease Society Brain Bank (UK-PDSBB) clinical diagnostic criteria for PD[67]. Neuropathological evaluation was performed on 7 mm formalin-fixed paraffin-embedded sections collected from multiple brain regions according to the guidelines of BrainNet Europe. As is routine for such brain donors, staging of Alzheimer's disease was evaluated according to the Braak criteria for NFTs[68], CERAD criteria adjusted for age and Thal criteria[69]. The presence and topographical distribution of aSyn (monoclonal mouse antihuman-a-synuclein, clone KM51, Monosan) was rated according to Braak's staging scheme for aSyn[70] and a modified version of McKeith's staging system for aSyn (i.e., brainstem, limbic system, amygdalapredominant or neocortical[71].

2.2.2 Safety Considerations for Tissue Handling

All tools/surfaces coming in contact with the chemically fixed, postmortem human brain tissues were sterilized with a mixture of 2% sodium dodecyl sulfate (SDS) and 1% acetic acid, for sterilization against potential pathogenic agents[72]. For delicate parts such as the fine diamond tips of the Diatome™ knives, 50% ethanol – as recommended – was used.

2.2.3 Tissue Preparation for Cryo-PXCT Imaging

Tissues were prepared as previously described for mouse brain[61] with some alterations regarding the final trimmed sample shape. The fixed tissue was sectioned using a Vibratome into 60 mm thick slices, kept at 4C in glass scintillator vials with tight rubber seals in 0.15M cacodylate buffer. PBS (without calcium or magnesium) can be substituted. Circular regions were biopsy-punched out from the tissue in the neuromelanin-rich areas using a Harris Uni-Core biopsy punch tool (diameter 1.20 mm) on a Harris Cutting Mat. Punched-out pieces were placed in cryoprotectant (1.2M sucrose with 15% polyvinylpyrrolidone) in small plastic vials,

rotating at 4C for 2–3 weeks. Prior to cryo-ultramicrotomy, tissue pieces were checked to ensure that all sunk to the bottom of the tubes, indicating full penetration of cryoprotectant to the tissue. Tissue pieces were kept in the tubes on ice while preparing the OMNY pins[73] in a method as previously described[61]. On the day of cryo-trimming, cryo-knives (Diatome™ 45° diamond trim knife and 90° diamond trim knife) were loaded and the cryo-chamber was cooled to -90C. OMNY pins were slightly shaved down to an appropriate height as previously described. For dissection, pieces of biopsy-punched tissue were placed in droplets of cryo-protectant on a black plastic block on ice; a black piece of paper glued to the other side of a petri dish, on ice, could also be used. This black plastic block (Leica) is typically used for mounting of pins for cryo-ultramicrotomy Tokuyasu technique. A Microfeather 30 ophthalmological scalpel was used to cut the pieces (in cryoprotectant) into four quadrants, further cut into 8 “pie pieces” in total. The sample was held in place using fine electronic-grade tweezers during this cutting. The leg of one of the tweezers was used to position one “pie-piece” of tissue onto the tip of a shaved OMNY pin [61] positioned in a small aluminum cube adaptor. Ethanol (70%) was used to continuously clean the tweezers to prevent hardening/sticking due to the cryoprotectant. A clean 200 ml pipette tip was used to gently position the piece of tissue straight and centered onto the OMNY pin. The pipette tip did not stick as much to the tissue as the metal tweezers. The OMNY pin and adaptor was then placed into the cryo-chamber at -90C and kept therein for 1 h. This is a “slow-freezing” technique typical for cryo-immunogold electron microscopy[74,75]. This procedure was repeated for mounting all “pie pieces” of tissue from two biopsy-punched pieces of tissue, onto multiple OMNY pins. The small aluminum cube adaptors, holding the OMNY pin on which each tissue piece was previously “glued” using the extra cryoprotectant (liquid at room temperature, then hardened while transferred and left in the cryo-ultramicrotome chamber at -90C), were then firmly clamped into the standard clamping chuck of the Leica cryo-ultramicrotome for subsequent trimming into a skyscraper-type shape of approximately 100 µm in X-Y-Z dimensions using a Trim 90^0 (Diatome™) diamond knife with a 90° cutting angle. Samples were stored in liquid nitrogen until imaging by cryo-PXCT. Safety considerations were performed according to section “Safety Considerations for Tissue Handling.”

2.2.4 Cryo-PXCT Data Collection and Tomogram Reconstruction

Cryo-PXCT measurements were carried out at the cSAXS beamline at the Swiss Light Source, Paul Scherrer Institut (PSI), Switzerland. The cryo-PXCT data was collected by Esther H. R. Tsai, Ana Diaz, Manuel Guizar-Sicairos, Mirko Holler (PSI). Nine tomograms (four of Parkinson's diseased human brain and five of non-demented control human brain) were obtained under cryogenic conditions (-180C) using OMNY[62]. A general description of the experimental setup is provided as follows. Samples were mounted on customized sample pins[73] and imaged at a photon energy of 6.2 keV, defined by a double crystal Si (111) monochromator. The illumination on the sample was defined by the combination of a 50 µm-diameter central stop, a coherently illuminated 220 µm-diameter Fresnel zone plate (FZP) with an outer-most zone width of 60 nm, and a 30 µm diameter order sorting aperture. The FZP was fabricated by the Laboratory for Micro and Nanotechnology, Paul Scherrer Institut. The focal distance was 66 mm while the sample was placed 2.4 mm downstream the focus to give an illumination of around 8 µm in diameter on the sample. For each ptychographic projection, the scanning followed a Fermat spiral pattern[76] with an average step size of 2.6 micron. For each scanning position, a diffraction pattern was collected 7.3 m downstream of the sample with an EIGER[77] detector and exposure time of 0.1 s. Projections were taken from 0 to 180 degrees. The field of view and the number of projections for each tomogram are detailed in Table 1. Esther H. R. Tsai (PSI) primarily completed all of the tomographic reconstructions. It were obtained through the difference map algorithm[78] followed by maximum likelihood algorithm[79] using software PtychoShelves[80]. For each diffraction pattern an area of 500 by 500 pixels was used for the reconstruction, giving an image pixel size of approximately 40 nm. 2D projections were aligned [57,58] to generate 3D tomograms based on modified filtered back projection[57]. The grayscale in the tomograms correspond to absolute electron density[81]. Image resolution was estimated by FSC[82]. The number of photons incident on the sample for one projection fell in the range of 2.5 x 106 to 4.5 x 106 photons/μm^2. X-ray doses exposed to the frozen brain samples were estimated using absorption coefficients of water with attenuation length of 451 µm and density 1,000 kg/m^3. Estimated resolutions and X-ray doses can be found for each measurement in Table 2.1. Safety considerations were performed according to section "Safety Considerations for Tissue Handling."

2.2.5 Immuno-Electron Microscopy After Cryo-PXCT Imaging

Tissue blocks corresponding to Tomo 5 (Control human brain) and Tomo 2 (Parkinson's diseased human brain) were selected for downstream cryo-ultramicrotomy and immunogold labeling followed by imaging by electron microscopy (**Figure 2.12**). Tissue blocks were mounted into the cryo-ultramicrotome chamber and sectioned at -100C, typical for cryo-immunogold labeling for electron microscopy[74,75]. Sections of 70 nm thickness were created using a sectioning speed of 0.2 mm/s with a Diatome™ "Cryo35" knife, without use of the static ionizer. Sections were picked up from surface of the knife using a Diatome™ "Perfect Loop" with a droplet of solution prepared by adding 2.3 M sucrose in phosphate buffer to 2% methylcellulose in distilled water with a ratio 3:1, and transferred to the surface of a hexagonal 200-mesh gold EM grid using a technique as previously described[75]. Calcium-magnesium-free PBS were used to wash sections from both control human brain and Parkinson's diseased human brain tissue blocks to remove pick-up solution (three times for 2 min each). After washing, those sections were inactivated free aldehyde group by incubating with 50 mM glycine in calcium-/magnesium-free PBS for 15 min and were then blocked hydrophobic areas using AURION™ Blocking Solution for Goat antibody Gold Conjugated (product code 905.002) for 30 min. After washing by calcium-/magnesium-free PBS buffer containing 0.1% AURION™ BSA-c (product code 900.099), they were immunolabeled using the following primary antibodies: 1 mg/ml of anti-VDAC1 (mitochondrial porin antibody, Abcam ab14734), 2 mg/ml of anti-LAMP1 antibody (lysosomal marker, Abcam ab24170), 5 mg/ml of anti-alpha-synuclein (LB509, Abcam ab27766), or 10 mg/ml of anti- phosphorylated alphasynuclein (S129, Abcam ab59264). Sections on each EM grid were subject to only 1 kind of antibody each (no multiple labeling). Antibodies were diluted in a calcium-/magnesium-free PBS buffer containing 0.1% AURION™ BSA-c. Sections on the EM grids were incubated for 1 h at room temperature with the primary antibodies. After primary antibody incubation, they were washed 6 times, 5 min each with calcium-/magnesium-free PBS solution containing 0.1% AURION™ BSA-c. Secondary immunogolds (10 nm diameter, AURIONTM ImmunoGold reagents) were incubated for 90 min at room temperature, then washed with calcium-/magnesium-free PBS containing 0.1% AURION™ BSA-c, followed by additional wash by calcium-/magnesium-free PBS. Afterward, sections on grids were postfixed by 2% glutaraldehyde in calcium-/magnesium-free PBS for 5 min. To remove glutaraldehyde, grids were washed extensively with calcium-/magnesium-free PBS, then

deionized/distilled water. Subsequently, grids were additionally contrast-enhanced using 4% neutral uranyl acetate, which was prepared by mixing 4% uranyl acetate and 0.3M oxalic acid and was adjusted to pH 7 by 25% ammonium hydroxide. A solution of 0.4% uranyl acetate in 2% methylcellulose was then used for further contrast-enhancement (on ice). EM grids were then imaged at room temperature using an FEI T12 (Thermo Fisher Scientific, United States) operated at 120 kV. Electron micrographs were recorded by Dr. Sarah Shahmoradian (PSI) and Amanda J. Lewis (C-CINA University of Basel) on a 4096 x 4096 pixel F416 CMOS camera (TVIPS GmbH, Germany). Safety considerations were performed according to section “Safety Considerations for Tissue Handling.”

2.2.6 3D Color Segmentation and Statistical Analysis of Dystrophic Myelinated Axons (DMAs)

Three-dimensional visualization and color segmentation was performed using commercial software Avizo 9.2.0 (Thermo Scientific). The images were imported into Avizo software and the threshold of the colormap was adjusted appropriately. The features of interest including blood vessels, nuclei, red blood cells and myelinated axons were segmented semi-automatically with the use of the “Brush” and “Interpolate” tools. The neuromelanincontaining organelles that appear as dark, dense globules could be segmented by “Threshold” tool. The masking value was adjusted until all neuromelanin-containing organelles were masked and identified precisely, then were selected and assigned by “Select Masked Material” tool for all slices. Unexpected selected regions not corresponding to neuromelanin were deselected semiautomatically afterward by using “Brush” and “Interpolate” tools. After all structures were segmented and registered to their appropriate materials (blood vessel, myelinated axon, etc.), they were smoothed independently by locking other materials. Afterward, smoothed materials were exported into individual data objects from the Labels dataset by the “Arithmetic” function and surfaces were then generated for visualization. Myelinated axons, neuromelanin, nuclei, red blood cells were visualized by the “Shaded” draw style while blood vessels and the swollen part of the myelinated axons were visualized by “Transparent” draw style to reveal their inside contents. This label separation process allowed us to visualize the surface of single

material without disturbing others. Afterward, snapshots of 3D color-rendered surfaces and movies were created for presentation.

2.3 Results

2.3.1 Cryo-PXCT Imaging

Cryo-PXCT using the OMNY instrument[62] at the cSAXS beamline of the Swiss Light Source was utilized to visualize five and four brain tissue samples, respectively (*Table 2.1*) from a control, non-demented donor and a Parkinson's diseased donor (*Table 2.2*, Donors B and D). Cryo-PXCT was used to identify pathological-related abnormalities in postmortem brain tissue from Parkinson's diseased (PD) human patients, within roughly cubic volumes spanning ~(100 μm)^3 at a resolution ranging from 145 to 390 nm. The substantia nigra pars compacta (SNpc) brain region was selected for dissection and imaging since this region typically contains the most pathology and highest clinical relevance[83]. Samples were prepared according to a pre-established protocol optimal for cryo-PXCT imaging of mouse brain tissue[61], with an improved trimming procedure (**Figure 2.3**), which resulted in a skyscraper-type structure rather than a pyramidal-type structure to enable more efficient imaging resulting in larger overall studied volumes.

Four cryo-PXCT tomographic datasets were generated from four separate blocks of human postmortem brain tissue from a PD brain donor (*Table 2.1*). As a control, five cryo-PXCT tomographic datasets were generated from five separate blocks of human postmortem brain tissue from a non-demented, age-matched control human brain donor (*Table 2.1*), three of which are shown as virtual slices in **Figure 2.3**.

	Control Human Brain					Parkinson's Diseased Human Brain			
	Tomo 1	Tomo 2	Tomo 3	Tomo 4	**Tomo 5**	Tomo 1	Tomo 2	Tomo 3	**Tomo 4**
Data collection (hours)	33	28	19	35	**34**	37	31	62	**42**
Volume imaged (μm^3)	230,000	123,000	55,000	260,000	**204,000**	400,000	258,000	426,000	**220,000**
Dimensions (X,Y) (µm)	150	120	110	110	**140**	160	112	150	**120**
Depth (Z) (µm)	30	25	20	50	**30**	35	50	50	**40**
Projections	750	850	850	700	**600**	800	640	1100	**700**
Estimated dose (MGy)	9	9	9	7	**4**	15	11	19	**12**
3D resolution estimation (nm)	255	215	145	240	**245**	280 (2D) 380	270 (2D) 390	250	**190**

Table 2.1: Imaging parameters and characteristics of biological samples imaged by cryo-PXCT using OMNY.

Table summarizes the volume imaged per tomogram, data collection time, dimensions in X-Y-Z of the imaged region of the tissue block, projections used for tomographic reconstruction, estimated dose (MGy), and estimated 3D resolution, for each of the samples. **Tomo 5** (control human brain) and **Tomo 4** (PD human brain), were selected for 3D color segmentation.

Donor	Diagnosis	Age at onset (years)	Age at death (years)	Sex	PMD (hrs:min)	Braak aSyn stage
A	PDD	59	77	M	5:15	6
B	PDD	75	90	F	4:45	6
C	NDC	-	85	F	6:25	0
D	NDC	-	92	M	7:45	0
E	NDC	-	89	F	13:00	0

Table 2.2: Clinical and pathological characteristics of brain donors.

PDD, PD with dementia; age-at-onset, age at clinical diagnosis of PD; NDC: non-demented control; aSyn: a-synuclein; PMD: postmortem delay. Age at onset, age at clinical diagnosis of PD. Donors B and D were used for cryo-PXCT and cryo immuno-electron microscopy. All donors were used for optical microscopy studies.

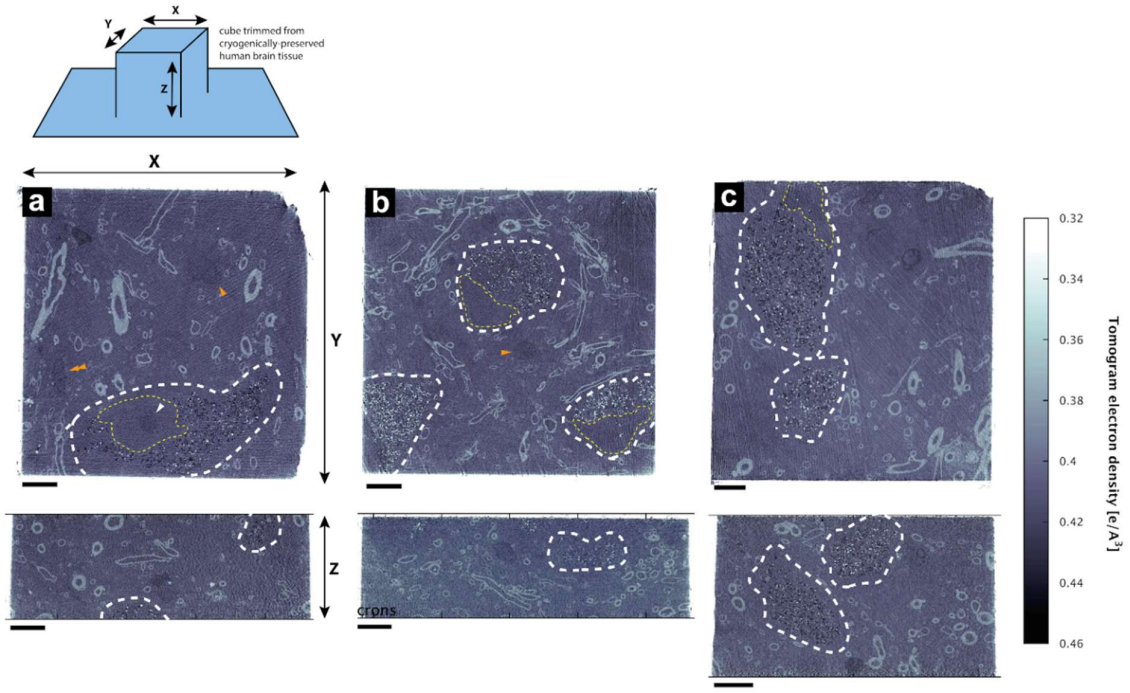

Figure 2.3: Human brain imaged by cryo-PXCT using OMNY.

Representative orthoslices are shown from an X-Y plane (top panels) and X-Z plane (bottom panels) from three of the nine total human brain tomograms collected. Grayscale intensity values directly correspond to mass density. Data shown corresponds to orthoslices from (a) Tomo 5, (b) Tomo 1, (c) Tomo 4 (*Table 2.1*). Scale bars: 10 µm.

The grayscale in the tomograms is proportional to the absolute electron density of the specimens. The thorough infiltration of cryoprotectant (sucrose), which have higher density compared to the density of proteins and lipids provided good contrast to distinguish various sub-cellular features in brain tissues. Particularly, neuromelanin-containing cells typical of the substantia nigra region were clearly visible in the tomograms (**Figure 2.3**, white dotted lines), as well as the cross-sections of myelinated axons (high contrast ellipsoid and circular structures). Nuclei (**Figure 2.3**, yellow dotted lines) of these neuromelanin-containing cells, and a smaller dense nucleolus (**Figure 2.3**a, white arrowhead), were also visible. Nuclei likely corresponding to glial cells were observed as an elongated, irregular nucleus with characteristic peripheral heterochromatin and heterochromatin net made of multiple fused granules[84] (**Figure 2.3**, orange double-arrowhead), and dense, round nuclei typical of oligodendrocytes[84] were also visible (**Figure 2.3**, orange single-arrowheads).

2.3.2 3-D Segmentation and Quantification

Segmentation is the process of dividing raw stacked images into different segmented features, which can be represented in 3-D view. In this research, we used the commercial software Avizo, which is a common software platform for 3D data visualization, processing, and analysis. Tomogram #5 from control group and tomogram #4 from PD group were selected for subsequent 3D color segmentation (*Table 2.1*). The grayscale in the tomograms was inverted for easy correlation with downstream electron microscopy.

The most commonly used tools to correct the segmentation within each image slice were "Brush" and "Interpolate" function of Avizo software. Since myelin has a very low density compared to the surrounding tissue, which led to highly contrasted images, it was easy to select by "Brush" tool with the assist of a pen and touchpad (**Figure 2.4**a,b). In addition, most of the myelinated axons extended continuously through a long distance without sudden turns or juts so "Interpolate" tool was used to reduce processing time. It was possible to skip a few slices and select the same myelinated axon in the following slices until it changed shape, direction or it developed side branches, then "Interpolate" function could fill in the slides between the ones that were manually selected. Besides, myelinated axons extended in multiple 3-D directions so it was easier and more precise to trace and segment them in different planes (X-Y, X-Z, Y-Z). Similar procedure was applied to segment blood vessels, nuclei and red blood cells inside blood vessels (**Figure 2.4**d,e,g,h,j,k). The nuclear boundaries of non-neuromelanin-containing cells and neuromelanin-containing cells were distinguishable because density in the nuclei was less than in the surrounding cytoplasm (**Figure 2.4**d,g). However, the nuclear membranes themselves were not distinguishable because their thickness was 20-40 nm, below cryo-PXCT resolution[61]. The blood vessels had lower contrast so the threshold of tomograms was adjusted continuously to recognize the difference of density between two areas (inside blood vessels and surrounding tissue). Correction of segmentation of the same blood vessels in all planes (X-Y, X-Z, Y-Z) together was also beneficial to segment them precisely. The neuromelanin-containing organelles were segmented differently since they are small (~500nm) and abundant so manual segmentation by "Brush" and "Interpolate" tool was very time-consuming. Therefore, the lipid vesicle components of neuromelanin-containing organelles, which had low density and appeared as highly contrasted dark bodies (**Figure 2.4**m, inverted greyscale), were semi-automatically segmented

by “Thresholding” tool (**Figure 2.4**n) (for details see Methods). As a result, the identity of several cellular features in two datasets became more apparent by 3-D representation (**Figure 2.5, 2.6**).

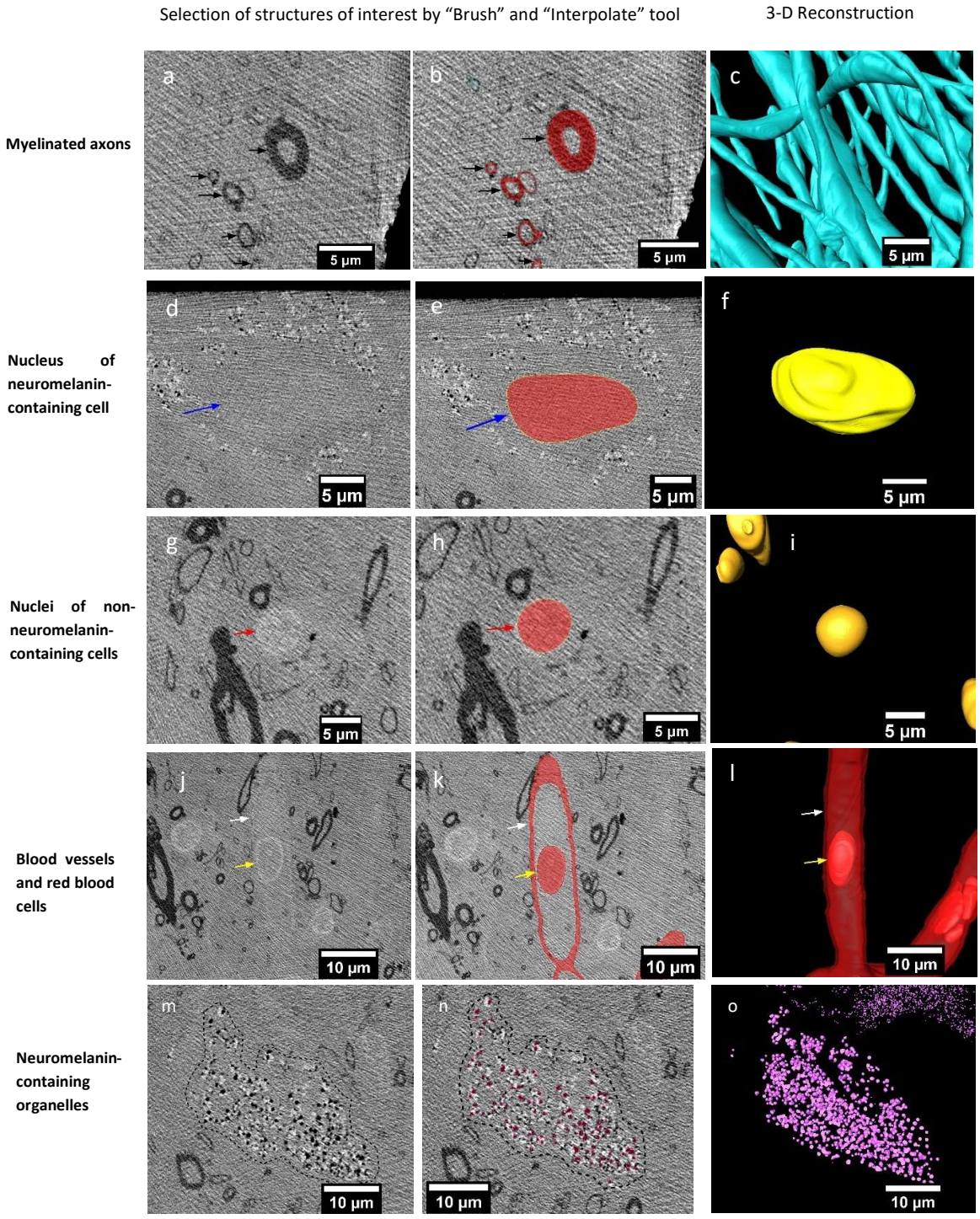

Figure 2.4: Segmentation of cellular features in human brain tissue tomograms.

(a,d,g,j,m): The threshold of tomograms was adjusted to reveal cellular structures; (b,e,h,k,n): The structures of interest were selected by “Brush” and “Interpolate” tool; (c,f,i,l,o): Reconstruction of cel-

lular structures in 3-D. Black arrows: myelinated axons; Blue arrow: nucleus of neuromelanin-containing cells; Red arrow: nucleus of non-neuromelanin-containing cells; White arrow: blood vessel; Yellow arrow: red blood cell; Black dotted-line: neuromelanin-containing organelles; Aqua = myelinated axons; Yellow (white arrowhead) = nucleus of neuromelanin-containing cell; Orange = nuclei of non-neuromelanin containing cells; Pink = neuromelanin-containing organelles; Red = blood vessels; Dark red = blood cells within the blood vessels.

While features such as neuromelanin-containing cells, blood vessels, glial nuclei, and myelinated axons could all similarly be segmented from both control and PD cryo-PXCT human brain tomograms (**Figures 2.5, 2.6**), one feature that was uniquely observed in all four PD brain datasets as compared to all five control brain datasets was the presence of swellings within the myelinated axons (**Figures 2.6**b,d, purple segments within the aqua axons; **Figure 2.7** and **Supplementary Figures 2.1, 2.2**, yellow crosses) as compared to the rest of the axons (**Figures 2.6**b,d, aqua axons). These swellings were in close proximity to the neuromelanin-containing cells (**Figure 2.6**e), which are majorly affected in PD. Different views of approximately ten of these swellings, or dystrophic myelinated axons (DMAs) are shown at greater detail within one of the PD brain tomograms (**Figure 2.7** and **Supplementary Figures 2.1, 2.2**; yellow crosses). The variability of the type of swelling is more apparent when the DMAs are visualized in 3D color segmentations, eight of which are shown in **Figure 2.8**. For example, the inner part of the axon, or axoplasm, can appear relatively "normal" and consistent in diameter along the length of the axon (**Figures 2.8**) with the swelling occurring in the axoplasm itself (**Figure 2.8**a-d) or in the layers comprising the myelin sheath of the axon (**Figure 2.8**e-g), or in both the oligodendrocyte cytoplasm and underlying axoplasm (**Figure 2.8**h).

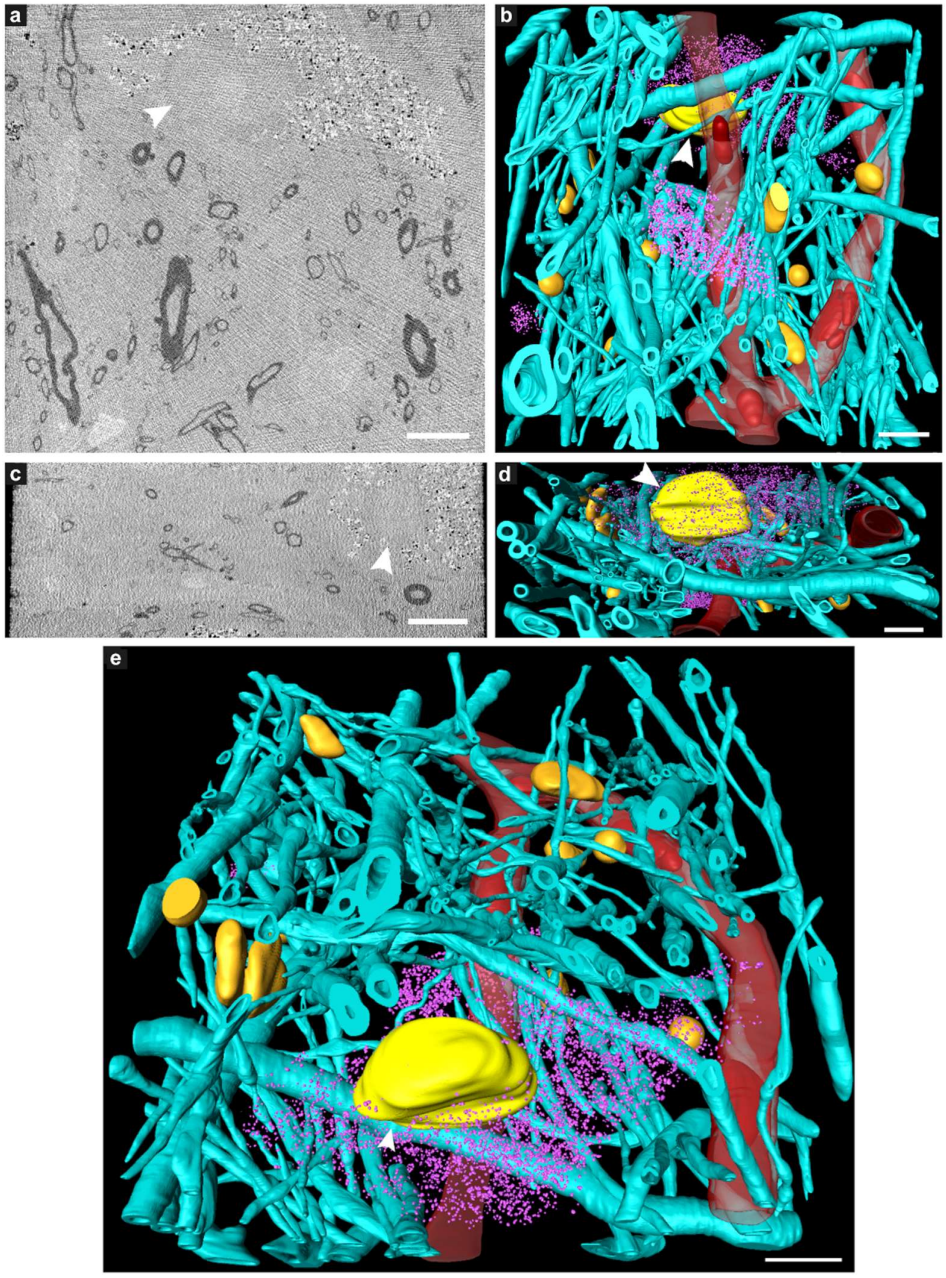

Figure 2.5: Tissue components in 3D color-segmented cryo-PXCT datasets of non-demented control human brain.

Single 2D orthoslices with inverted grayscale in the (a) X-Y plane and (c) X-Z plane, shown from the 3D volume used for the corresponding color segmentation, displayed in the (b) X-Y plane, (d) X-Z plane, and (e) tilted larger-scale view. Aqua = myelinated axons; Yellow (white arrowhead) = nucleus of neuromelanin-containing cell; Orange = nuclei of non-neuromelanin containing cells; Pink = neuromelanin-containing organelles; Red = blood vessels; Dark red = blood cells within the blood vessels. Corresponds to "Control human brain," Tomo 5 (Table 2.1). Scale bars: 10 µm.

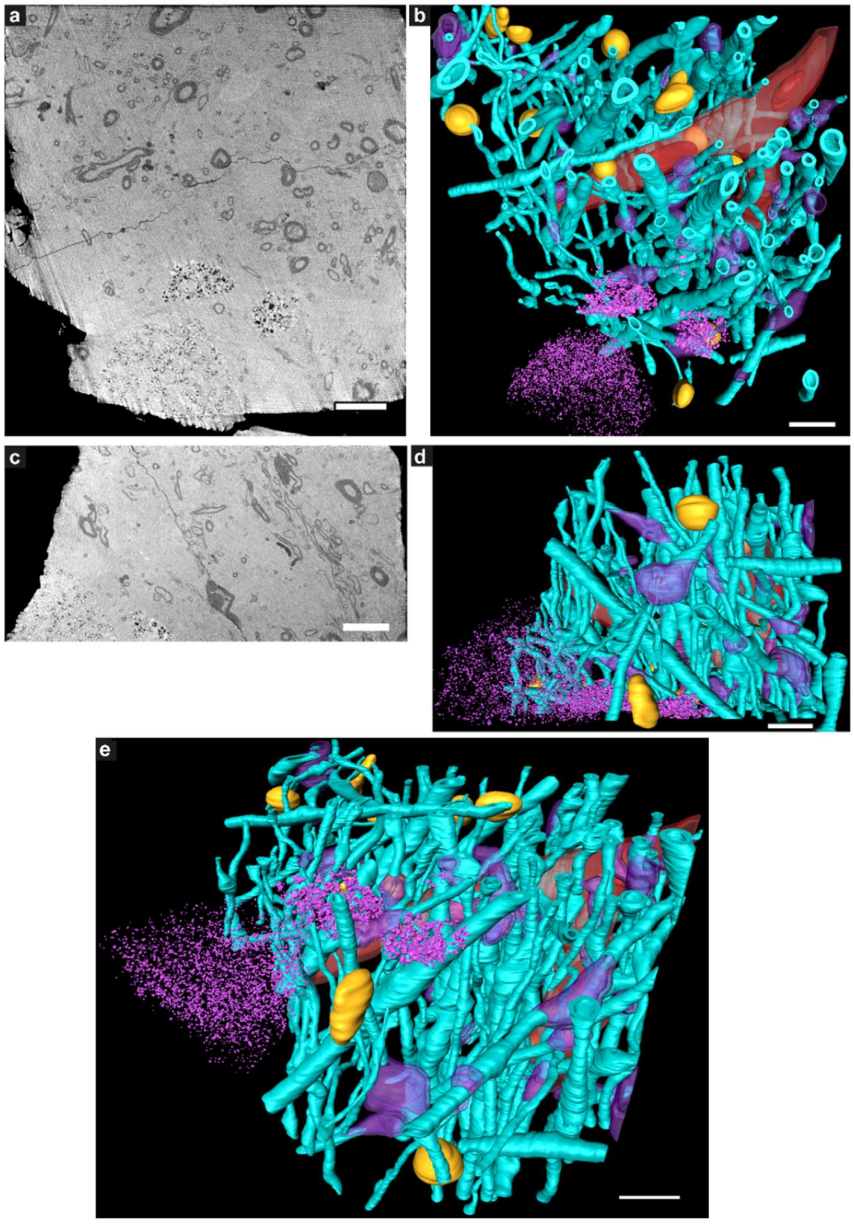

Figure 2.6: Tissue components in 3D color-segmented cryo-PXCT tomograms of PD human brain.

Single 2D orthoslices with inverted grayscale in the (a) X-Y plane and (c) X-Z plane, shown from the 3D volume used for the corresponding color segmentation, displayed in the (b) X-Y plane, (d) X-Z plane, and (e) tilted larger-scale view. Aqua = myelinated axons; Purple = swellings along the axons (DMAs); Orange = nuclei of non-neuromelanin-containing cells; Pink = neuromelanin-containing organelles; Red = blood vessels; Dark red = blood cells within the blood vessels. Corresponds to "PD human brain," Tomo 4 (Table 2.1). Grayscale shown herein does not correspond directly to mass density as opposed to **Figure 2.3**. Scale bars: 10 µm.

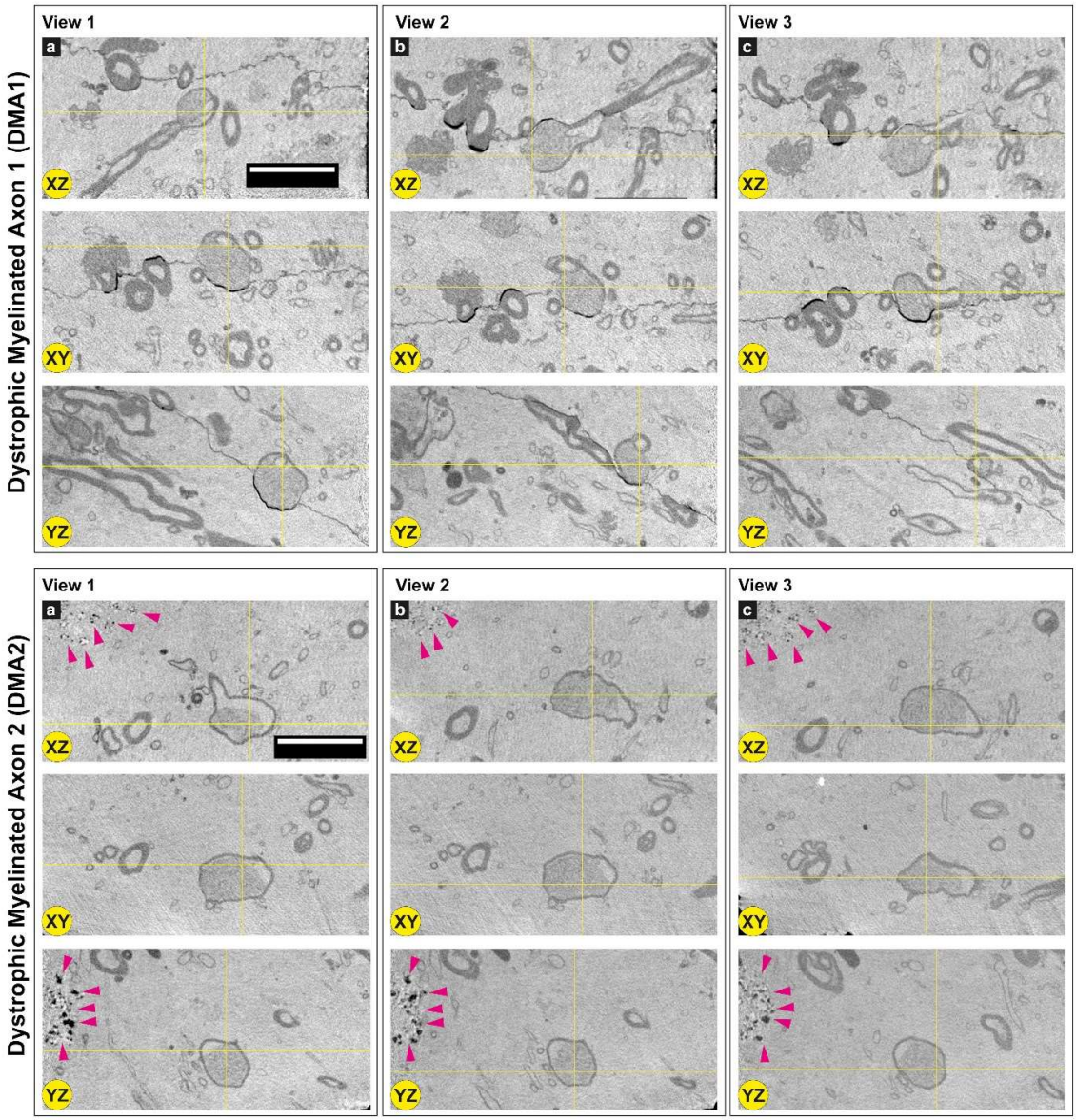

Figure 2.7: Dystrophic myelinated axons (DMAs) by cryo-PXCT in PD human brain.

Single 2D orthoslices with inverted grayscale showing the appearance of two DMAs in different planes (X-Z, X-Y, Y-Z) and different positions (Views 1, 2, 3) in the 3D tomogram. Yellow crosses indicate the position of the DMA in the different views and planes. Several other DMAs are shown in Supplementary Figures 2.1, 2.2. Grayscale of all 2D cutaways shown herein correspond to electron density. Pink arrowheads = neuromelanin-containing organelles of adjacent cell. a, b, c refer to the different columns corresponding to View 1, View 2, and View 3, for clarity sake. Scale bars: 10 µm

---

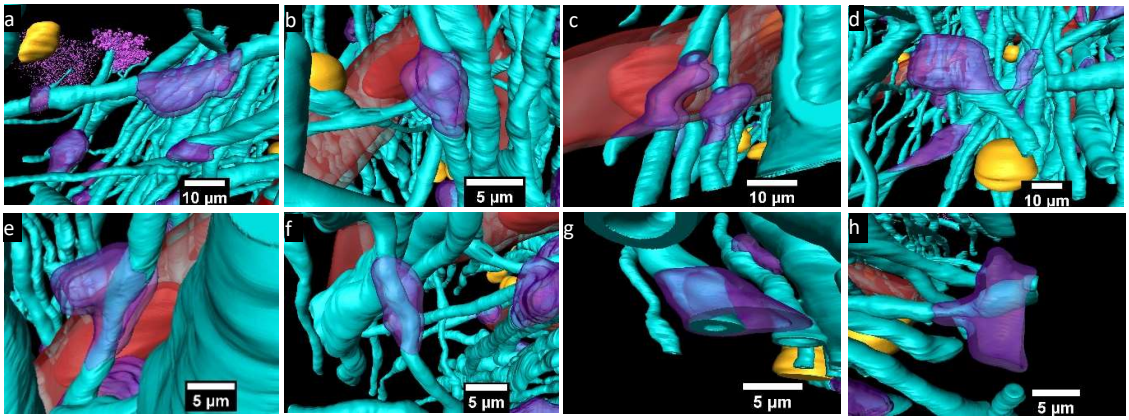

Figure 2.8: 3D color representations of DMAs in Parkinson's diseased human brain by cryo-PXCT.

(a-d) DMAs in which the swellings (purple) occur in axoplasm, (e–h) DMAs with oligodendrocyte swollen in the myelin sheaths at a region along the length of the myelinated axon (aqua), (h) DMA with visible swelling in both the oligodendrocyte cytoplasm (purple) and underlying axoplasm (aqua swelling beneath the purple). Red = blood vessel; Dark red = blood cell; Orange = nuclei of non-neuromelanin containing cells; Pink = neuromelanin-containing organelles.

Two types of DMAs were identified and characterized by cryo-PXCT: one population we refer to as SWiA (swollen in axoplasm) and another as SWiM (swollen in myelin). "In axoplasm" refers to cytoskeletal part of the axon that is in direct continuation from the neuron (**Figure 2.9**b), whereas "in myelin cytoplasm" refers to the cytoplasm within the myelin sheaths (**Figure 2.9**c) corresponding to that of the parent oligodendrocyte rather than the neuron[85]. Since the resolution of these reconstructed tomograms enables distinguishing the axoplasm from the myelin sheath, especially when the myelin sheath appears to have partially separated, we could detect dense granular cytoplasmic material comprising these DMAs that appeared surprisingly often within the wrappings of the myelin sheath (**Figure 2.7** "DMA1", **Figures 2.8**e–g, and Supplementary Figure 2.1 all excluding "DMA3") of the parent oligodendrocyte, hence the SWiM type, rather than simply within the axonal passage itself (the SWiA type). This was counter-intuitive considering that the clogging of the axon was not mainly occurring in the axonal passage itself, but rather in the exterior myelin sheaths compromising the axon. Typically, axonal traffic jams associated with neurodegenerative disease are generally attributed to material accumulating within the axonal passage itself[10,86,87] thereby resulting in a local swelling of the SWiA type, which we did observe albeit

to a lesser extent (**Figure 2.7** "DMA2" and Supplementary Figures 2.1 "DMA3"). Overall, 74% (40) of DMAs were found to be the SWiM type (**Figure 2.9**c), corresponding to a swelling within the cytoplasm of the actual myelin sheath, while 26% (14) of DMAs were found to correspond to the SWiA type (**Figure 2.9**b), corresponding to the more intuitive case of a swelling within the neuronal cytoplasm inside the axon itself (**Figure 2.10**). Quantification performed for each of the four PD brain tomograms independently (**Figures 2.10** b-e) also showed a similar theme with the majority of DMAs corresponding to the SWiM rather than the SWiA type. To assess the degree of swelling in each DMA, three groups of measurements were taken in all planes (X-Y, Y-Z, X-Z) together for each DMA before, within, and after the swelling: (1) the axon diameter, averaged across three positions on the axon preceding the swelling, (2) of the maximum diameter of the axonal swelling, and (3) the axon diameter, averaged across three positions on the axon following the swelling. A great variability was observed for each swelling, ranging from ~3 to 11 μm (**Figure 2.11**).

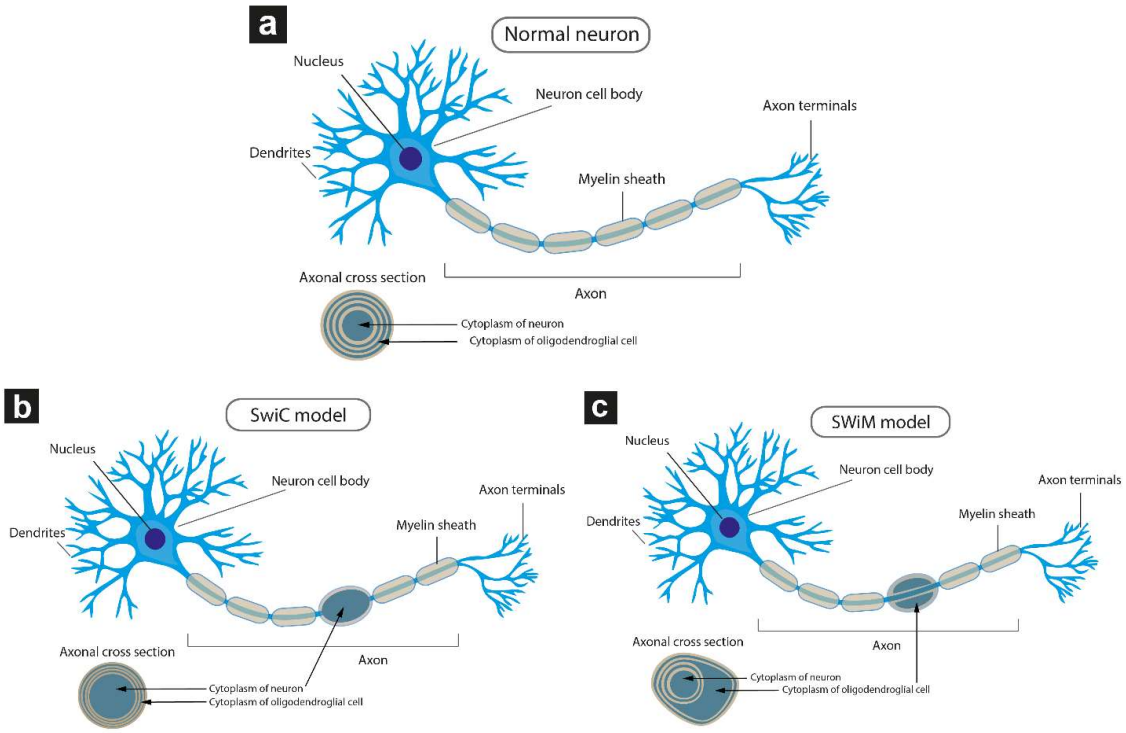

Figure 2.9: Schematic model of different types of dystrophic myelinated axons (DMAs) as observed by cryo-PXCT in Parkinson's diseased human brain.

Overall appearance of the myelinated axon protruding from a neuron, and zoomed-in cross-section of the myelinated axon (inset), is shown for each type: (a) neuron with a normal appearance of myelinated axon, in which the cytoplasm of the oligodendroglial cell is barely visible due to the typical tight compaction of the myelin sheaths (beige); (b) neuron with swelling in the axon, in which the neuronal cytoplasm within the axon is enlarged, referred to as "swelling in axoplasm" or SWiA; (c) neuron in which cytoplasm within myelin sheath is expanded, referred to as "swelling in myelin sheath" or SWiM. Oligodendroglial cells are not shown. Their extensions flatten out and wrap around the axon multiple times, forming the myelinations that appear as "sausage"-like pieces (beige) from the overview. The layers of myelin are apparent from the cross-sectional inset views.

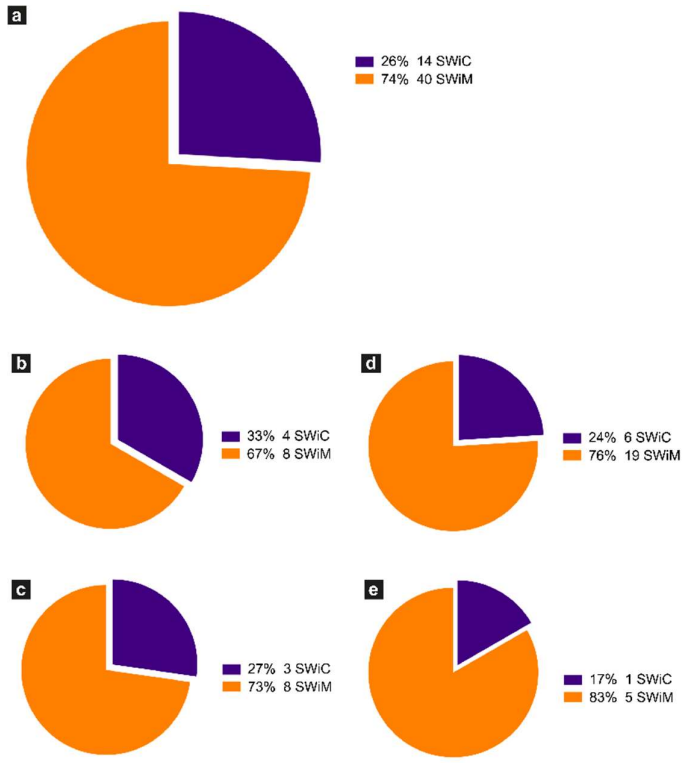

Figure 2.10: Type and abundance of DMA observed in cryo-PXCT tomograms of Parkinson's diseased human brain.

DMAs were individually assessed and categorized as either SWiA type (swelling of neuronal cytoplasm) or SWiM type (swelling of oligodendrocyte cytoplasm within the myelin). (a) Of all four cryo-PXCT tomograms of PD human brain, 54 DMAs were identified, 40 (74%) corresponding to SWiM type, and 14 (26%) corresponding to SWiA type. Measurements for each individual tomogram correspond to (b) Tomo 3, (c) Tomo 4, (d) Tomo 1, and (e) Tomo 2, all of PD human brain. Characteristics of each matching tomogram are noted in Table 2.2.

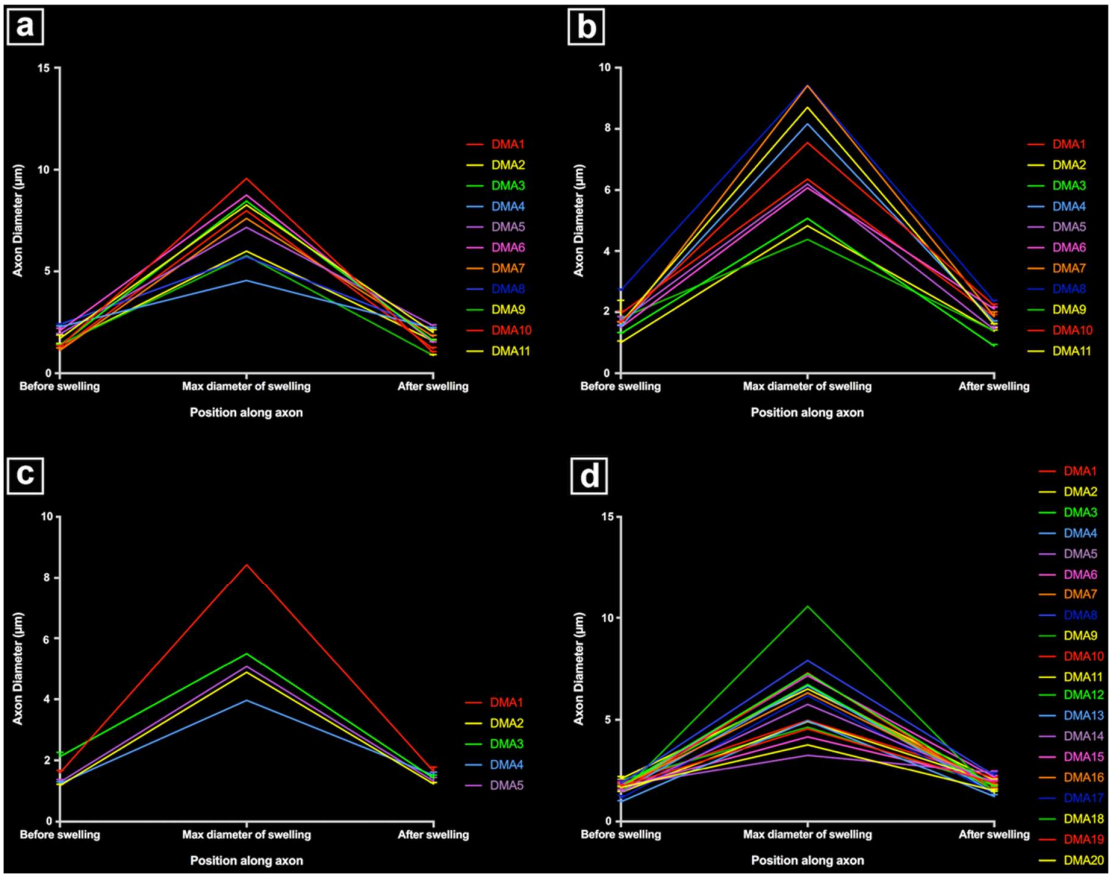

Figure 2.11: Measurements of DMAs in cryo-PXCT tomograms of Parkinson's diseased human brain.

The diameter was measured at the widest point of the swelling of the DMA (indicated by "Max diameter of swelling" in the center point of the X-axis of each graph), and averaged diameter across three positions along the axon immediately preceding the swelling (indicated by "Before swelling" on the X-axis of each graph), and averaged diameter across three positions along the axon immediately following the swelling (indicated by "After swelling" on the X-axis of each graph). Measurements shown correspond to (a) Tomo 4, (b) Tomo 3, (c) Tomo 2, and (d) Tomo 1, all of PD human brain. Characteristics of each matching tomogram are noted in Table 2.2.

2.3.3 Correlative Electron Microscopy

For imaging downstream target structures at higher resolution, one PD and one control tissue block after cryo-PXCT imaging were selected for subsequent cryo-ultramicrotomy at -100C[88]. The grids containing cryosections were transferred and thawed at room temperature as routine for cryo-immunogold electron microscopy[75]. Structures of interest were labeled by primary antibody followed by secondary immunogolds and contrast-stained by uranyl acetate[89], then imaged by transmission electron microscopy (TEM) at ambient temperature. This workflow is shown in **Figure 2.12**. After cryo-PXCT measurement, the tissue blocks were intact and maintained at cryo-condition for downstream processing. Each tissue block was schematically divided into three zones, and ultramicrotomed sections (70 nm thin) were cut and collected onto TEM grids sequentially from top of the block to bottom of the block, and immunolabeled accordingly. EM grids at low magnification showed the general shape and position of the resulting ultrathin sections from control human brain (**Figures 2.13**a, **2.14**a) and PD human brain (**Figures 2.15**a,g). The integrity of the tissue was as expected for cryo-immunogold labeling[74,75] with the gaps and holes typical of the methodology when applied to non-densely packed tissues with high water content like brain.

Neuromelanin-containing cells, of high clinical relevance in PD, were the most prominent and easily identifiable features within the tissue sections (**Figures 2.13–2.15**), after using the cryo-PXCT tomographic maps to navigate to the appropriate region in which these cells were originally found. By scrolling up and down through the corresponding cryo-PXCT reconstructed tomogram, we could determine the appropriate region (top, middle, bottom; edge, center) of the imaged cube in which the cells where located, which allowed to define the immunogold-stained tissue section(s) that would be most relevant to subsequently image. One neuromelanin-containing cell (**Figures 2.13**b,c) from a non-immunogold stained tissue section (**Figure 2.13**a) from a non-demented control human brain donor is shown to display clear neuromelanin-containing organelles in which the lipid vesicle component is clearly preserved amongst the typically dark, dense globules representing neuromelanin-containing organelles[90] (**Figures 2.13**d,e, blue arrowheads). The dark appearance of the globules by electron microscopy (**Figures 2.13**c–e) is attributable to the naturally high metal content of such structures, while the dark appearance typically observed by brightfield light microscopy is attribut-

able to the fact that these are pigmented akin to melanin in skin tissue. Furthermore, mitochondria with clear cristae were also visible within the tissue sections, one of which is shown enclosed within a clear axonal cross section (**Figure 2.13**f, white asterisk). The individual lipid layers of myelin sheath that compose the axon are also clearly visible, as well as the membranous profiles of vesicles (**Figure 2.13**f, orange arrowheads). In another neuromelanin-containing cell (**Figure 2.14**b) shown in a control human brain tissue section (**Figure 2.14**a) that was immunogold-stained for a prominent mitochondrial porin antibody (VDAC1, Abcam ab14734), the nucleus and nucleolus are clearly visible (**Figures 2.14**c,d); furthermore, the nuclear membrane is also visible at higher magnification (**Figure 2.14**d, aqua arrowheads). Below the neuromelanin-containing cell (**Figure 2.14**e), several mitochondria were visualized, some of which are shown in **Figures 2.14**f–j (white asterix). Immunogolds (**Figures 2.14**f–j, yellow arrowheads) are visible at the edges of the mitochondria, where the VDAC1 porin protein is expected to be localized, being an outer mitochondrial membrane protein. Specificity is demonstrated by the lack of labeling in the tissue surrounding the mitochondria. This suggests that some protein antigenicity is retained even after cryo-PXCT imaging. Interestingly, a pool of synaptic vesicles (**Figure 2.14**j, orange arrowheads), synaptic cleft (aqua arrowheads), and a mitochondrion (white asterix) visible in the postsynaptic zone, were also clearly visible. Several neuromelanin-containing cells (**Figures 2.15**a,b,g,h) could be localized in the appropriate EM tissue sections from the PD brain tissue samples, using the corresponding cryo-PXCT tomograms as a guide. In one tissue section (**Figure 2.15**a) immunogold-stained for LB509 (Abcam ab27766), an antibody that is routinely used to identify Lewy pathology as aSyn-immunopositive structures in PD, we observed that immunogolds localized to lamellar membranous structures (**Figures 2.15**e,f, yellow dotted lines) within the neuromelanin-containing organelles. These immunogolds were not visible in the background, suggesting a specificity to these structures. Similar to the control human brain tissue section, the quality of the tissue post cryo-PXCT imaging was sufficient to clearly resolve both the neuromelanin-containing organelles (**Figures 2.15**b–f,i–l, black, dark-contrast features) and their typical corresponding lipidic vesicle component known as lipid bodies[90] (**Figures 2.15**d,e,j, blue arrowheads). In another tissue section (**Figure 2.15**g) immunogold-stained for p-aSyn (phospho S129, Abcam ab59264), we found immunogolds (yellow arrowheads) localized to the edge of the lipid bodies. Our results are in line with similar immunogold electron microscopy-based studies that show aSyn is localized in the neuromelanin[90], similar to our result. Those researchers suggest that the process

of neuromelanin synthesis that starts in the cytosol, may involve accumulation of aggregated and b-structured proteins, including aSyn[90].

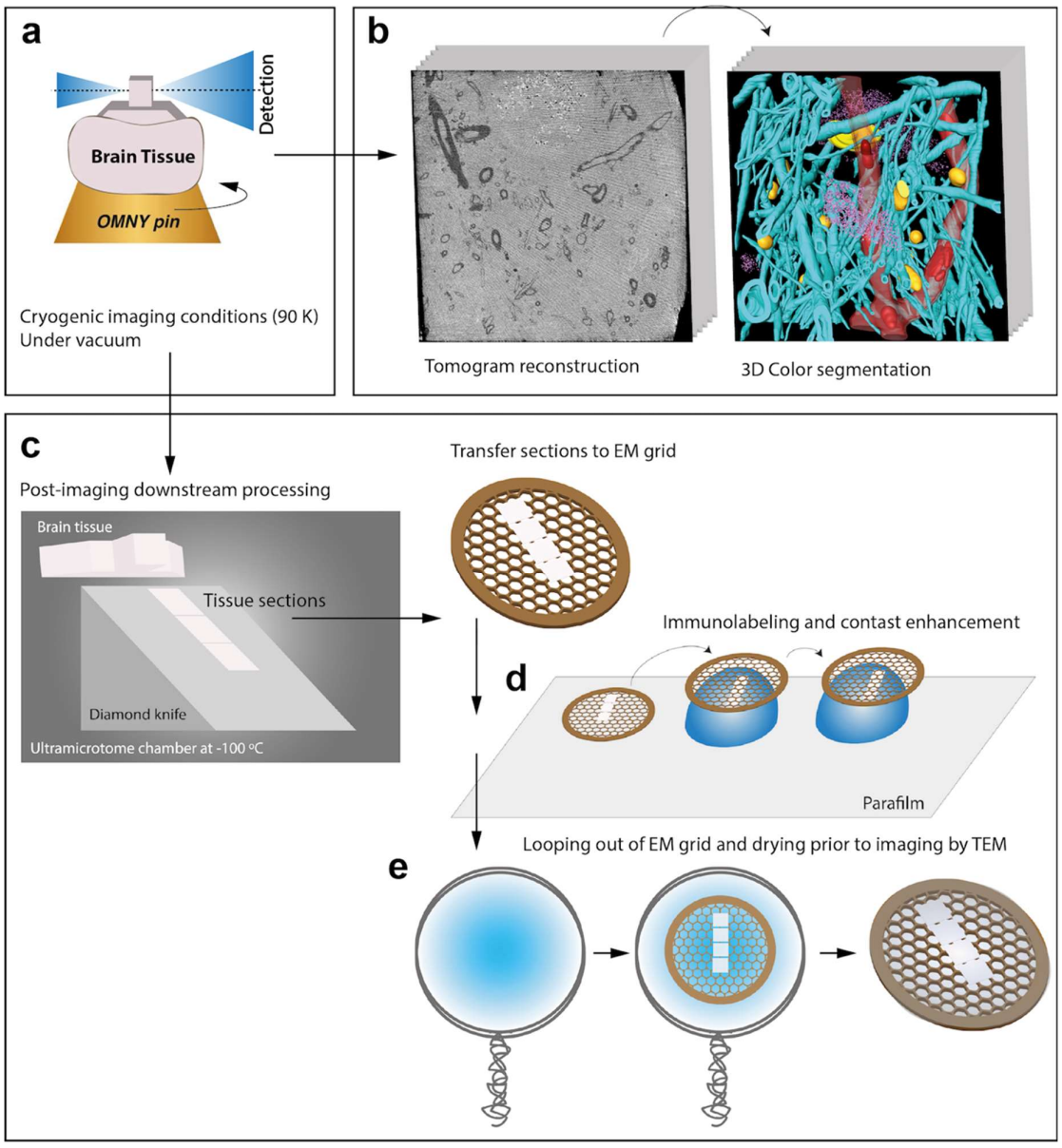

Figure 2.12: Simplified schematic workflow for tissue imaging by cryo-PXCT and downstream post-processing.

(a) Mounted and trimmed brain tissue is imaged under cryogenic imaging conditions (-180 °C) under vacuum in the OMNY[62] stage. The sample is sequentially rotated and imaged towards generating and reconstructing (b) a 3D volume, that can then be used for direct mass density measurements of features contained therein, and 3D color segmentation. Following cryo-PXCT, (c) the sample can then be re-mounted into the cryo-ultramicrotome chamber at -100 °C for trimming as is established for cryo-

immunogold electron microscopy[88], then the resulting ultrathin sections cut by the diamond knife are transferred and thawed on an electron microscopy (EM) grid at ambient temperature, where they are subsequently placed section-side downwards onto droplets with the appropriate primary antibody, blocking buffer, secondary immunogold, etc., as previously described[75,89]. (e) The sections on the EM grid are finally "looped out" with a mixture of methylcellulose and uranyl acetate (MC/UA) and left to dry, before removing the grid with the thin layer of MC/UA prior to imaging by transmission electron microscopy (TEM).

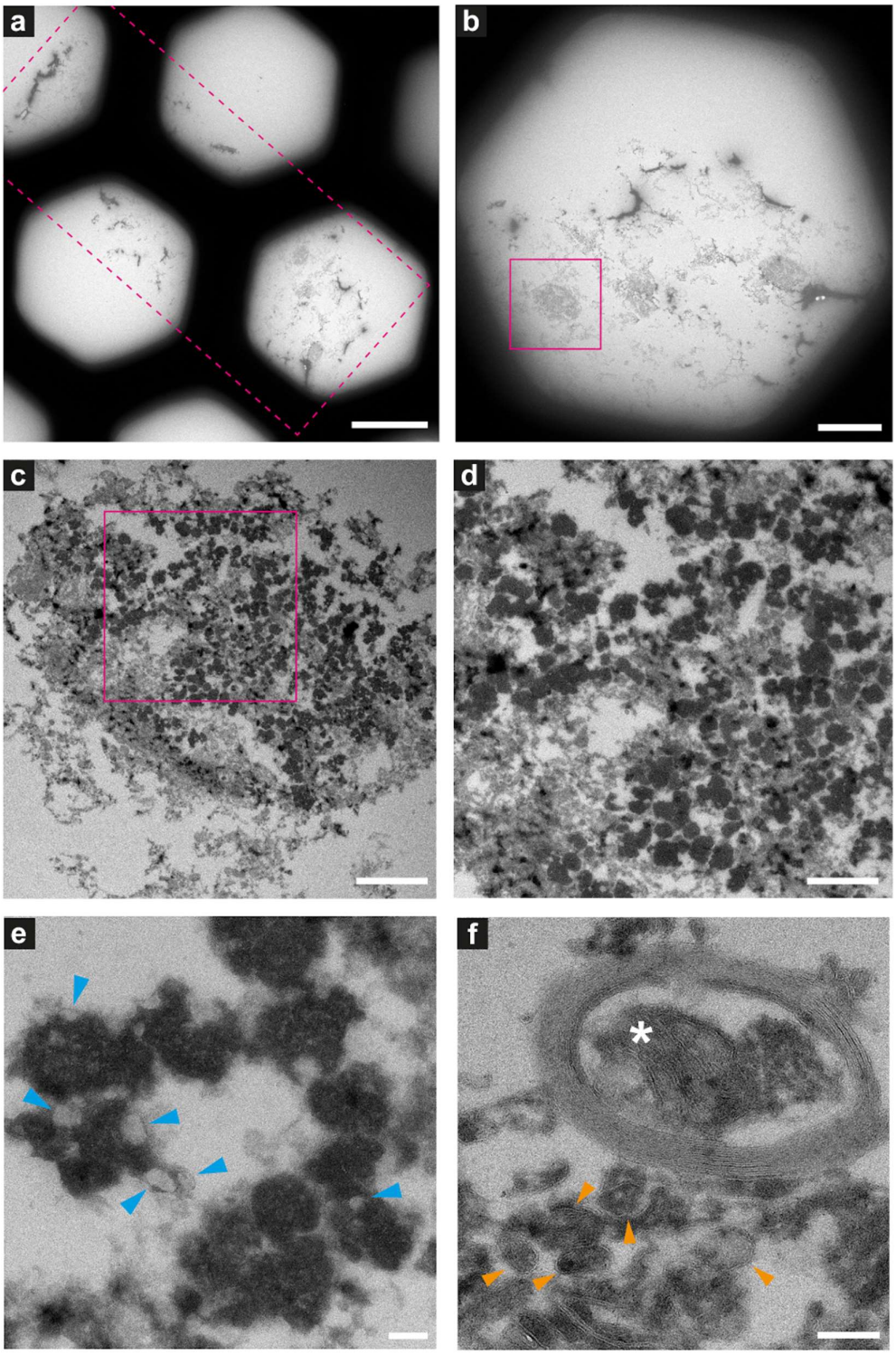

Figure 2.13: Electron microscopy of ultrathin tissue sections post cryo-PXCT imaging of non-demented control human brain.

Sections were generated by cryo-ultramicrotomy of the tissue block of non-demented control human brain (Tomo 5, Table 2.1) and contrast-enhanced using uranyl acetate, following cryo-PXCT imaging.

Images show progressively zoomed-in views of a neuromelanin containing cell and other higher-resolution cellular features. (a) Overview of the ultrathin tissue sections (pink dotted box) on the formvar-carbon support film of a hexagonal EM grid. (b) One neuromelanin-containing cell (pink box) visible in a section zoomed-in from panel (a). (c) Zoomed-in view of the same neuromelanin-containing cell as shown in panel (b), (d) Zoomed-in view of the neuromelanin as shown in the pink box in panel (c), (e) Neuromelanin granules (dark dense blobs) and typically associated lipid globules (blue arrowheads) are visible at higher magnification and resolution, (f) A mitochondrion (white asterix) is visible within the cross-section of a myelinated axon in which the individual membranes of the myelin are clearly visible, as well as individual membranes of other vesicles and features within the tissue (orange arrowheads). Scale bars: (a) = 80 µm; (b) = 30 µm; (c) = 3 µm; (d) = 2 µm; (e,f) = 200 nm.

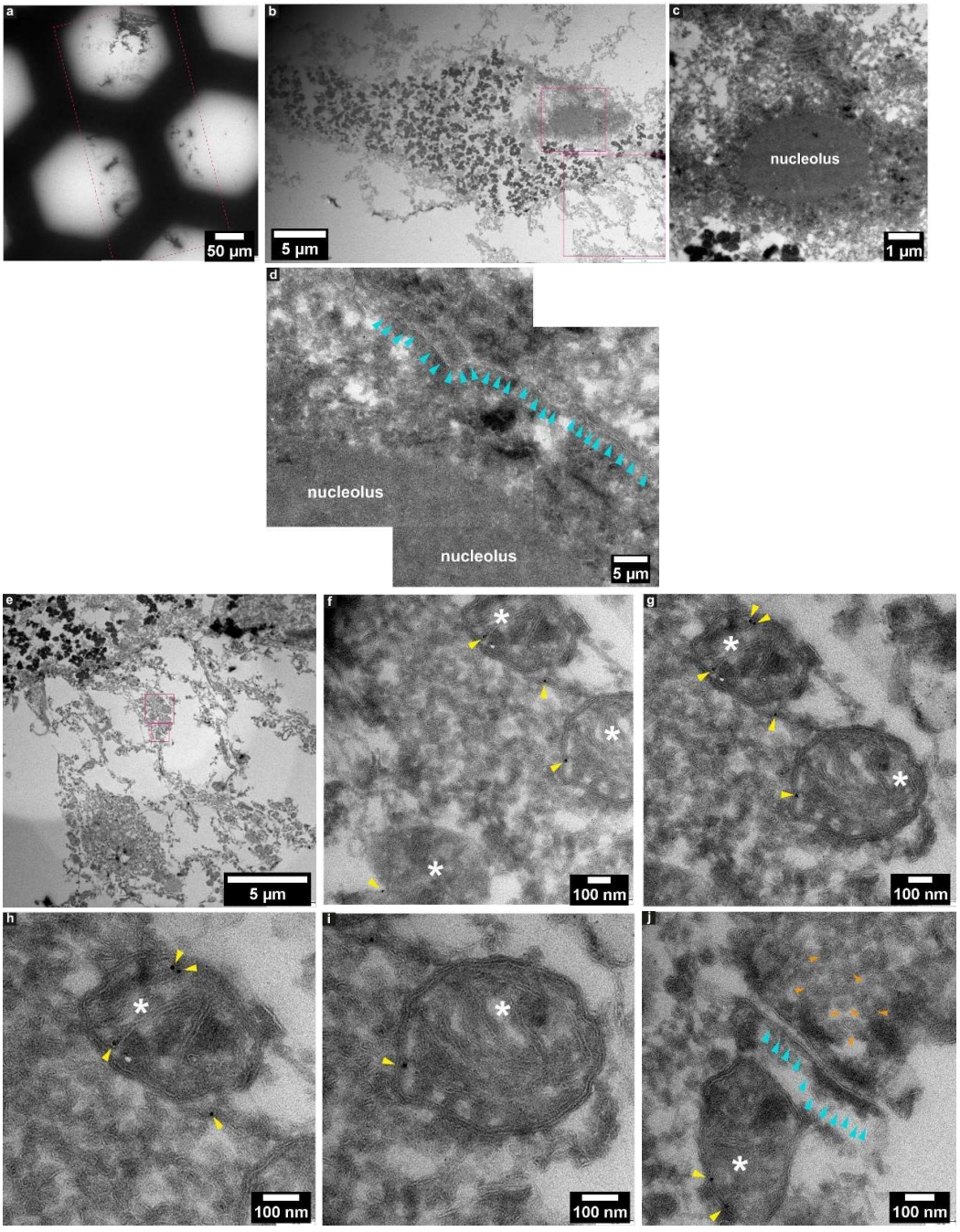

Figure 2.14: Immuno-electron microscopy of ultrathin tissue sections post cryo-PXCT imaging of non-demented control human brain.

After cryo-PXCT imaging, sections were generated by cryo-ultramicrotomy of the tissue block of non-demented control human brain (Tomo 5, Table 2.1) followed by immunogold labeling using anti-VDAC1 (mitochondrial membrane marker), standard uranyl acetate contrast enhancement, and electron microscopy. Images (a–c) show progressively zoomed-in views of a neuromelanin containing cell. (a) Overview of the ultrathin tissue sections (pink dotted box) on the formvar-carbon support film of a

hexagonal EM grid. (b) One neuromelanin-containing cell visible in a section zoomed-in from panel (a). Neuromelanin granules are the dark dense globules. (c) Zoomed-in view of the nucleus [top pink box in panel (b)] including the clearly visible nucleolus of the same neuromelanin-containing cell, (d) Zoomed-in view of a part of the same nucleolus within the nucleus of the neuromelanin-containing cell, in which the nuclear membrane (aqua arrowheads) is preserved and clearly visible. (e) Zoomed-in view of the region as shown in the bottom pink box depicted in panel (b), directly underneath the neuromelanin-containing cell, (f) three mitochondria (white asterix) zoomed-in from the top pink box as shown in panel (e), with anti-VDAC1 (outer mitochondrial membrane marker) immunogolds (yellow arrowheads) visible as expected on their periphery. (g) View of two of the same mitochondria as shown in panel (f) in which more immunogolds (yellow arrowheads) can be visible at the top of the top-most mitochondrion. (h) Zoomed-in view of the top-most mitochondrion (white asterix) as shown in panel (g) where four immunogolds (yellow arrowheads) are visible. (i) Zoomed-in view of the bottom mitochondrion (white asterix) shown in panel (g) where one immunogold is visible. (j) Zoomed-in view of the synaptic cleft as shown in the bottom-most pink box shown in panel (e), in which the membranes of the synaptic cleft (aqua arrowheads) are visible, a mitochondrion (white asterix) with two immunogolds (yellow arrowheads) visible on the post-synaptic side, and clusters of synaptic vesicles (orange arrowheads) visible on the presynaptic side.

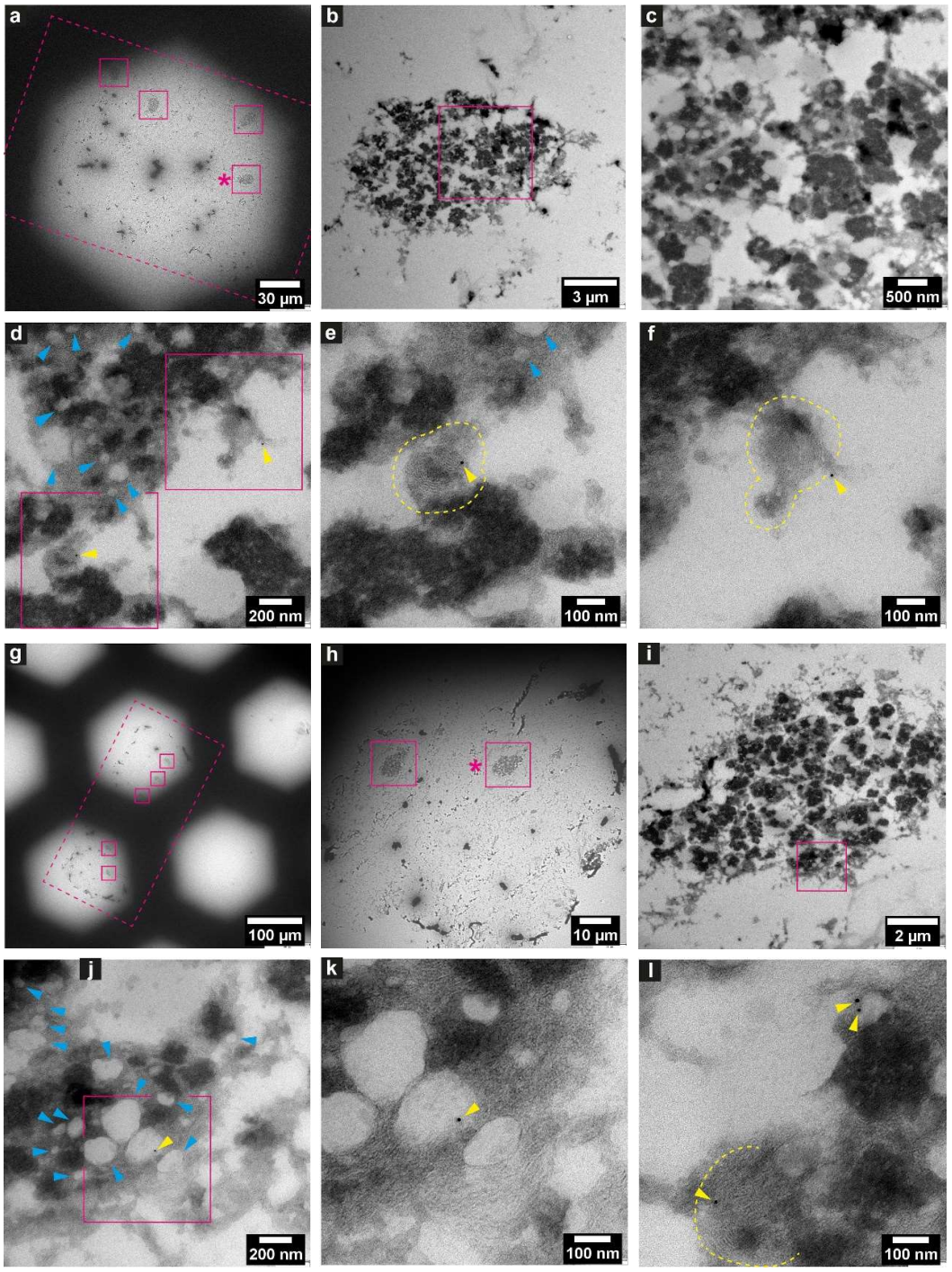

Figure 2.15: Immuno-electron microscopy of ultrathin tissue sections post cryo-PXCT imaging of PD human brain.

Immuno-electron microscopy of ultrathin tissue sections post cryo-PXCT imaging of Parkinson's diseased human brain. After cryo-PXCT imaging, sections were generated by cryo-ultramicrotomy of the

tissue block of Parkinson's diseased human brain (Tomo 2, Table 2.1) followed by immunogold labeling, standard uranyl acetate contrast enhancement, and electron microscopy. Images in panels (a–f) and (g–l) correspond to different tissue sections: (a–f) immunogold-labeled using LB509 (anti-alpha synuclein), and (g–l) immunogold-labeled for p-aSyn (anti- phosphorylated alpha synuclein at S129). Images show progressively zoomed-in views of a neuromelanin containing cell from each tissue section. (a) Overview of the ultrathin tissue sections (pink dotted box) on the formvar-carbon support film of a hexagonal EM grid, with neuromelanin-containing cells visible (pink solid boxes). (b) Zoomed-in view of neuromelanin-containing cell shown in pink box (asterix) in panel (a), and progressively zoomed-in view in panel (c) where lipid globules (pale gray globules) are clustered with neuromelanin granules (darker globules) as typically expected. (d) Zoomed-in view within the neuromelanin-containing cell where lipid globules are more clearly visible (blue arrowheads) and immunogolds (yellow arrowheads) for LB509 (anti alpha-synuclein) are visible. (e) Zoomed-in view of the bottom-most pink box shown in panel (d), and the (f) top-most pink box shown in panel (d), in which immunogolds for LB509 (anti alpha-synuclein) are visible, both on lamellar multi-membranous structures. (g) Overview of the ultrathin tissue sections (pink dotted box) on the formvar-carbon support film of a hexagonal EM grid, with neuromelanin-containing cells visible (pink solid boxes). (h) Zoomed-in view of neuromelanin-containing cell shown in pink box (asterix) in panel (g), and progressively zoomed-in view in panel (i) where lipid globules (pale gray globules) are clustered with neuromelanin granules (darker globules) as typically expected. (j) Zoomed-in view within the neuromelanin-containing cell where membrane-enclosed structures are visible (blue arrowheads) and immunogold (yellow arrowhead) is visible, (k) zoomed-in view of the region in pink box shown in panel (j), where immunogold is visible at the edge of a vesicle. (l) Another zoomed-in view of the neuromelanin-containing cell in which an immunogold is visible on another lamellar multi-membranous structure (delimited by yellow dotted lines) and two immunogolds are visible at the edge of a vesicle.

2.4 Discussion

Our results using cryo-PXCT on unstained human brain tissue samples have revealed that several key cellular components can be resolved at the nanoscale, including myelinated axons, neuromelanin-containing cells and their nuclei, the nuclei of other brain cells such as glia, red blood cells and blood vessels within the brain. We have demonstrated that resolution is sufficient to visualize fine details including changes between the myelin sheaths of axons, particularly clarifying the ultrastructural nature of swellings within axons in this case. Not only can such structures be clearly visualized, but also with sufficient resolution (145–390 nm) providing a level of detail that allows us to clarify whether these swellings are occurring within the actual axon or within the myelin sheath composing the axon, suggestive of different biological mechanisms. We have found that such swellings, or dystrophic myelinated axons (DMAs), appear only within the PD human brain tissue samples as compared to the control brain samples that we have imaged; in this case, in the SNpc brain region that is highly clinically relevant to this disease.

We have also shown that the majority of these DMAs occur within the myelin sheaths (**Figure 2.9, 2.10)** corresponding to the cytoplasm of the parent oligodendrocyte, in contrast to the expectation that they would occur within the main passage of the axon corresponding to the neuronal cell itself. This suggests that processes in which the oligodendrocytes, or cells that produce the myelin sheath, are involved in the pathology of PD. The number of reports on the role of oligodendroglial cells in neurodegeneration has increased substantially over recent years[91]. In addition to their well-known role of producing myelin that mediates action potential conduction and communication between neurons, oligodendrocytes also provide trophic support for axonal and neuronal maintenance. Typically, oligodendrocytes are implicated in diseases such as multiple systems atrophy (MSA), amyotrophic lateral sclerosis (ALS), and more recently, Alzheimer's disease (AD)[10]. Like PD, MSA is also mainly characterized by the abnormal accumulation of aggregates of the aSyn protein, albeit predominantly in oligodendrocytes rather than neurons[92]. Interestingly, this phenomenon can go "both ways": aggregates of aSyn in PD are predominant in neurons, but can also be found in oligodendrocytes[93–95]. This suggests that oligodendrocytes cannot totally be excluded from PD pathogenesis, and our observations pointing in such a direction are not implausible.

The pathological accumulation within the swellings in both oligodendrocyte cytoplasm and axoplasm appeared very granular (**Figure 2.7** and Supplementary Figures 2.1, 2.2). Indeed, correlative light and electron microscopy and tomography, and parallel studies using multi-labeling super resolution light microscopy, have recently shown a high lipid content and a crowding of vesicular structures including lysosomes and autophagosomes within both Lewy bodies and dystrophic axons corresponding to be Lewy neurites based on immunohistochemical staining[43]. Multiple studies have shown a potential link between disturbances in myelin integrity/myelin breakdown and axonal damage as an early event in the onset of neurodegenerative diseases including PD, AD, and Huntington's disease (HD), using magnetic resonance imaging (MRI)[96,97]. Furthermore, the occurrence of heightened tissue iron levels complexed with ferritin (produced in the brain mainly by oligodendrocytes) in PD, AD, and HD[96,98,99] is known to increase the concentration of reactive oxygen species[100] that can initiate changes in the proteins' tertiary structure, leading to aggregation that is associated with neurodegeneration. High tissue iron is considered as a risk factor in developing neurodegenerative disease, with oligodendrocytes playing a key role[87,101,102].

Considering that myelin represents a vital factor for human brain connectivity, is profoundly evolved in humans compared to non-human primates and other mammals, and progressively declines in the aging human brain, oligodendrocyte dysfunction would logically contribute to the vulnerability of the human brain in regard to neurodegenerative diseases. We have demonstrated that cryo-PXCT is a useful tool to simultaneously visualize several axons in a continuous volume, currently limited to ~$(100\ \mu m)^3$, without the addition of any stain, allowing the detection of subtle changes in axonal ultrastructure and enabling us to distinguish between types of swellings and furthermore the extent to which the axon is myelinated: thin myelin sheaths which are more frequently associated with neurodegeneration, as compared to thicker myelin sheaths which are more frequently associated with a healthier state[103,104]. While cryo-PXCT would hence be useful to investigate diseases in which neuronal, oligodendrocytes and axonal degeneration are majorly implicated, our unexpected finding of axonal swellings directly arising within the myelin sheaths originating from the parent oligodendrocyte rather than within the axoplasm of the associated neuron from the human postmortem PD brain, brings forth the question of whether other neurodegenerative diseases displaying axonal swellings may also involve oligodendrocytes in a similar manner. Such an

observation would have implications for disease pathogenesis and warrant closer investigation using complementary techniques.

Recognizing and differentiating abnormal features within the axon as opposed to those within the myelin sheath that encase the axon, is a crucial step toward pinpointing the underlying physiological and pathological processes. For example, abnormalities within the axon rather than the myelin sheath would implicate a cellular process that is specific to the parent neuron from which the axon extends. Abnormalities within the myelin sheath itself would correspond to pathologically relevant processes that are occurring within the parent oligodendrocyte cell from which the myelin sheath is produced. More specifically, each individual wrapping of myelin sheath around an axon protruding from a neuron, also contains its own cytoplasm that belongs to the oligodendrocyte cell producing that myelin sheath[105]. Since oligodendrocyte cells are different in both composition and function as compared to neurons, abnormalities arising in their cytoplasm are important to distinguish from abnormalities in the neuronal cytoplasm, and would refer to a pathological process attributable to a different – either separate or concerted – cellular mechanism[106].

Furthermore, we have demonstrated for the first time that after cryo-PXCT imaging, protein antigenicity is preserved, as demonstrated here by subsequent ultramicrotomy, immunogold labeling, and correlative electron microscopy (**Figures 2.13–2.15**), revealing the ultrastructure of cellular features including mitochondria, myelinated axons, synaptic clefts and the typical associated protein densities, synaptic vesicles, neuromelanin-containing organelles, nuclear membrane, nucleus and nucleolus, and various lipid vesicles. Our samples were fixed by gentle fixatives and embedded in sucrose to enable the preservation of protein antigenicity so the tissues' architecture was unstable and easy to fall apart after several incubation/washing steps of thawed ultrathin sections during staining process, which resulted in holes and gaps observed by TEM (**Figures 2.13–2.15**). In addition, they are aged human brains and some samples are aged diseased human brains so the gaps in the tissues are indeed from brain cells that have already died away. This demonstration has important implications for investigations which would greatly benefit from first generating a large map of complex, hierarchical multi-component features – typical to the crowded environment of biological tissues – by using cryo-PXCT, and subsequently imaging at higher resolution using correlative electron microscopy of target structures localized in the cryo-PXCT tomograms.

In general, X-ray ptychography has been shown to provide resolutions as high as 20 nm in 2D projections of single biological cryo-preserved cells[107]. There is potential for increasing the resolution in large tissue volumes such as the ones investigated here, as there are studies supporting that biological tissue could withstand doses up to 1e9 Grays, which is about 2 orders of magnitude more than the dose deposited by PXCT in our work, while preserving features at length scales well below 100 nm[108]. The development of diffraction-limited storage rings[109] and other improvements in instrumentation will allow to increase the coherent flux required for these experiments and thereby the spatial resolution could be increased up to the limit imposed by radiation damage within practical measurement times.

Moreover, high-pressure frozen biological samples, which are cryo-immobilized directly in their native state without chemical fixation/sucrose infiltration/staining to better preserve their ultrastructure can be also imaged by cryo-PXCT since the fundamental instrumentation of OMNY would be exactly the same as used to image our chemically-fixed, sucrose-infiltrated samples. However, the current sample carriers to high-pressure freeze biological samples are not compatible with cryo-PXCT instrument. Theoretically, it should be possible that biological samples are cryo-immobilized inside metal carriers[110] and then the frozen samples are mounted onto the head of an OMNY pin for cryo-PXCT imaging. Even though it is possible to trim frozen samples into small cubes for mounting inside the metal carriers directly by cryo-ultramicrotome, it is still very challenging to handle and attach them to OMNY pin's tip at cryo-temperature. Future works can develop compatible sample carriers which enable either simple transfer of frozen samples to an OMNY pin or direct imaging by cryo-PXCT after trimming by cryo-ultramicrotome.

We have shown that cryo-PXCT is a useful tool for visualizing several features in both control and diseased postmortem human brain tissue samples, and for facilitating detection of subtle ultrastructural differences amongst structures that continuously span the examined tissue volumes, especially axons in this case. Evidence suggests that changes to axonal ultrastructure are considered as one of the early events in neurodegeneration, thereby justifying closer nanoscale-based investigations. For example, the appearance of neurite swellings marks an early event in neuritic degeneration in Parkinson's diseased patient-derived neurons[42], and dystrophic axons and alterations in axonal transport induced by overexpression of mutant alpha synuclein (p.A53T) in rats are known to precede neuronal loss[37].

Although our cryo-PXCT study generated five datasets from a single control aged human brain and four datasets restricted to a single age-matched PD brain donor, the unexpected finding of expansions and aggregations in myelin sheaths corresponding to the cytoplasm of the parent oligodendrocytes in the PD brain suggests a closer investigation of such processes in PD and other neurodegenerative conditions. Our results also prove cryo-PXCT as an appropriate tool for imaging such phenomena and related ultrastructural changes at the nanoscale. More remains to be clarified on samples taken from more patients, how such dense cytoplasmic aggregations arise within the parent oligodendrocytes, their specific relation with the dominant pathological form of alpha synuclein (phosphorylated Ser-129)[111], and why they occur at specific points along the axon. Investigating across PD brains of different disease stages (Braak stages) and quantifying both the incidence and heterogeneity at the nanoscale of such DMAs may also prove to be useful in uncovering new aspects of the disease progression. Furthermore, our results warrant further investigations in other neurodegenerative diseases in which oligodendrocytes and axonal abnormalities are primarily involved, to yield a better understanding of subtle nanoscale changes that occur in different disease states and stages.

2.5 Conclusion

Here we have shown for the first time that nanoscale label-free imaging of diseased human brain tissues using hard X-rays can visualize several ultrastructural features and provide insight to pathologically relevant processes spanning continuous volumes. Our successful demonstration of downstream electron microscopy, and immunogold labeling for electron microscopy, post cryo-PXCT imaging on human brain tissue is anticipated to finally open the doors for clarifying the identity and ultrastructure of nanoscale biological features in large volume X-ray tomographic data. While the imaging rate of cryo-PXCT is currently comparable to destructive methods, with synchrotron upgrades occurring worldwide according to the multi-bend achromat and additional beamline improvements we expect an increase in coherent photon flux by up to four orders of magnitude, and thus a dramatic increase in imaging rate and/or resolution[55]. This will allow increasing the number of samples studied for a wider investigation.

Chapter 3 A Compartmentalized Neuronal Cell-Culture Platform Compatible with Cryo-Fixation by High-pressure Freezing for Ultrastructural Imaging

This chapter is based on a manuscript to be submitted to *Frontiers in Neuroscience, Neural Technology section; Hung Tri Tran, Sarah H. Shahmoradian, Takashi Ishikawa, Celestino Padeste*; in preparation.

3.1 Introduction

Studying individual neurites in defined neuronal circuits, and especially determining how specific neurons interact within the complex nervous system remains a challenge. Since human brains contain large numbers of neurons and interconnections, delimiting and characterizing specific targets and their interactions is a major issue. Therefore, well-designed cell culture models are needed to provide key insights while circumventing complex issues associated with handling human brain tissue.

An often pursued approach towards modeling of neuronal circuitry in culture is compartmentalization. Compartmentalized culturing systems, which are commonly created using microfabrication technology and soft lithography, enable the physical isolation of different cell populations as well as the sectioning of neuronal soma from neurites[112]. Various advanced versions of such devices have been used for neurobiological studies of neuron cell development and degeneration, thus capitalizing on the ease of fabrication, reproducibility and cost effectiveness.

For example, a PDMS device with additional microfluidic local perfusion chambers was fabricated to access synaptic regions with high spatial and temporal resolution[32,113]. The microfluidic local perfusion chamber provided a novel approach for local manipulation and study of synapse connections between a “presynaptic” and a “postsynaptic” compartment by diffusion of soluble substances. This unique design was also utilized to reconstruct corticostriatal neuronal circuits *in vitro*, providing a microfluidic platform to investigate molecular mechanisms that occur in neuronal circuits, to elucidate pathogenic mechanisms,

and to identify potentially effective drug treatments [114,115]. Another example of a compartmentalized microfluidic system for neurobiological cell culture utilizes asymmetric microfluidic channels for unidirectional axonal guidance from a presynaptic sub-population to a postsynaptic sub-population of the neurons to study predefined neuron connectivity *in vitro* [116–119].

Such compartmentalized microfluidic devices are well-controlled systems compatible with optical microscopy to enable investigation of cellular dynamics with subcellular resolution. However, these devices are often not compatible with vitrification, or cryo-fixation (no chemical fixatives), by means of high-pressure freezing[120] for optimal high-fidelity ultrastructural imaging using approaches such as electron microscopy. Therefore, cellular processes occurring at the nanoscale within such microfluidic devices cannot easily be captured in a near-native state. Currently, cells grown in compartmentalized devices are prepared by more traditional routes for electron microscopy; instead of cryo-fixation, they undergo chemical fixation, subsequent staining using a cocktail of heavy metals to generate high contrast, and dehydration procedures, prior to electron microscopic imaging. Such steps are well-known to potentially introduce artifacts and structural or chemical changes inside biological specimens, which is why cryo-fixation for freeze-substitution and electron microscopy, or cryo-fixation followed by cryo-electron microscopy and tomography, are beginning to take precedence as more high-fidelity approaches for addressing biological questions[121].

Cryo-fixation by techniques such as plunge-freezing or high-pressure freezing has emerged in recent decades as the best way to preserve biological samples for ultrastructural studies, i.e. by electron microscopy[121–123]. Cryo-fixation by high-pressure freezing enables the frozen-hydrated preservation of molecules inside the sample within milliseconds by rapidly chilling the sample to liquid nitrogen temperatures at extremely high pressure (2100 bar). Under these circumstances, the ice nucleation and distortion of specimens during solidification by freezing are minimized: intrinsically contained water turns into vitreous ice even in the absence of cryo-protectants. This results in preserving the cellular architecture[124] without requiring the use of any chemical fixatives, hence capturing a near-native, physiologically-relevant state. Since this type of freezing occurs on the order of milliseconds, highly dynamic cellular events can be captured with high molecular fidelity.

Plunge-freezing also is used to achieve vitreous ice, albeit for thinner samples (<100 nm; typically restricted to macromolecular complexes in solution, or thin cell culture monolayers) as compared to those for high-pressure freezing (up to 200 µm thick samples, such as a wide variety of cell culture or tissues)[125]. Primary neurons as well as other cell lines have been grown directly atop electron microscopy (EM) grids, which can be plunge-frozen and examined with cryo-electron tomography to study neuronal synapses in a nearly native state[126–129]. While these systems are useful, typically they utilize only one type of neuron, and further lack any guidance or growth control in a compartmentalized fashion. Indeed, it is very challenging to fabricate a guiding chemical pattern or structure atop EM grids due to size and sensitivity constraints: EM grids are very delicate and relatively small (Ø 3mm), often containing thin and holey substrates (carbon, formvar) for cell culture compatibility that further complicate them for conventional micro-patterning methods. Micro-contact printing is one approach that has been applied successfully to fabricate protein patterns on EM grids to study the cellular mechanism of dynamic actin cytoskeleton self-organization by electron tomography[130]. However, after physical contact between the PDMS stamp and substrate to transfer the protein pattern, the removal of grids from the stamp was shown to cause damage to the EM grid surface integrity. Recently, a mask-less photo-patterning has been developed, which can overcome this problem by eliminating physical contact between the stamp and delicate substrate[131]. This method enables contactless fabrication of protein patterns on EM grids using light-induced molecular adsorption[132–134]. Although this is an innovative approach to create protein micro-patterns on EM grids for biological research, it still requires further development to make it sufficiently suitable for neurobiological research, i.e. of compartmentalized neural circuits.

Among different sample carrier systems for high-pressure freezing, sapphire discs are well suited for cell culture including neuronal cell culture. They possess sufficient strength to withstand the high pressure during fixation, have sufficient optical clarity for enabling correlative light and electron microscopy studies, and can easily be coated for culturing different types of cells including neurons. Dissociated primary neurons have been shown previously to be cultured on sapphire discs for subsequent downstream processing by high-pressure freezing, freeze substitution, sectioning and investigation by electron microscopy to investigate subcellular compartments or organelles [135]. The possibility to capture neurons in

their native state also provided snapshots of membrane dynamics at synapse junctions under light stimulation with milliseconds temporal resolution [136]. However, cryo-fixation methods are not compatible with conventional cell culture set-ups using microfluidic chambers, and there are only limited systems reported which are compatible with neuronal cell cultures.

In our work reported here, we developed a compartmentalized platform, which is uniquely compatible with cryo-fixation by high-pressure freezing followed by freeze substitution to reconstruct compartmentalized neuronal circuits *in vitro* for high fidelity ultrastructural imaging of subcellular structures by methods including electron microscopy. The system allows co-culturing of different populations of neural cells to mimic physiologically-relevant neuronal pathways as they exist in the brain, such as corticostriatal or nigrostriatal, or to establish artificial neuronal networks. We fabricated a PDMS device with an embedded microstructured sapphire disc, which is designed in such a way to enable co-culturing of two groups of primary neurons or other neuronal cell lines. The neuritic extensions from the different groups of neurons placed in the two separate compartments are guided by a channel array, which was lithographically fabricated in an SU-8 photoresist on the sapphire discs, and further coated with a suitable neuronal attachment solution. The versatility of our device makes it useful not only for the investigation of ultrastructural features of neuronal networks but also for circuit-level studies of brain diseases and neurological disorders characterized by network dysfunction.

3.2 Methods

3.2.1 Fabrication of microstructures on sapphire discs

Polymeric microstructures for neurite outgrowth guidance were lithographically fabricated on 6 mm sapphire discs (Leica Microsystems, Switzerland), which were cleaned with Piranha solution (2:1 vol $H_2SO_4 : H_2O_2$) at 90°C for 1 hr. The discs were then landmarked by carbon evaporation (MED010, BalTec AG, Switzerland) through a finder grid mask (Leica Microsystems, Switzerland) and baked at 190°C for 6 hrs. to stabilize carbon pattern. A 6 µm layer of SU-8 photoresist (SU-8 5, MicroChem Corporation, Newton, MA, USA) was spin-coated on the sapphire discs at 500 rpm (200rpm/s acceleration) for 5 s and 2000 rpm for 40 s (500 rpm/s acceleration). It was soft baked at 65°C for 1 min, 95°C for 3 min and then exposed at 365 nm wavelength at a dose of 100 mJ/cm^2 (Karl Suss, MJB3) using a chromium mask

produced with standard e-beam lithography. Following a post expose bake at 65°C for 1 min and 95°C for 1 min. The structures were developed in AZ® EBR Solvent (Microchemicals GmbH, Germany) for 1 min and hard baked at 190°C for 30 min on a hot plate to further crosslink the SU-8 photoresist. The profile of final structure was measured using a Veeco Dektak 8 profilometer.

3.2.2 Fabrication of the PDMS chamber

The device to enable co-culture of neurons in separate areas on sapphire discs (Figure 1) consists of components which were fabricated in PDMS (Sylgard 184, Dow Corning) using a mixture of silicone elastomer and its curing agent in a ratio of 10:1. Crosslinking was done at 80°C for 1 hr. A circular PDMS substrate (Ø 30mm, thickness 3mm) was fabricated, using a sapphire disc as a mold to create a cavity that fits perfectly to sapphire disc. It was then punctured to create circular hole (Ø 4mm) concentrically to the Ø 6mm cavity to enable neuron live-imaging on an inverted microscope. This substrate was placed manually on top of a stainless steel plate (Ø 35mm, thickness 0.2mm) with a circular hole (Ø 4mm) in the center prepared by laser cutting. The PDMS substrate and metal plate were manually aligned using their Ø 4mm holes. The patterned sapphire disc was placed into the Ø 6mm cavity of circular PDMS substrate. A PDMS ring (inner Ø 15mm / outer Ø 30mm, thickness 3mm) with a square glass spacer (20mm x 7mm, thickness 160-190µm) in the center to divide it into two separated chambers was placed on top of the PDMS substrate containing patterned sapphire disc under a stereo microscope, and the glass spacer was aligned to cover the parallel ridges of the photoresist structure. The assembled device was oxygen plasma treated for 1 min and sterilized by 70% ethanol. To promote attachment and growth of neurons 0.15 ml of 0.01% Poly-L-lysine solution (Catalog # 3438-100-01, Trevigen, Gaithersburg, MD, USA) was added to the chambers and incubated for 2 hr at room temperature (0.15ml/cm^2). The device was then washed 3 times with H_2O, dried under the tissue culture hood and stored at 4°C until neuron culture. Alternately, for PC12 differentiation experiments, the device was coated with collagen type IV (C5533, Sigma-Aldrich) reconstituted in sterile 0.25% acetic acid. After sterilization by EtOH, 600 µl of 0.023mg/ml collagen type IV solution was added to PDMS device and incubated over night at 37°C. The coating solution was then removed and device was airdried, and stored at 4°C until use.

3.2.3 Cell cultures

Primary striatal neurons were dissociated from E18 rat embryo brain tissue (BrainBits LLC, USA) and hippocampal neurons were dissociated from P0 mouse pups (courtesty of E. Pecho-Vrieseling, University of Basel, Switzerland). The dissociation was performed according to detailed protocols from BrainBits LLC (www.brainbitsllc.com). The dissociated neurons were seeded onto the samples at an optimized density (16.000 cells/cm^2 for embryonic hippocampal neurons and 32.000 cells/cm^2 for postnatal hippocampal neurons) in NbAct1 media (BrainBits LLC, USA) and were grown for up to 21 days in a humidified cell culture incubator with 5% CO_2 at 37°C.

PC12 cells were obtained from ATCC (Catalog # CRL-1721) and cultured in DMEM media supplemented with 10% heat-inactivated horse serum, 5% fetal bovine serum and 1% penicillin-streptomycin. Cells were cultured in poly-l-lysine coated petri dishes (0.01% solution, 0.15ml/cm^2) and the culture medium was refreshed every three days. For differentiation experiments, PC12 cells were harvested and transferred to a collagen coated PDMS device in DMEM media supplemented with 1% heat-inactivated horse serum, 1% penicillin-streptomycin and 100ng/ml NGF at cell density 1000 cells/cm^2. PC12 cells cultures were maintained at 37°C, 5% CO_2 and the media was replaced every two days.

After cells were growing for a defined period of time, the PDMS device was disassembled and sapphire disc was removed from PDMS substrate. Cells cultivated on the sapphire discs were then fixed by standard chemical means or high pressure freezing for downstream investigation.

3.2.4 Immunostaining

Neuron cultures were fixed on day 14 in a 4% paraformaldehyde diluted in filtered PBS solution (pH 7.4) for 10 min at room temperature. After fixation, neurons were washed three times, 5 min each with a permeation buffer containing 0.05% Triton X-100 and 1% bovine serum albumin (BSA) in PBS. Then the fixed cells were incubated in Anti-DARPP32 primary antibody (Abcam ab40801) diluted 1:200 in permeation buffer supplemented 3% normal goat serum for 24 hours at 4C. After primary antibody incubation, the cell cultures were washed three times, 5 min each with permeation buffer and were incubated in a secondary antibody

solution (Alexa Fluor 488 anti-rabbit, Abcam ab150077 at 1:200 dilution) for 1 hr at room temperature. The labelled neurons were fluorescently visualized in PSB solution on a confocal microscope (Leica SP5) with a x20 objective.

3.2.5 Lentivirus production and transfection

HEK293T cells were plated at a density of 50% in DMEM media containing 10% fetal bovine serum and 1% penicillin-streptomycin in 175 cm^2 cell culture flask 24 hr before transfection. A mixture of 24 µg lentiviral transfer plasmid pLV-eGFP (#36083, Addgene, USA) or 24 µg pLV-mCherry (#36084, Addgene, USA) with 8 µg each 3rd generation viral packaging vectors: pMDLg/pRRE (Addgene plasmid # 12251) pRSV-Rev (Addgene plasmid # 12253) pVSV-G (Addgene #138479) was prepared. The DNA mixture and PEI (branched polyethylenimine, Sigma-Aldrich,1 mg/ml) were mixed at the ratio of 1:3 in a total volume of 2 ml of OptiMEM media (Gibco) and incubated at room temperature for 10 min to form complex before transfection. Then, the mixture was added to the cells to initiate the transfection.

The supernatant containing virus from transfected HEK293T was harvested at 48h and 72h post transfection in a combined harvest where all the individual harvests were pooled. Each harvested media was stored at 4°C between harvests. The viral supernatant was centrifuged at 200g for 5 min at room temperature to pellet any cell debris that was collected during harvesting. Then, it was filtered through a 0.45 µm filter and concentrated by Polyethylene Glycol (PEG) precipitation. The PEG solution was prepared by dissolving 85g PEG 6000, 17.5g NaCl in 25 ml 10x PBS and 100 ml sterile water and stored at 4°C until use. The PEG solution was added to filtered virus supernatant at ratio 1:3 and final PEG and NaCl concentration will be 8.5% and 0.3M respectively. After gently mixing, it was stored overnight at 4°C. Next, the mixture was centrifuged at 1600g for 1 hr at 4°C. After gently aspirating the liquid, the pellet was resuspended in 1/250 of the original volume of cold PBS. The virus suspension was aliquoted and stored at -20°C. For transduction of PC12 cells, concentrated virus suspension was added to undifferentiated PC12 cells, which were growing poly-l-lysine coated petri dishes. Two days after transduction, PC12 cells were harvested and transferred to a collagen coated PDMS device for differentiation.

For transduction of primary neurons, following dissociation, the concentrated virus was immediately added to neuron suspension in NbAct1 media (BrainBits LLC, USA) and incubated

for 1.5 hr at 37°C, 5% CO_2. After that, the cells suspension was centrifuged at 1100 rpm for 3 min to remove virus and cells pellet was resuspended in warm NbAct1 media (BrainBits LLC, USA). The infected neurons were seeded onto PDMS device, grown for up to 21 days, and imaged by confocal microscopy.

3.2.6 SEM imaging of neuron cultures

Neurons were chemically fixed by 4% paraformaldehyde diluted in filtered DPBS pH 7.4 for 10 min at room temperature. Cells were then rinsed 3 times with DPBS, 3 times with distilled water. Dehydration was performed through a graded series of ethanol beginning with 25% EtOH (1 x 5 min), followed by 50% EtOH (1 x 10 min), 75% EtOH (1 x 10 min), 95% EtOH (1 x 10 min), and 100% EtOH (3 x 10 min). The samples were then quickly transferred in 100% EtOH to critical point dryer (EM CPD300, Leica Microsystems, Switzerland) for drying by liquid CO_2. Neurons always remained immersed in liquid in between the washing steps and during transfers to avoid any intermediate drying. After critical-point drying, the samples were sputter coated with ultrathin gold layer (SPI-Module Sputter Coater, Structure Probe, Inc., USA) and imaged by Scanning Electron Microscopy (ZEISS NVision40).

3.2.7 High pressure freezing

Sapphire discs with growing neurons were mounted face-up into a plastic 6mm middle plate, and a metal spacer ring (Ø 6mm, 100 µm thickness) was then placed on top. Before capping the assembly with another bare sapphire disc to form a sandwich, a droplet of neuron culture medium was added in order to protect the neurons in a small liquid chamber. The sandwich was then simultaneously pressurized at high pressure (2100 bar) and frozen at liquid nitrogen temperatures using a Leica EM ICE high pressure freezer (Leica Microsystems, Switzerland). Frozen samples were stored in liquid nitrogen for downstream processing and imaging.

3.2.8 Freeze substitution

Neuronal cell cultures on sapphire discs were high pressure-frozen at PSI, then transported in liquid nitrogen to ScopeM (ETH Zurich). Samples were subjected to freeze-substitution in acetone, dried over molecular sieve and supplemented with 0.5 % uranyl acetate (Polysciences; added from a 5 % stock solution in methanol) and 1 % osmium tetroxide (Polysciences). 5% double distilled water was added to the FS-cocktail, to improve visibility of membranes [137].

The samples were kept at -90 °C for 3 h, then warmed gradually to -20 °C at 5 °C/h, left at -20 °C for 2 h, then warmed to 0 °C at 10 °C/h, and left 1 h at 0 °C, before bringing them to room temperature and letting them adapt for 1 h. Then, samples were rinsed twice in dry acetone, microwave-assisted (Pelco BioWave, Ted Pella Inc., California, US). For resin embedding, the samples were infiltrated using 30 % Epon (Fluka Epoxy Embedding Kit) in dry acetone twice, microwave-assisted, followed by two changes of 70 % Epon. Then samples were subjected to three changes of 100% Epon for 1.5 h each, at RT on a shaker, before transferring them into molds with fresh resin and polymerization for 3 days at 60 °C. After polymerization, sapphire discs were detached by briefly dipping the warm resin block into liquid nitrogen, leaving the cells embedded in the resin block.

3.2.9 Ultrastructural imaging

For FIB-SEM (NVision 40, Zeiss), the resin block was trimmed to approximately 5 mm height and glued to a SEM-stub using silver conductive epoxy glue (CircuitWorks; Chemtronics, Hoofddorp, The Netherlands) and allowed to dry for one day at room temperature. Identification of a ROI and FIB-SEM imaging was performed as previously described in [2]. Briefly, by increasing the acceleration voltage to 15 kV and thus increasing the interaction volume of the electron beam with the sample, backscattered and secondary electrons could be detected selectively within the resin block, revealing the cells stained with heavy metal salts for precise positioning of the trench-milling. Milling a trench to expose the cells for imaging and imaging conditions were applied as described [138].

For TEM, small series of ultrathin sections (50-60 nm thickness) were obtained with a diamond knife (Diatome Ltd., Switzerland) on a Leica UC6 ultramicrotome (Leica Microsystems, Heerbrugg, Switzerland), collected atop Formvar- and carbon-coated slot grids (Quantifoil, Großlöbichau, Germany), and subsequently stained with 2% aqueous uranyl acetate and Reynold's lead citrate for 30 seconds each. Stained sections were then visualized using a Morgagni 268 TEM at 100 kV (FEI Company, Eindhoven, The Netherlands). As the neuronal cells and their neurites can cover an area of several hundreds of microns, overlapping images were collected that follow neuritic processes at high magnification. These image series were stitched into one large image using the TrakEM plugin of Fiji [139].

3.3 Results

3.3.1 Neuron co-culture system: Device concept and fabrication

The central piece of the device presented here consists of a 6mm sapphire disc with a structure with parallel ridges, used to separate two co-cultured cell populations (**Figure 3.1**). Sapphire discs were selected as the material of choice for a platform base due to their extremely high heat conductance withstanding the high-pressure freezing process and their optical transparency required for the light microscopic characterization prior to freezing, i.e. correlative light and electron microscopy[140,141]. A finder grid consisting of a thin carbon layer was deposited on the sapphire disc to generate a spatial "map" on the surface for localization of regions of interest for downstream processes including correlation of structures by light microscopy to electron microscopy (**Figure 3.1)**. SU-8 was chosen as material to fabricate the structures due to its biocompatibility with neuronal cultures [142]. Furthermore, SU-8 is a commonly used material for successfully producing structures with heights of 10-100 µm, and with high aspect ratios. The microstructures divide the center region of the sapphire discs into smaller areas to enable visualization of individual neurites by optical microscopy. The length of the microchannels was designed to increase the probability of capturing synaptic connections in the channels between ridges further downstream by electron microscopy. However, it is very challenging to trace individual neurites from synapse to their respective neuronal cell bodies in long channels because the imaging area of electron microscopy is limited as compared to optical microscopy. Hence, the length of channels was set to 200µm to balance those requirements. The width of channels was minimized to increase the probability of neurites' encounters to establish synapse connections between neurons. In addition, narrow channels were utilized to prevent the neurons themselves (soma) from migrating into channels from their respective separated compartments.

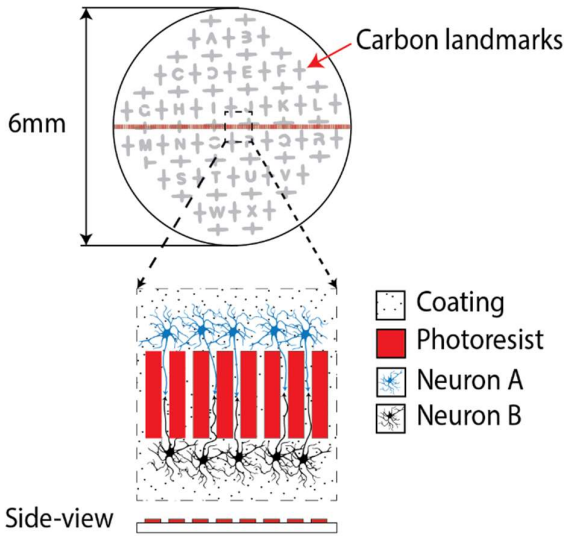

Figure 3.1: Schematic of the microstructured sapphire discs used as cell-growth substrates.

Parallel ridge structures are lithographically fabricated on sapphire discs using a biocompatible SU-8 negative tone resist. The structures are guiding neurites originating from neurons of two different populations for neuronal circuits' reconstruction. An evaporated carbon pattern serves as landmarks in the downstream processing.

Photolithography onto 6mm sapphire discs is a major challenge, as all the processes from spin-coating to photolithographic exposure are optimized for far larger substrates. Inhomogeneity of the photoresist layer, due to the incompatibility of such small (6mm) sapphire discs with the standard spin-coating process, prevents its close contact with the photomask during exposure to UV light for crosslinking to ultimately achieve highly resolved microstructures. Therefore, to improve the spin-coating process onto the 6 mm sapphire discs, the discs were mounted into a cavity in the center of a circular sample holder (Ø 15mm) made from PDMS (**Figure 3.2)**. These perfectly fitting cavities were prepared by placing similar sapphire discs in the center of the molds used for PDMS. These "perfect-fit" cavities were prepared by placing sapphire discs in the center of the molds used for PDMS. After mounting, a completely flat surface with an optimally larger surface area (as compared to the small sapphire disc itself) was hence created, which significantly facilitated the spin-coating process to achieve a thin and homogenous layer. However, structure defects, e.g. residues of photoresist in the region between ridges, have been encountered frequently (**Figure 3.3**). This is due to the so-called edge bead formation after the baking process used to dry the thin photoresist layer (**Figure**

3.4). To overcome this issue, the edge beads of photoresist on top of 6mm sapphire discs were removed manually using an acetone-dipped cotton swap (**Figure 3.5**). As the result, well-defined parallel ridge structures with multiple designs could be fabricated successfully by standard photolithography on 6 mm sapphire discs (**Figure 3.6a-e**). The minimal distance between ridges that were fabricated was ~10 µm and structure heights of 5-6um were achieved, which is more than the 3 µm reported to be needed to prevent neurites crossing over them[143] (**Figure 3.6f**). Patterned sapphire discs were coated with either poly-L-lysine or collagen to facilitate the attachment and growth of neuronal cells, which are typical coatings[136,144].

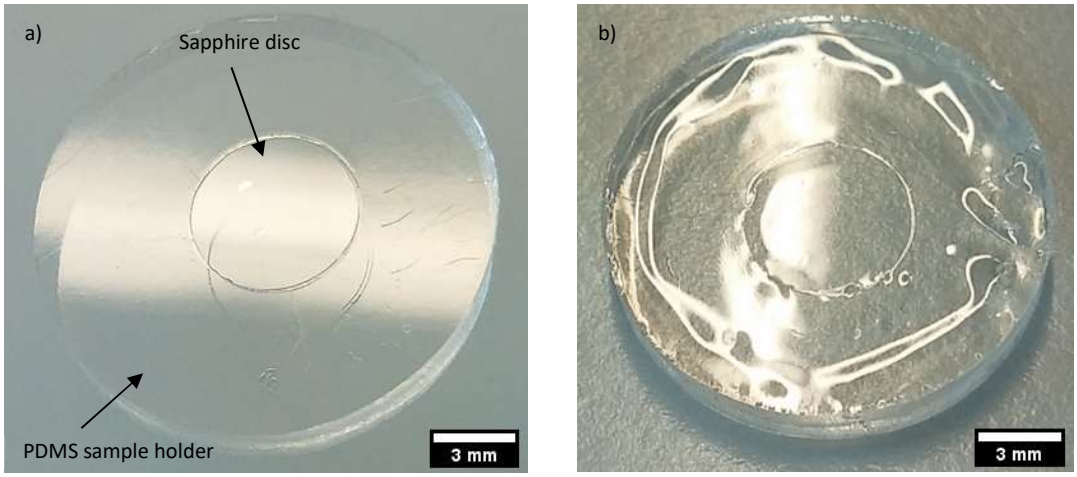

Figure 3.2: A sample holder to improve spin-coating process on the 6mm sapphire discs.

(a) Image of sapphire disc inside the PDMS sample holder. (b) Spin-coated SU-8 photoresist layer on sapphire disc with support of PDMS sample holder.

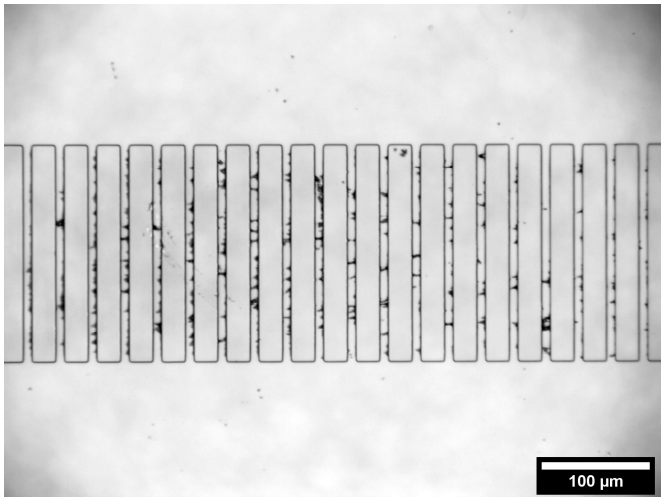

Figure 3.3: Defects of the structures.

The residue of photoresist exists in the region between ridges.

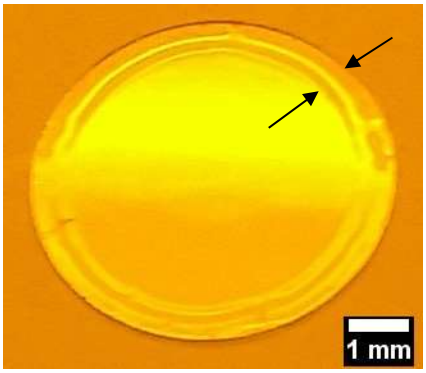

Figure 3.4: Formation of edge beads on the edge of sapphire disc after drying the photoresist thin film.

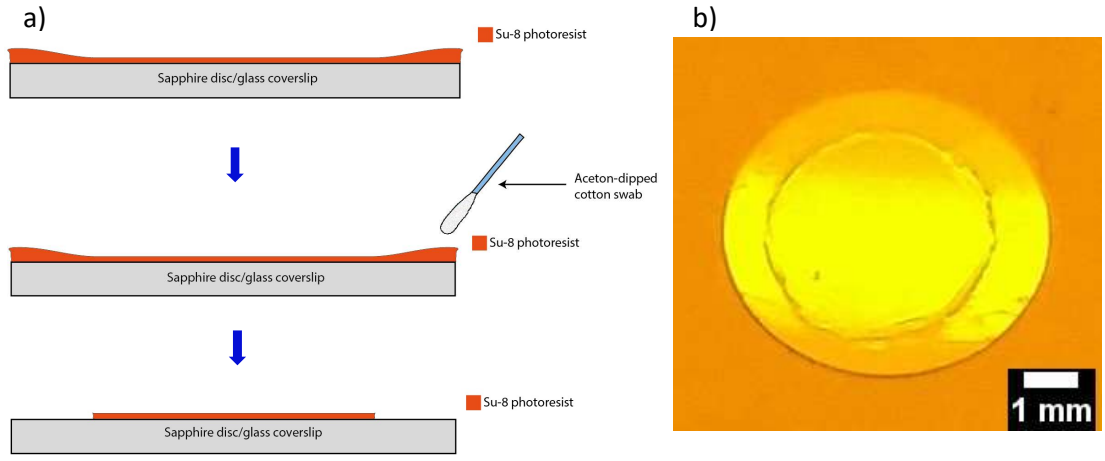

Figure 3.5: Removing edge beads manually by aceton-dipped cotton swap.

a) Procedure of manual removing edge beads atop spin-coated 6mm sapphire disc; b) Spin-coated 6mm sapphire disc after removing edge beads.

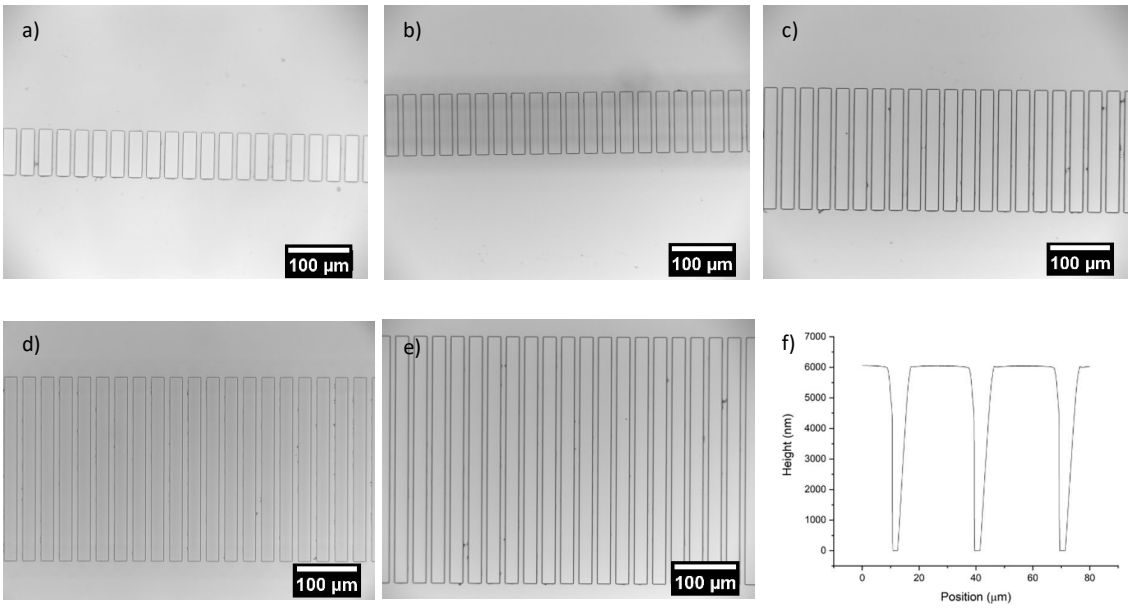

Figure 3.6: Parallel ridges structures with multiple designs on sapphire discs.

(a) Length: 75 µm, Width: 20 µm, Spacing 10 µm; (b) Length: 100 µm, Width: 20 µm, Spacing 10 µm; (c) Length: 200 µm, Width: 20 µm, Spacing 10 µm; (d) Length: 300 µm, Width: 20 µm, Spacing 10 µm; (e) Length: 400 µm, Width: 20 µm, Spacing 10 µm; (f) Thickness of the microstructures, measured by profilometer.

In order to co-culture two distinct groups of neuronal cells onto the different compartmentalized regions of the patterned sapphire discs, we fabricated a circular PDMS substrate with a cavity in the center to mount the patterned sapphire disc for integration into a larger device **(Figure 3.7)**. The patterned sapphire disc fit perfectly into the cavity, creating an even, flat surface with an optimally larger surface area. Afterwards, a PDMS ring divided into two parts by a glass spacer was aligned and attached onto the patterned sapphire disc for compartmentalized cell seedings (**Figure 3.7**). The glass spacer was aligned under a stereo-microscope to cover the microstructures on sapphire disc in order to prevent attachment of the neurons on the patterned area. This set-up enabled close contact between the PDMS chamber - including glass spacer and PDMS substrate - to form a closed system, which prevented culture media from leaking. The PDMS material underneath sapphire discs was removed by puncture to enable direct observation of neurons atop the sapphire discs by inverted microscopy without appreciable light scattering. Moreover, the PDMS circular substrate was fabricated with minimal thickness to reduce the distance between the objective lens of the microscope and the sapphire disc for high-resolution imaging. To stabilize this highly flexible PDMS substrate, it was placed and aligned manually on top of a stainless steel ring. Usually, the bonding between PDMS parts and substrates is critical for making microfluidic devices. High bonding strength is required to ensure leak-tight encapsulation; for instance, irreversible bonding is achieved by activating the surfaces of both the PDMS species and the glass substrates with a plasma treatment and bringing them into contact. However, this type of bonding introduces limitations to internal accessibilities of the devices and inhibits later disassembly, which would be required in the case of making such microfluidic-type compartmentalized devices for cell culture purposes. Alternatively, PDMS substrates can be sealed reversibly to other flat substrates by simply relying on hydrophobic interactions[112,145,146]. This concept was followed for our devices, as the glass spacer is the only part that has close contact with the patterned sapphire disc; furthermore, it does not make any direct bond with photoresist structures. Furthermore, easy disassembly is crucial for further downstream processing. No surface modification of the PDMS substrate and the PDMS ring was done prior to assembly to avoid excessively strong bonding.

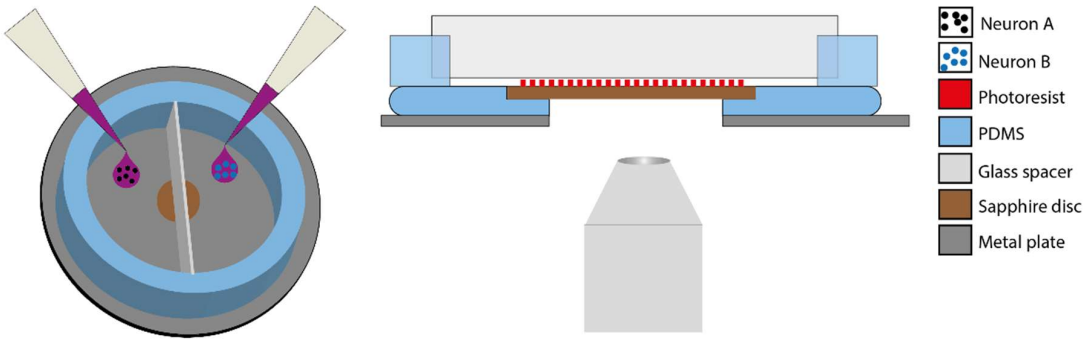

Figure 3.7: Schematic illustration of an assembled device allowing compartmentalized co-culture of different cell populations.

The device includes two main components: a PDMS ring with a glass spacer to from two isolated chambers for co-culture, and a PDMS base with a central hole holding patterned sapphire. The whole system is placed on top of a stainless steel ring as a support. The assembled device is compatible with light microscopes to enable correlative light-electron microscopy.

Following assembly, watertight chambers were formed due to adhesion by van der Waals forces between the PDMS pieces due to the intrinsic hydrophobicity of PDMS material (**Figure 3.8a**). No culture media leak from the chambers was noted for up to 21 days in culture at 37°C, 5% CO_2. Features of the assembly remained clearly visible by optical microscopy (**Figure 3.8b**). The glass spacer was aligned precisely on top of the photoresist ridge structures and carbon landmarks were visible by optical microscopy as well (**Figure 3.8b**). The design of this device permits for simple disassembly, and the sapphire discs could be removed from the PDMS chambers easily without damaging the reconstructed neurons and their neurites, for further downstream processes.

The constructed neuronal networks were then subjected to a workflow of processes toward ultrastructural imaging by electron microscopy: first, from cryo-fixation via high pressure freezing, followed by freeze substitution and embedding in resin (**Figure 3.9**). The resin-embedded cells were then in an optimal state for being subjected to multiple methods for ultrastructural imaging, i.e. focused ion beam-milling scanning electron microscopy (FIB-SEM) or physical sectioning by a diamond knife for high resolution imaging by transmission electron microscopy (TEM). The same type of physical sectioning by diamond knife could also be easily

utilized for serial block-face scanning electron microscopy (SBF-SEM), but was not demonstrated in this specific study.

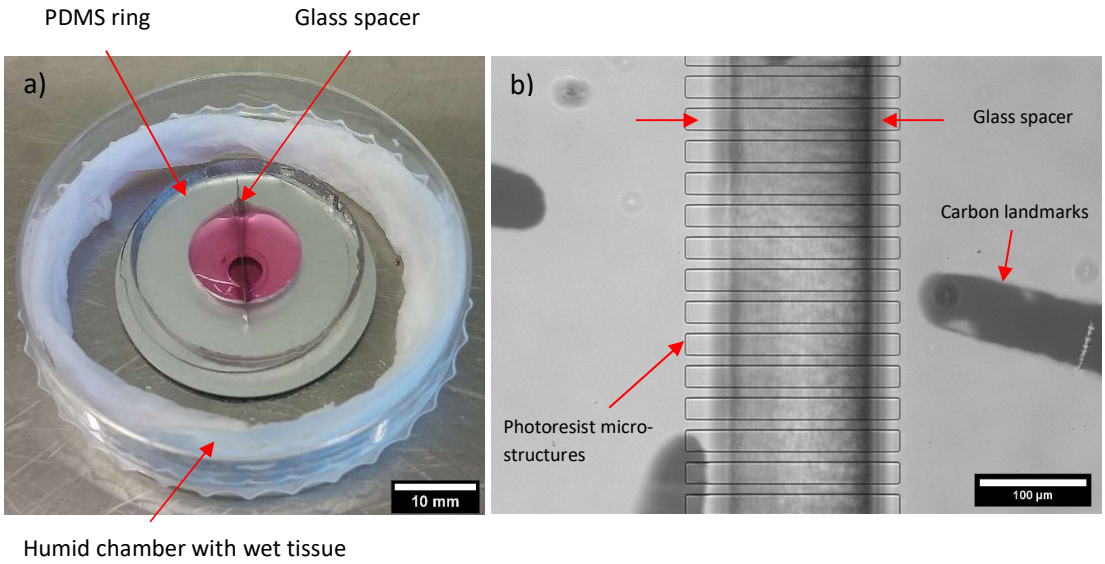

Figure 3.8: Pictures of an assembled PDMS device.

(a) Two groups of cells can be introduced introduced independently into chambers. The device is placed into a home-made humidity chamber with a wet tissue to maintain humidity. (b) Image of the patterned sapphire disc inside the PDMS device recorded using an inverted microscope. The photoresist ridge structure, the glass spacer separating the two chambers as well as the carbon landmarks were clearly visible.

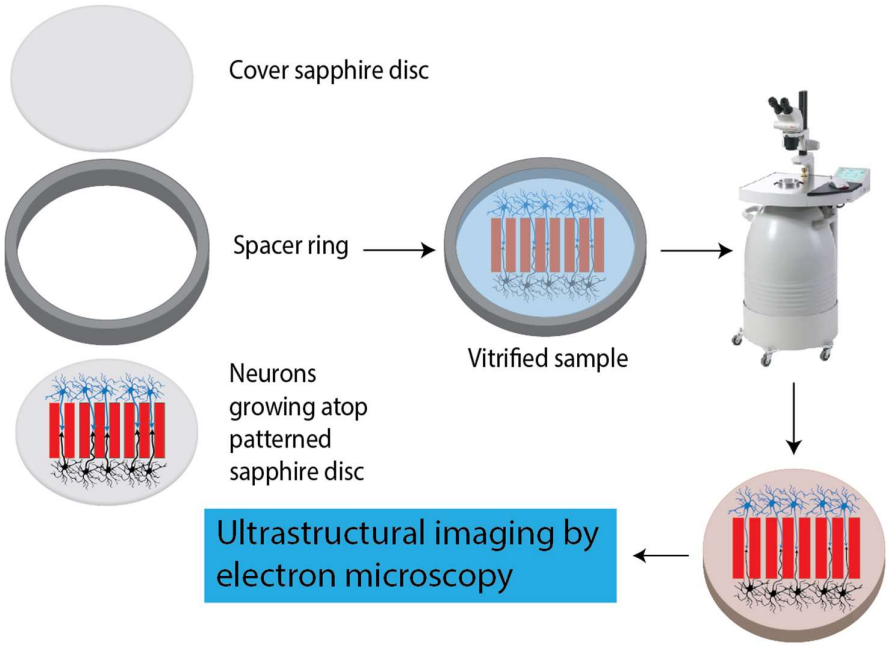

Figure 3.9: Experimental workflow for ultrastructural imaging.

Cryo-fixation of cells grown on the structured discs via high pressure freezing, followed by freeze substitution is utilized to preserve cellular ultra-structures for downstream electron microscope analysis.

3.3.2 Cell culture

3.3.2.1 Culturing PC 12 cells

Rat pheochromocytoma cells PC12 are extensively used as models in neuroscience research as they have the ability to exhibit typical neuronal features. In the presence of nerve growth factor (NGF), they undergo neuronal differentiation to adopt the morphology and functionality of neurons with long extensions[147–149] (**Figure 3.10**). Before plating into the PDMS device, PC12 cells were labeled with EGFP or mCherry using lentivirus infection in order to enable visualization of potential interactions between two isolated sets of cells. This also facilitated the observation of the response of the neuritic projections of PC12 cells into the micropatterns of the sapphire discs. Labelled PC12 cells were plated into the separated chambers of the PDMS devices, which had been coated with collagen type IV to promote cell attachment and differentiation. During 14 days of differentiation with NGF supplement, the cells were periodically characterized by optical microscopy to monitor the outgrowth of individual neuritic processes. The design of device permits the direct observation of living cells on the sapphire discs inside chambers without the need of disassembling the device. Clear observation of thin neuritic processes by inverted microscopy demonstrates the compatibility of the PDMS device with live microscopic imaging (**Figure 3.11**). For more detailed analysis of the outgrowth of projections, the patterned sapphire discs were then removed from PDMS and imaged in a high-resolution microscope. The optical images in **Figure 3.12** showed that the PC12 cells were differentiated efficiently and displayed long neurites. **Figure 3.12b-c** clearly demonstrates that the microstructures performed well in directing the neural outgrowth, as multiple neurites were observed to follow patterns and grew in directions outward from each of the two compartments along the ridges.

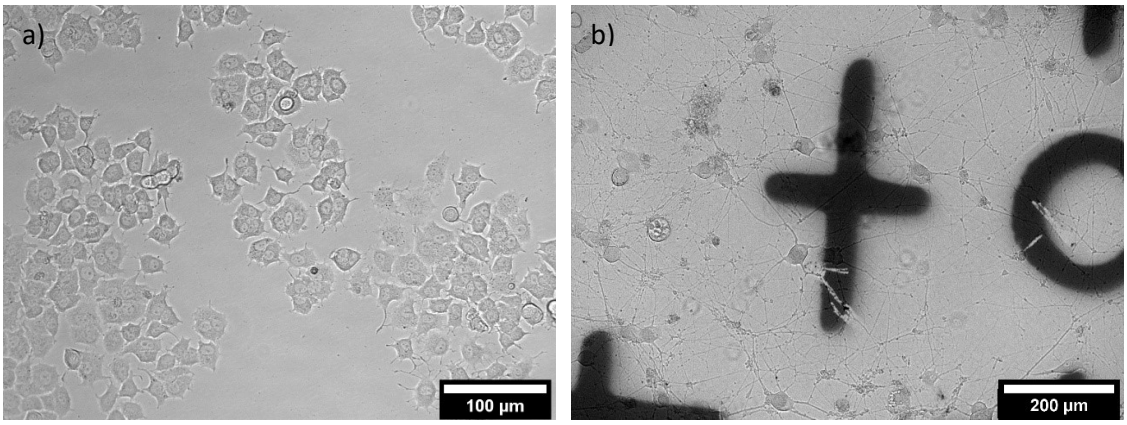

Figure 3.10: Differentiation of PC12 cells on collagen coated sapphire disc.

(a) Undifferentiated PC12 cells growing on collagen type IV sapphire disc. (b) 14 DIV differentiated PC12 cells growing on collagen type IV sapphire discs in the presence of nerve growth factor (NGF).

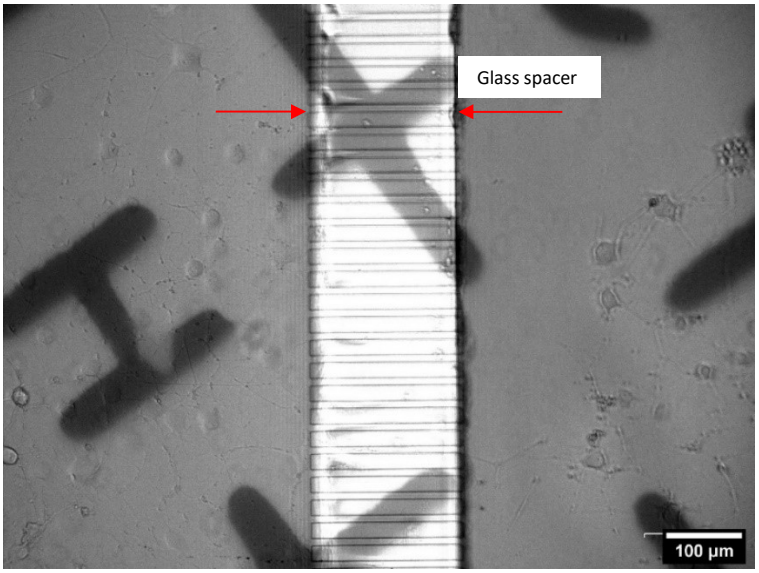

Figure 3.11: Live imaging of 5 DIV differentiated PC12 growing on a structured and collagen coated sapphire disc inside PDMS chamber.

5 DIV differentiated PC12 cells growing on patterned sapphire disc with long extensions. The glass spacer which was aligned to cover microstructures is visible.

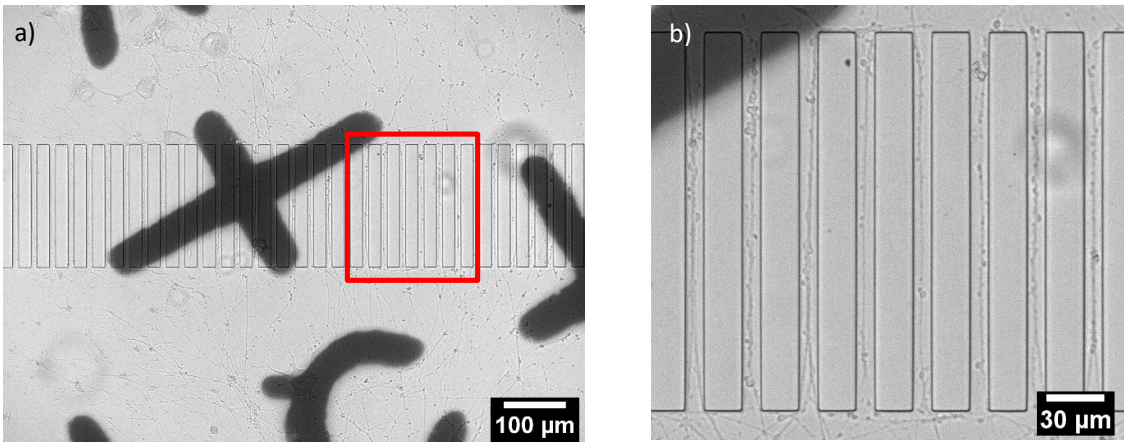

Figure 3.12: Live imaging of differentiated PC12 cells growing on a structured sapphire disc coated with collagen type IV.

(a) Projections from differentiated PC12 cells were guided to grow into channels between ridges. (b) Zoomed-in red box in (a).

3.3.2.2 Culturing of postnatal hippocampal neurons

Hippocampal neurons were dissociated from postnatal mice hippocampi. Two groups of dissociated neurons were incubated with lentivirus to fluorescently label them with either EGFP or mCherry prior to cell seeding. Those labeled groups of neurons were introduced into separated areas on the patterned sapphire discs in the PDMS devices. Hippocampal neurons exhibited good viability at 21 DIV, confirming the biocompatibility of the SU-8 photoresist with primary neuron cultures. The viability of neurons and the outgrowth of neurites on the patterned sapphire discs were observed using an inverted microscope (**Figure 3.13**). As shown in **Figure 3.14**, the intact neuronal networks with fine extending neurites are imaged at higher resolution by confocal microscopy after disassembling them to investigate neurites in the microchannels. Labelled neurons that were expressing EGFP or mCherry grew inside the separated compartments on the patterned sapphire disc. The majority of neurons in one chamber

expressed mCherry whereas neurons in the other one expressed EGFP. The compartment-specific expression of either EGFP or mCherry demonstrated the ability of our device to introduce and maintain independent culturing of two sets of different cells in components separated by the patterned microstructures on the patterned sapphire discs, and to permit the investigation of the interactions between the two cell populations. It was observed that neuritic processes extending from neuronal cell bodies followed along the micropatterned channels (**Figure 3.14**). The fluorescent signals facilitated the visualization of neuritic outgrowth into these channels. Red or green neurites extending from either mCherry- or EGFP-labeled neurons, respectively, were evident within the microchannels, and neurites that contacted the inner walls of the micropatterned channels continued to grow parallel along the length of that wall towards the neighboring compartment, rather than climb upwards and over the ridges. It is likely that the limited flexibility of microtubules and actin filaments hindered the significant bending of growth cones' filopodia to change to a more perpendicular direction of outgrowth[150,151]. In addition, the adhesion of the filopodia onto the substrate at the step might be higher than on a flat surface due to higher contacting area. Therefore, the neurites prefer to keep growing at the edge of the ridges.

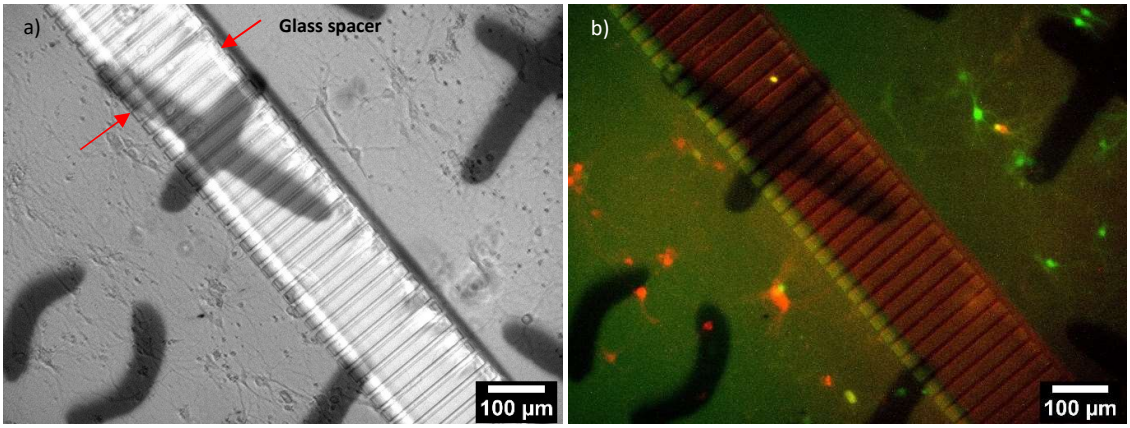

Figure 3.13: Live imaging of 14 DIV postnatal hippocampal neurons growing on a structured and Poly-L-Lysine coated sapphire disc inside PDMS chamber.

(a) 14 DIV neurons growing on patterned sapphire disc with extended neurites. The glass spacer which was aligned to cover microstructures is visible. (b) Two groups of postnatal hippocampal neurons labeled with m-Cherry and EGFP, respectively, which were growing in separated chambers.

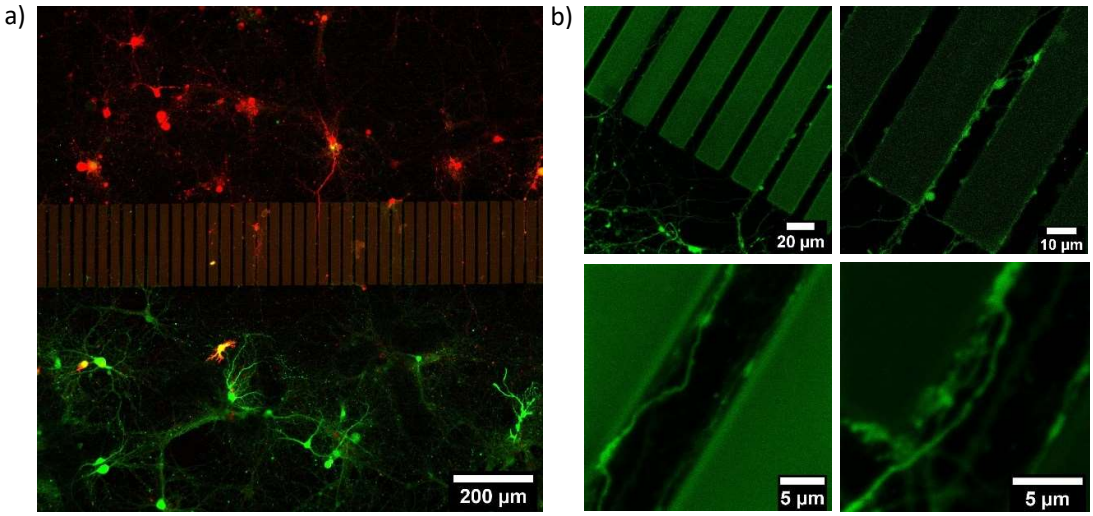

Figure 3.14: Live imaging of 21 DIV postnatal hippocampal neurons growing on a structured and Poly-L-Lysine coated sapphire disc.

(a) Two sets of postnatal hippocampal neurons labeled with m-Cherry and EGFP, respectively, which were growing in separated chambers. (b) Representative images of the neurites, which were growing in channels.

3.3.2.3 Culturing of embryonic striatal neurons

Embryonic (E18) striatal neurons were obtained from E18 rat striatum and DARPP32+ neurons were identified using a specific antibody[152] (**Figure 3.15**). Dissociated neurons were cultured on Poly-L-Lysine coated patterned sapphire discs with optimized density (160 cells/mm^2) and observed by live imaging using an optical microscope at 14-DIV DIV to localize regions of interest immediately prior to the cryo-fixation process by high-pressure freezing, to prepare such samples for downstream electron microscopy. Neurons demonstrated good viability and the neurites from different neurons were observed to successfully enter the microchannels between ridges from both directions (**Figure 3.16a**). The individual channels, in which neurites from opposite sides of microchannels established the contacts, were targeted for downstream

analysis. The landmarks produced from evaporated carbon were stable and clearly visible after 14 days in culture. They were used to precisely identify regions of interest by optical microscopy for subsequent processing. Furthermore, we found that resist microstructures provided sufficient geometrical guidance cues to direct neuritic outgrowth from the striatal neurons into the predefined patterns. None of the observed neurites crossed over the ridges of the microchannels. This was confirmed in another set of experiments performed by Scanning Electron Microscopy (SEM), which enabled imaging the neuronal networks at higher resolution than optical microscopy. In this case, the striatal neurons growing on the structured sapphire discs were chemically fixed, followed by dehydration by a series of ethanol concentrations in distilled water, drying in a critical point drier and Au coating for SEM imaging. SEM images in **Figure 3.16b** clearly showed that the neuritic extensions from the neurons grew only within the channels. No visible neurites appeared crossing over, or on top, of the ridges of the microchannels. This finding is consistent with previous reports that the ridges of structures with heights over 3 µm was sufficient to prevent neurite overcrossing[143].

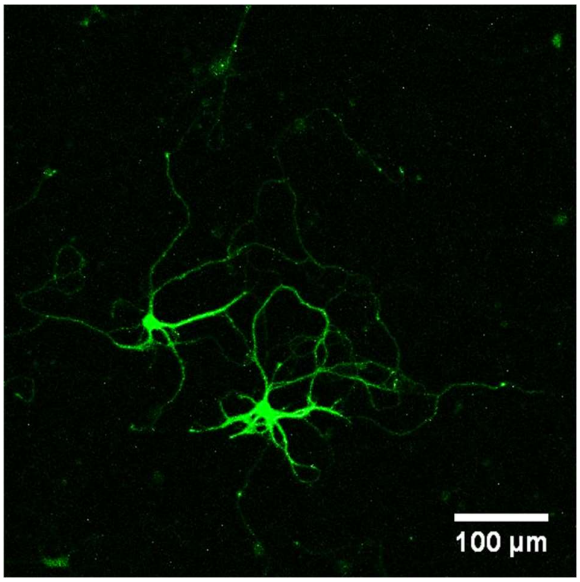

Figure 3.15: 15 DIV striatal neurons growing on glass coverslips.

Striatal neurons were stained with Anti-DARPP32 antibody and visualized by Alexa Fluor 488 secondary antibody.

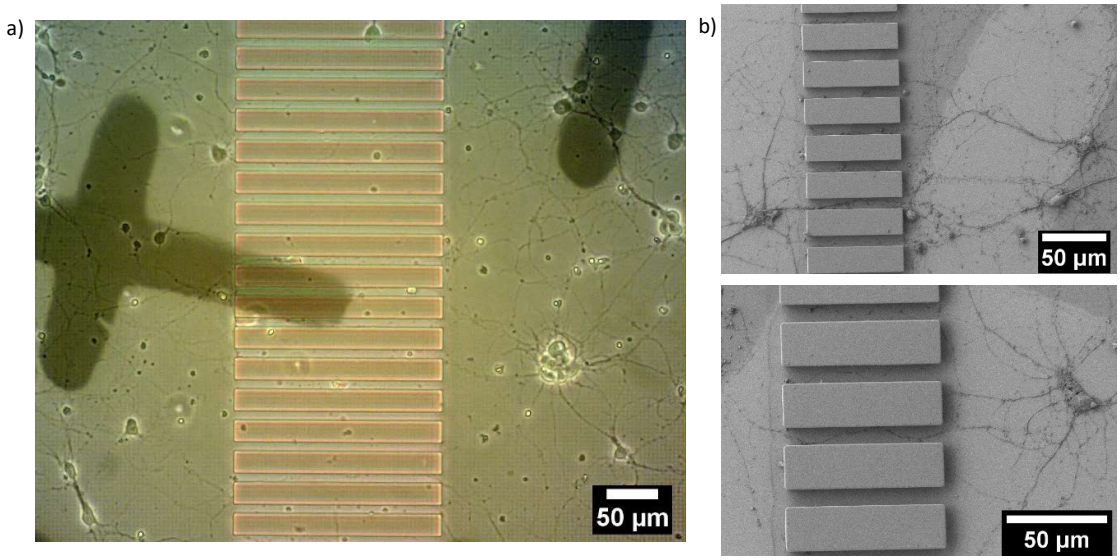

Figure 3.16: 14 DIV embryonic striatal neurons which were growing on Poly-L-Lysine coated-patterned sapphire disc.

(a) Live imaging showed neurites from neurons on both sides of the structure growing into channels. (b) SEM images of the neurites, which were growing into channels. Crossing of neurites over the ridge structures was not observed in any sample.

3.3.3 Ultrastructural imaging

3.3.3.1 Focus Ion Beam – Scanning Electron Microscopy (FIB-SEM)

After cryo-fixation via high pressure freezing, 14 DIV E18 striatal neurons were subjected to a freeze substitution process using a substitution solution consisting of a cocktail of heavy metals for staining (to enhance contrast for electron microscopy) followed by resin embedding (for details see *Methods*). The resin blocks were then processed by Focused Ion Beam – Scanning Electron Microscopy (FIB-SEM) to investigate the ultrastructure of the embedded neuronal networks. FIB-SEM is a commonly used method for 3D biological imaging developed in the last decade [153–155]. Typically, the 3D FIB-SEM procedure utilizes a focused ion beam to sequentially remove thin layers (a few nanometers thick) of either frozen-hydrated or resin-embedded samples to expose a fresh surface for subsequent imaging by SEM. This enables the 3D reconstruction of samples with nanoscale resolution, albeit relatively less than that afforded by transmission electron microscopy (TEM).

As there is very little contrast between photoresist structures and the embedding resin, the parallel-ridge structures of the microchannels are not directly visible in the SEM. However, following freeze substitution and resin embedment, the carbon landmarks were found to be transferred to the resin block and were clearly visible by SEM (**Figure 3.17a**). Furthermore, the patterned regions were recognized easily by observing the neuritic outgrowths into the channels between the ridges (**Figure 3.17b**). Numerous neurites originated from opposite sides of the microstructures and were clearly visible within the separating channels. Using the carbon evaporated landmarks, the regions of interest selected earlier by optical microscopy were targeted and processed by FIB, to reveal the embedded neurites within microchannels. The freshly-milled surface was captured by SEM and the internal ultrastructure of multiple neurites within the channels were clearly revealed (**Figure 3.17c**). The neurites were optimally embedded within the resin block and located very proximally to the surface (within 70nm ~ 300nm). The SEM images also showed various neurites entering a single channel and establishing close physical contacts. The excellent resolution provided by FIB-SEM is well suited to study the ultrastructure of such embedded neuronal networks. However, the process time is a limiting factor, as it takes approximately 1-2 weeks to investigate a single 200 µm-long channel. Therefore, such a method appears more suitable to obtain high-resolution images for pre-

targeted regions, rather than scanning or “fishing” generally for synaptic connections within a long channel, for example.

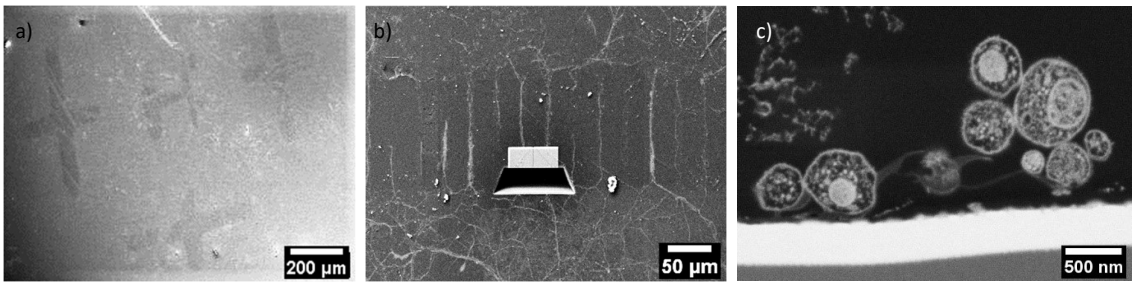

Figure 3.17: Ultrastructural analysis of resin-embedded embryonic striatal neurons by FIB-SEM.

(a) SEM images of the surface of resin block. The carbon finder grid was transferred to the resin and it was clearly detectable by SEM. (b) The neurites in the channels were targeted and processed by FIB-SEM. (c) Cross-section of neurites in a channel laid open by FIB and imaged by SEM.

3.3.3.2 Serial sectioning - Transmission Electron Microscopy (TEM)

The carbon landmarks, embedded microstructures and neuronal networks in resin blocks were clearly visible by optical microscope to allow regions of interest selection for physical sectioning by a diamond knife using an ultramicrotome to prepare ultrathin sections (50-60 nm thickness) for TEM imaging (**Figure 3.18**). The channels between the patterned ridges were targeted for processing to reveal the ultrastructure of neurites within. Compared to FIB, such ultramicrotome sectioning using a physical diamond knife enabled cutting along the length of microstructures and a large area could be captured in a single section. Thus, substantially larger imaging areas were possible to obtain, allowing us to visualize and track neurites within the channels with relatively less processing time. However, it was challenging to capture the neurites in these ultrathin sections because those were accumulated very near to the surface of the resin block.

Standard slot-type electron microscopy grids were used to collect the ultrathin sections to ultimately enable a larger viewing window by TEM imaging. Numerous neurites were observed within a single channel (**Figure 3.19a**). TEM images revealed a perfectly-preserved ul-

trastructure of the embedded neurites with high contrast. Colored boxes in **Figure 3.19a** represent areas that are zoomed-in to show a higher magnification in **Figure 3.19b-e**. At this magnification, internal cellular structures including microtubules, synaptic vesicles, and mitochondria are clearly visible. Axonal terminals are also recognizable based on their button-like shape (white asterix in **Figure 3.19c-e**). Multiple physical contacts between neurites were observed to be established in the channel area. However, no ultrastructural evidence of a synapse was observed in this particular channel.

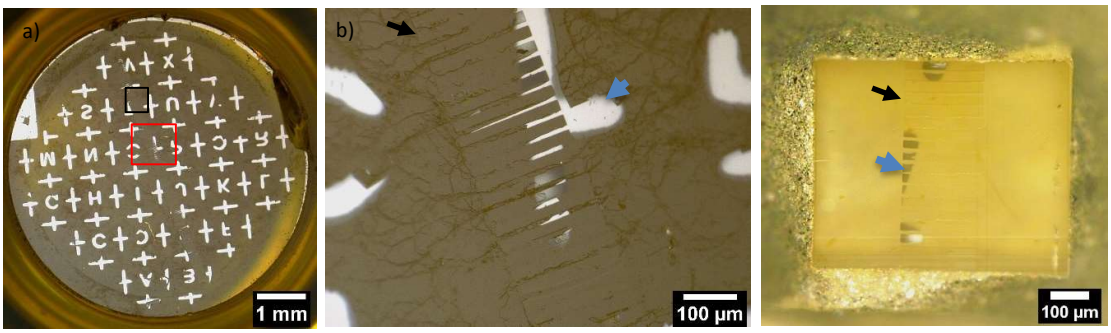

Figure 3.18: Light microscope of embedded neuronal networks in Epon resin block.

(a) Overview of resin block; (b) Zoomed-in red box in (a); (c) Region of interest in black box in (a) was selected and trimmed by razor and ultramicrotome. Black arrows: photoresist microstructures. Blue arrows: carbon landmarks.

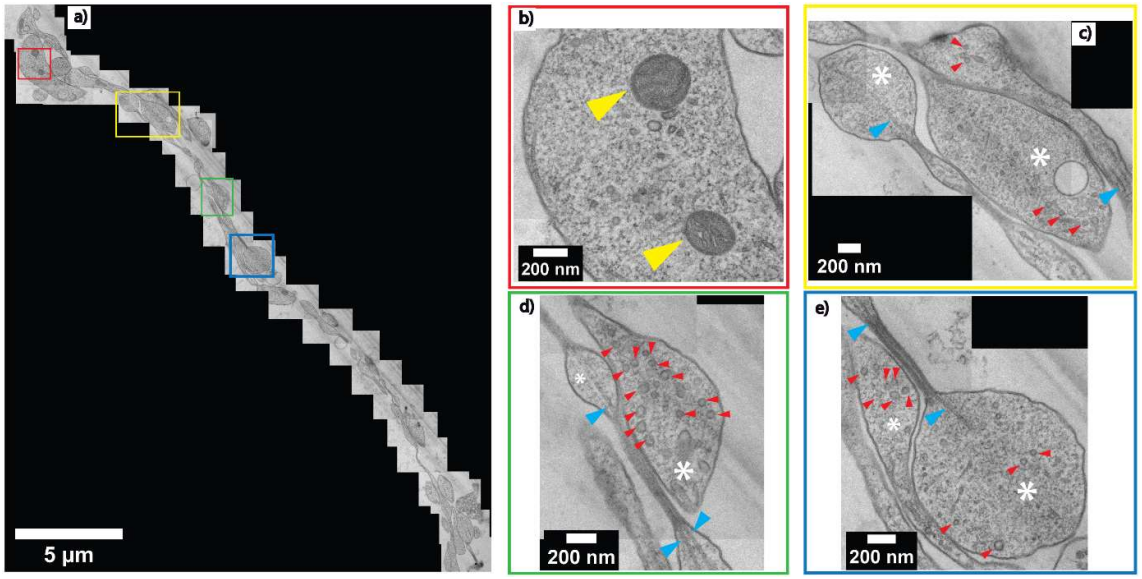

Figure 3.19: Ultrastructural analysis of resin-embedded embryonic striatal neuron obtained by serial sectioning – TEM.

(a) A set of TEM micrographs of neurites embedded in a single channel. (b-e) Enlarged images of boxes outlined in (a) with corresponding colors. (yellow arrowhead) = mitochondria, (white asterix) = axonal bouton, (red arrowhead) = synaptic vesicle, (blue arrowhead) = microtubule.

3.4 Discussion

Here we describe a compartmentalized platform enabling ultrastructural imaging of neuronal co-cultures, akin to those separated by channels in microfluidic devices to recreate neuronal pathways and circuits. We demonstrate topographical structuring of sapphire discs as a successful strategy to control cellular adhesion and growth. The fabrication of micropatterned channels atop the sapphire discs by an adapted photolithography process enables the selective guidance of neurites to the adjacent compartment housing compartmentally distinct neurons, all of which can be cryogenically-fixed in a near-physiological state in vitreous ice to preserve their structure for ultrastructural studies, while avoiding the use of chemical fixatives and dehydration. We have shown that a variety of neuronal-type cells can be grown and imaged successfully using our platform: differentiated PC12 cells and both murine hippocampal neurons and striatal neurons. Our results set a solid foundation for next steps in terms of culturing two distinct neuronal populations for re-creating more complex neuronal pathways/circuits, such as the corticostriatal and nigrostriatal pathway. For example, one compartment can be used for culturing cortical cells, and the other compartment can be used for culturing striatal cells. We have successfully demonstrated using our EGFP/mCherry studies that the two distinct neuronal populations do not cross over the channel barrier, and only make contact via their extending neurites through the micropatterned channels. This should open the door to more physiologically relevant discoveries at the nanoscale level using such cryo-fixed, vitrified neuronal networks for high-fidelity electron microscopy.

Since photolithography is a well-established patterning method that enables large-scale mass production and high reproducibility, the current fabrication process could be feasibly scaled up by means of designing a sample holder to allow parallel processing of multiple samples at the same time. In future developments it would be useful to enhance the resolution of the microstructures for reconstruction of neuronal networks. For instance, smaller microchannels (2-3 µm) are more effective in completely preventing the migration of the neurons themselves into the channels, as well as limiting the number of neurites entering the channels. This enables more clear and distinct tracing of individual neurites to their respective neuron as well as the synaptic contacts downstream. More elaborate microstructures with higher resolution could be utilized for creating unidirectional patterns for the investigation of predefined

neuronal connectivity [116–119] or the addition of extra chambers for local manipulation of neuronal circuits [32,113]. Such advanced devices can bridge the gap between compartmentalized microfluidic platforms and high fidelity ultrastructural imaging of cryogenically fixed, vitrified neuronal specimens. Since the resolution of fabricated microstructures on sapphire discs is mainly limited by the incompatibility of small samples with the standard photolithography processes, other new procedures can be used to overcome this barrier. Specifically, resolution can be increased using recent advanced mask-less lithography techniques, which allow exposing the patterns directly onto the resist-covered surfaces and can enable the fabrication of 2-D or 3-D microstructures with high resolution on small substrates [156–158].

An important feature of these developed devices is their compatibility with optical microscopy as well as downstream electron microscopy, thereby enabling the correlative study of neuronal networks. By optical microscopy, it is possible to monitor the live imaging of growing cells on top of patterned sapphire discs and the outgrowth of neuronal processes into the microchannels while the sapphire discs are still retained within the PDMS chambers. The neurites present in the microchannels can be live-imaged distinguishably via the expression of distinct fluorescent proteins, for example (**Figure 3.14b**). As a result, distinctly labelled neurites originating from different groups of cells can be traced and analyzed to study specific cell-cell communications as well as their responses to topological cues. The information obtained from optical microscopy can be precisely correlated to the electron micrographs of the same structures for interpretation of dynamic events and their ultrastructure at the nanoscale.

We have cultured multiple neuronal cell lines, including primary striatal and hippocampal neurons successfully on the platform for up to 3 weeks. All cell lines exhibit similar viability as in control experiments on culture dishes, confirming the biocompatibility of our platform for neuronal cell cultures. We also demonstrated the ability of microstructures in guiding the distal projections from separately growing groups of neuronal cells to form physical contacts (**Figure 3.12, 3.14, 3.16**). Although we have not proven the formation of synapses between the neurons, we have shown that neurites make physical contact as shown in **Figures 3.12, 3.17, 3.19** supporting the idea that such microstructures can be applied to image synapses. Given the versatility of the device, future works will undoubtedly include neurons from different brain regions cultured in the distinct compartments of our device, in order to study

physiologically-relevant neuronal circuits to neurodevelopment and neurodegeneration, for example. Moreover, each neuronal population could be independently manipulated using pharmacological chemicals within its distinct compartment to develop disease progression models for brain disease, which often selectively impair certain neurons and affected specific neuronal circuits. For example, the neurotoxin 1-methyl-4-phenylpyridinium (MPP+), the active metabolite of 1-methyl-4-phenyl-1,2,3,6-tetrahydropyridine, can be applied to one of the two compartments of neurons to induce neuronal death as relevant to Parkinson's disease, for correlative biochemical and ultrastructural studies regarding the degeneration of nigrostriatal dopaminergic neurons [159–161]. Furthermore, the responses of neuronal cells to pharmacological agents, such as neuroprotective agents, in the context of disease models can also be investigated at the ultrastructural level in a near-native state to validate their potentials in brain diseases' treatment [161,161–163].

Following cryo-fixation in a vitreous, near native state via high pressure freezing and freeze substitution, the subsequent resin-embedded neuronal networks are compatible with multiple methods to study ultrastructure by electron microscopy. FIB-SEM and serial sectioning-TEM were applied successfully to image the well-preserved ultrastructure of neuronal networks at high resolution (**Figure 3.17, 3.19**). For future studies, the ultrathin sections prepared by serial ultramicrotome sectioning can be combined with immunolabeling to allow the localization of macromolecules at high resolution in the cellular context [164–166]. Theoretically, another approach known as serial block-face scanning electron microscopy (SBF-SEM) would enable the imaging and investigation of neurites inside the microchannels with a relatively larger field of view as compared to FIB-SEM. Thus, it would allow for a more efficient, wide-field view of imaging and investigation of neurites that grow inside the microchannels. However, the large ratio of nonconductive embedding resin of our samples caused charging problems during our attempt at SBF-SEM imaging. Future work that utilizes a more conductive resin during the freeze-substitution process would theoretically eliminate such charging artifacts that we had encountered, thereby improving the imaging by SBF-SEM [167–170]. Furthermore, our system could be extended to different types of sample carriers for high-pressure freezing, which would directly be compatible for cryo-ultramicrotomy and cryo-electron microscopy and tomography, either by cryo-FIB-SEM or cryo-TEM.

3.5 Conclusion

Our cell culture platform with distinct compartments connected by microchannels akin to microfluidics, is uniquely compatible for high-pressure freezing for chemical-free preservation in a near-native vitreous state. It can thereby enable the recapitulation and imaging of neuronal pathways and circuits, and opens the door to more physiologically-relevant nanoscale imaging, and cryo-electron microscopy and tomography of compartmentalized neuronal “microfluidic”-type cultures, which was previously unachievable due to technical constraints that we have overcome. Our device can be expanded to studying neuronal systems in the context of disease and drug testing for correlative studies and high-resolution imaging, thereby serving as a tool of great potential to neuroscience research.

Chapter 4 General conclusion

The two novel imaging techniques described in this thesis can help to shed light into the hierarchical organization of brain samples from the macroscopic level all the way down to the nanoscopic level. The first biological case study by cryo-PXCT in reported here will help to further establish and expand the use of this technique in the biological research community. This study clearly revealed that cryo-PXCT can resolve small details over large spans of tissue, in particular non-destructively in the frozen-hydrated state, and allows further imaging post to the X-ray measurement by other techniques. For the first time the possibility of downstream electron microscopy and immunogold labelling of post cryo-PXCT biological samples was demonstrated whereby the subcellular ultrastructures and antigenicity were well-preserved. High-pressure frozen tissue biopsies at their native, hydrated state could be also investigated by cryo-PXCT using the same experimental setup. It is expected that the ultrastructure as well as protein antigenicity of the high-pressure frozen tissue are even better preseved without chemical fixation and cryo-protectant infiltration and allow for better biochemical investigation by enhanced efficiency and selectivity immunostaning.

The spatial resolution obtained by cryo-PXCT was sufficient to recognize distinct abnormalities in myelinated axons that occur only in PD human brain. The finding of aggregations and swellings in this case study suggests further investigations into fundamental mechanisms, to elucidate the important role which oligodendrocytes play not only for PD but also for other neurodegenerative diseases.

Future work can improve the process towards a better correlation between X-ray imaging by cryo-PXCT and downstream electron microscopy, which is lacked in this work due to the challenges in the cryo-ultramicrotome preparation of serial ultrathin sections from the tissue block after X-ray imaging.

High-pressure frozen tissue biopsies post cryo-PXCT could also be freeze-substitutedfor downstream processing by ultramicrotome at room temperature. Despite the fact that the cryo-workflow to process samples directly at cryo-conditions allows better preservation of ultrastructures and of the protein antigenicity for immunolabelling, the ultramicrotomy of resin-

embedded samples at room temperature is more simple and efficient. Resin-embedded samples can be processed by automated tape-collecting ultramicrotome (ATUM)[171] to prepare serial ultrathin sections from the X-ray imaged tissue blocks (**Figure 4.1)**. Theoretically, this technique can generate up to 10.000 ultrathin sections over 24 h period with no human interaction[171], meaning that whole resin-embedded blocks can be processed for downstream electron microscopy with minimal errors. The serial ultrathin sections can be imaged by SEM and images are assembled by automatic software into a 3D map of the tissue volume in which high resolution imaging targets can be selected[171]. As a result, two complete 3-D tomograms of the tissues at different resolution by different methods (cryo-PXCT and serial sectioning/SEM) and at different states (cryo-preserved, hydrated sample and freeze-substituted, resin embedded sample) can be obtained and fully correlated. The precise correlation of images of the same structure, for instance of dystrophic myelinated axons, allows better understanding of pathological features at ultrastructure level and evaluating the effects of each technique to the ultrastructure of biological samples.

It is also possible to interrupt the automatic collection process to manually pick up a few ultrathin sections by TEM grids and then continue the process. Those ultrathin sections attached on top of TEM grids could be combined with immunogold labelling for biochemical investigation of interesting structures within tissues at higher resolution by TEM. As a result, a comprehensive pipeline from 3D imaging of native tissues to complete correlative electron microscopy combined with biochemical investigation at multiscale can be a powerful tool for neuroscience research, especially for investigation of pathological features of neuronal diseases.

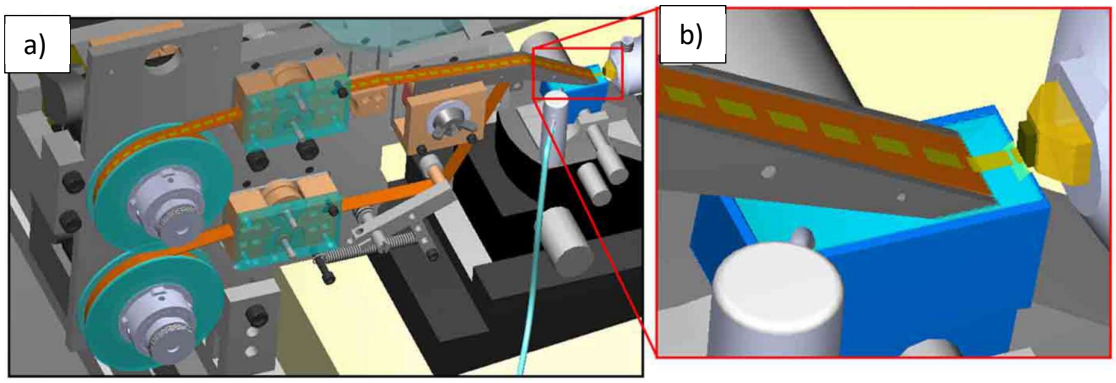

Figure 4.1: An automated tape-collecting ultramicrotome system.

(a) Schematic representation of a tape collection device installed on a commercial ultramicrotome. (b) Zoomed-in red box in (a) showing the collection process of ultrathin sections floating on the knife's water boat onto a surface of partially submerged plastic tape attached on a conveyor belt. Scheme reprinted from *Hayworth (2014)*[171].

While currently the imaging rate of cryo-PXCT is comparable to destructive methods, a dramatic (orders of magnitude) increase in resolution can be expected with upgrades of synchrotron sources currently on the way worldwide. It is expected that the coherent beam with increased flux allows 3D imaging of larger volume samples or at higher resolution. However, this will also increase the radiation damage to the biological samples; therefore more experiments must be carried to find the optimal condition. Recent upgrades in the computational algorithm to reconstruct 3D tomograms from collected overlapping diffractive patterns by cryo-PXCT to significantly reduce the data processing time. This upgrade will allow taking the technique beyond the level of a case study, allowing the measurement of significantly more samples to better understand the diseases' pathologies. Those achievements should thus raise interest from biologists of a wider field to apply this technique to their specific research questions.

Although the 3D tomograms obtained by cryo-PXCT can be semi-automatically segmented to visualize and investigate key features in human brain tissues with high accuracy as demonstrated in this work, the process is very time consuming. It can take several months to complete segmentation process of one single 3D tomogram containing more than a thousand of slices. Since the contrast of tomograms is low due to the low intrinsic density contrast of brain samples, it is challenging to speed up the process by automatic segmentation via automatic

thresholding/masking functions of current image processing software. Lately, the development of artificial intelligence, such as machine learning and artificial neural systems contributes to almost every field of technology, including imaging process[172,173]. Machine learning is defined as "Giving computers the ability to learn without being explicitly programmed" by Arthur Samuel, a pioneer American computer scientist in this field. It is possible to train computer by using complex algorithmic mathematicals to analyze and interpret data sets for image segmentation[174–177]. In this way, the analysis of large data sets from 3D imaging can be significantly improved, in terms of speed, efficiency and accuracy. This can free researchers in this field from repeated, time consuming tasks of image processing and it will grow in influence in the future. In the second part of this work, a well-designed compartmentalized platform for neuronal co-culture was developed to create simplified neuronal networks for studying human brain development and disease. This platform is fully compatible with cryogenic fixation by high pressure freezing, meaning that reconstructed neuronal circuits are cryo-fixed in a vitreous, near-native state for ultrastructural imaging by EM.

With rapid technology development, new possibilities can be expected for the fabrication of more advanced microstructures to reconstruct complex neuronal networks on such small substrates, while still being compatible with ultrastructural imaging. For instance, an additional chamber for a glia cell culture could be integrated to this compartmentalized platform to provide glial support for axon functions and integrity, which is an important feature in native nervous systems. Moreover, it is also important to fabricate a 3D cell culture models for neuroscience research because the 2D reconstructed neuronal networks are very different to their native 3D structure. Neurons in the brain form very dense architectures and tightly linked networks together with other supporting cells (glia cells). Several approaches to form 3D culture models have also been developed. Microwells arrays have been fabricated to create micro-3D (µ3D) neuron cultures to evaluate the activity patterns[178] or to investigate the formation and differentiation of embryoid body (EB) from human embryonic stem cells (hESCs)[179], or from murine embryonic stem cells (mESCs)[180]. The 3D cell culture approaches could be further extended to co-culture neurons and glial cells via multi-layer cultures or hydrogels embedding to fabricate complex brain-like tissue models and to promote the formation and stabilization of synapses [181,182]. The glia cell cultures provide supporting functions

to the neuron cultures, such as maintaining homeostasis, vital support, protection for neurons. Glia cells also serve as “glue” in neuronal networks and provide physical support as a scaffold for migrating neurons during neurogenesis. These brain-like tissue models can provide advanced platforms to address some questions in neuroscience under more relevant conditions.

Hypothetically, the approaches proposed above could be directly integrated into our culture model based on sapphire disc substrates. Advanced micro/nanofabrication methods, for example 3D printing or direct laser writing lithography can help to fabricate complex 3D microstructures on such small sapphire discs with higher resolution for cell cultures. Essentially, the complex 3D cell cultures could be imaged directly in 3D view by cryo-PXCT, followed by correlative ultrastructural study by electron microscopy. Nonetheless, the ability to reduce the volume/size of frozen samples on top of sapphire discs for cryo-PXCT imaging remains a challenge because it is difficult to cut sapphire discs physically by ultramicrotome. The fact that the microstructures atop sapphire discs could also be fabricated on other substrates like metal platelets, it enables direct trimming processes by cryo-ultramicrotomy to resize samples for 3D cryo-PXCT imaging. The post X-ray imaging samples can then be performed by both direct cryo-process and freeze-substituted/resin embedded, which are demonstrated in this work. This would be an example of the possibility to combine cryo-PXCT with the compartmentalized neuron co-culture platform as a more advanced approach for neuroscience research.

Nanoscale label-free imaging cryo-PXCT of the tissue samples at their native state provides great insights into pathological features of the diseases. However, investigation of the mechanism underlying the disease condition or observation of early progression of the disease *in vivo* remain a challenge. Theoretically, compartmentalized neuron co-culture platforms allow reconstruction of various neuronal circuits by co-culturing dissociated neurons from specific brain regions. Therefore, the same neuronal circuits in tissue samples which are investigated by cryo-PXCT can be replicated *in vitro* for further investigation. The pathological features investigated in the diseased brain samples can be simulated on neuronal cell culture models by using relevant neurotoxins. For example, the degeneration of nigrostriatal dopaminergic neurons in PD can be induced by applying neurotoxin 1-methyl-4-phenylpyridinium (MPP^+) [159–161] on reconstructed nigrostriatal pathway on the compartmentalized neuron co-culture platform.

In conclusion, the techniques for neuroimaging reported here are innovative methods for investigating structural aspects of the human brain in both healthy and impaired conditions at nanoscale, enabling valuable contribution to neuroscience research.

Supplementary Material

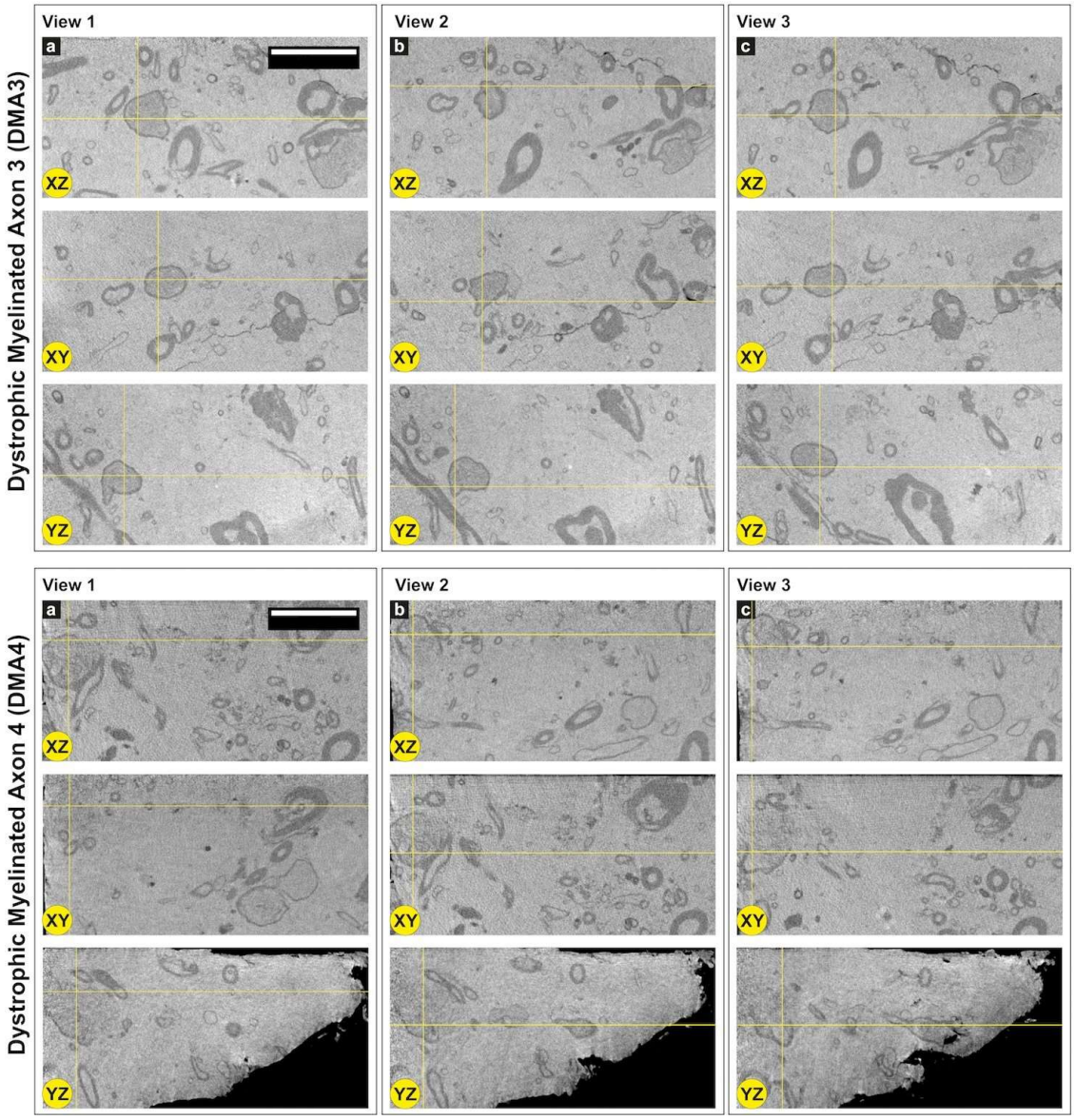

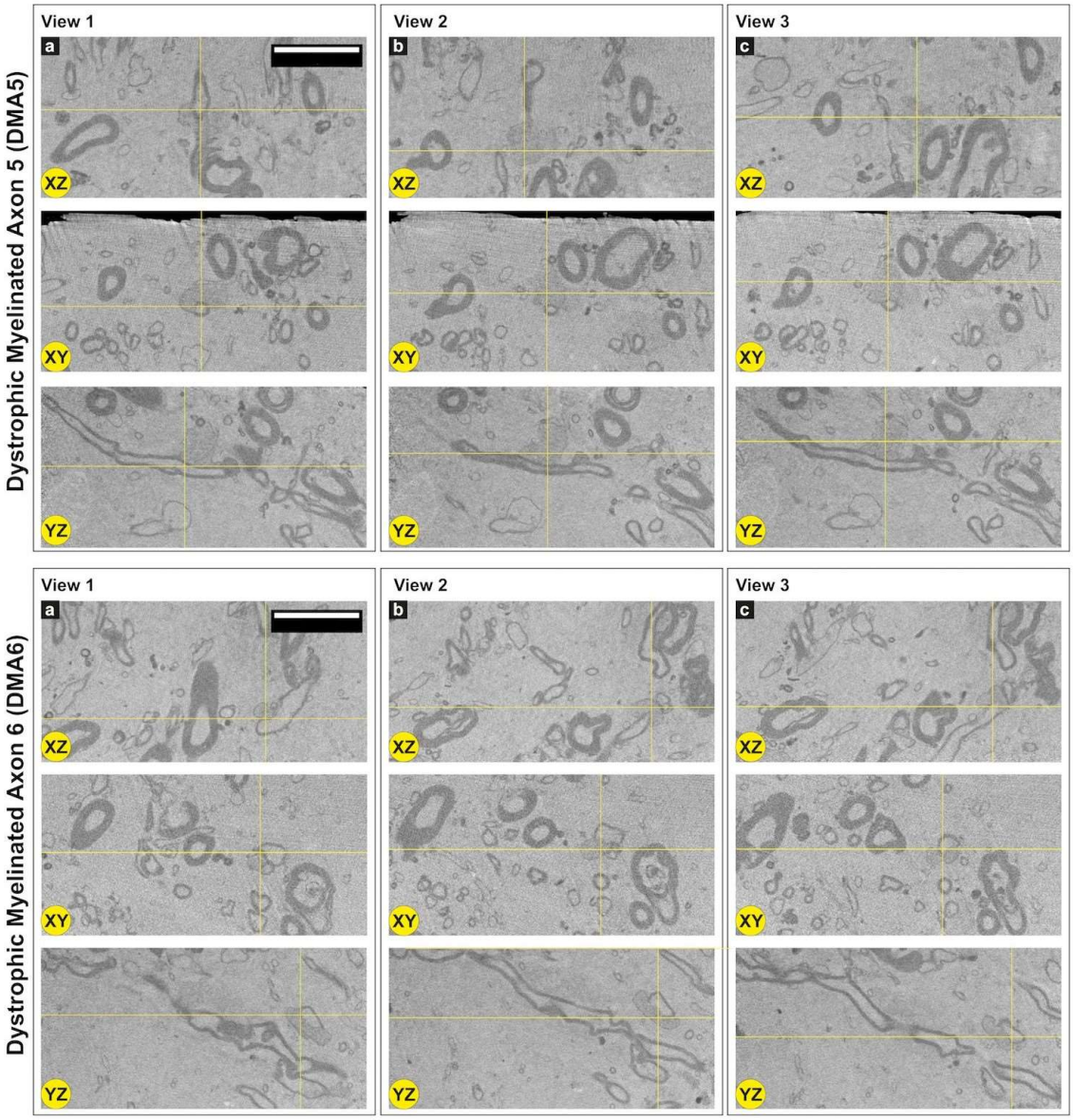
Dystrophic Myelinated Axon 5 (DMA5)
View 1
View 2
View 3
a
b
c
XZ
XY
YZ
Dystrophic Myelinated Axon 6 (DMA6)
View 1
View 2
View 3
a
b
c
XZ
XY
YZ

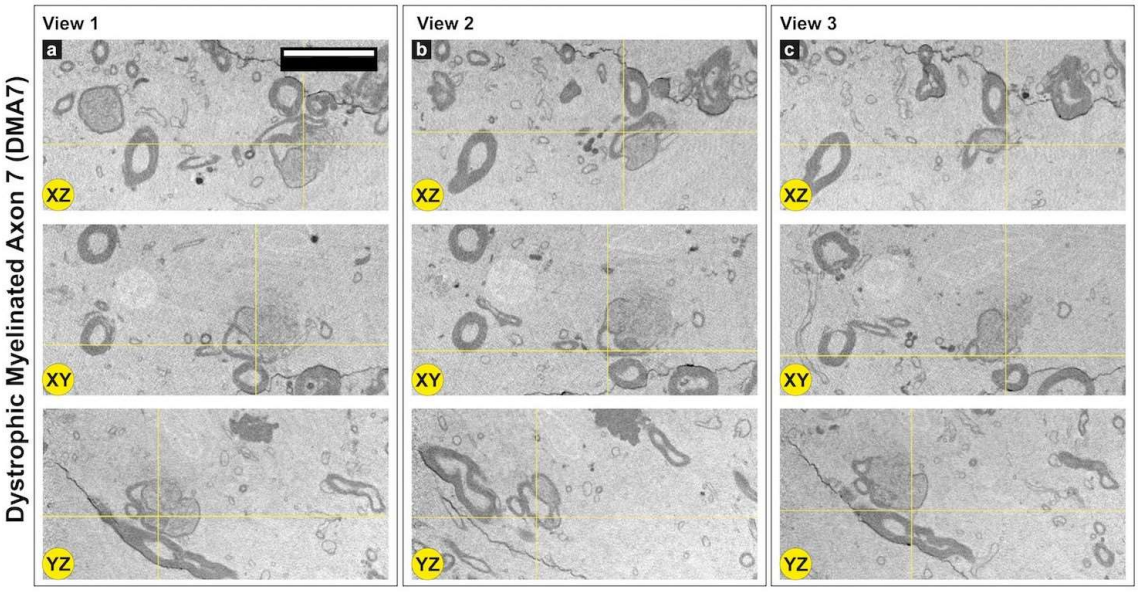

Supplementary Figure 2.1. Dystrophic myelinated axons (DMAs) by cryo-PXCT in Parkinson's diseased human brain. Single 2D orthoslices with inverted grayscale showing the appearance of five DMAs (indicated by the yellow crosses) in different planes (X-Z, X-Y, Y-Z) and different positions (Views 1, 2, 3) in the 3D tomogram. Yellow crosses indicate the position of the DMA in the different views and planes. Other DMAs are shown in **Figures 2.7** and **Supplementary Figure 2.2**. Grayscale shown herein does not correspond directly to mass density as opposed to **Figure 2.3**. Scale bars: 10 µm

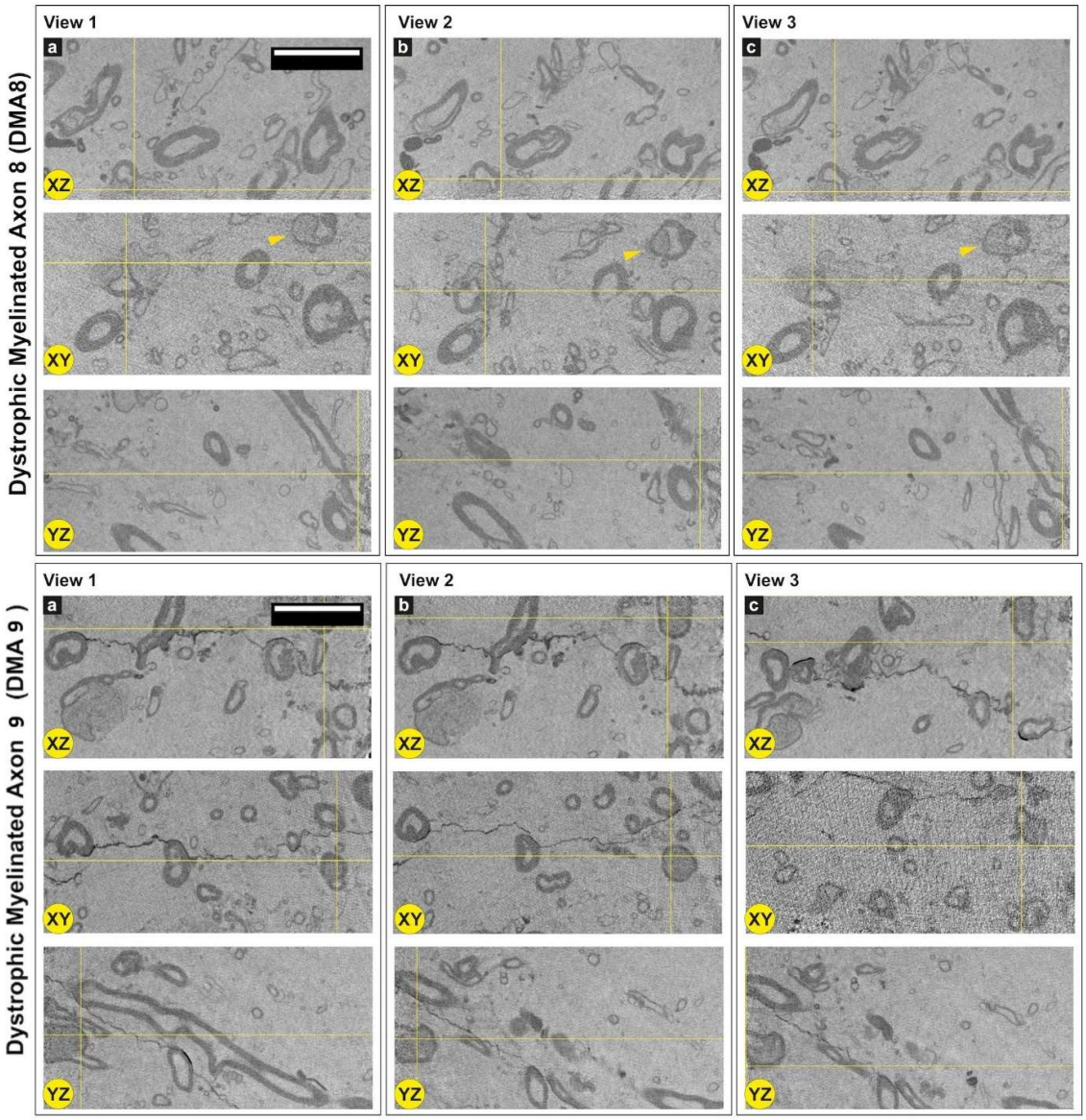
Dystrophic Myelinated Axon 8 (DMA8)
View 1
View 2
View 3
a
b
c
XZ
XY
YZ
Dystrophic Myelinated Axon 9 (DMA 9)
View 1
View 2
View 3
a
b
c
XZ
XY
YZ

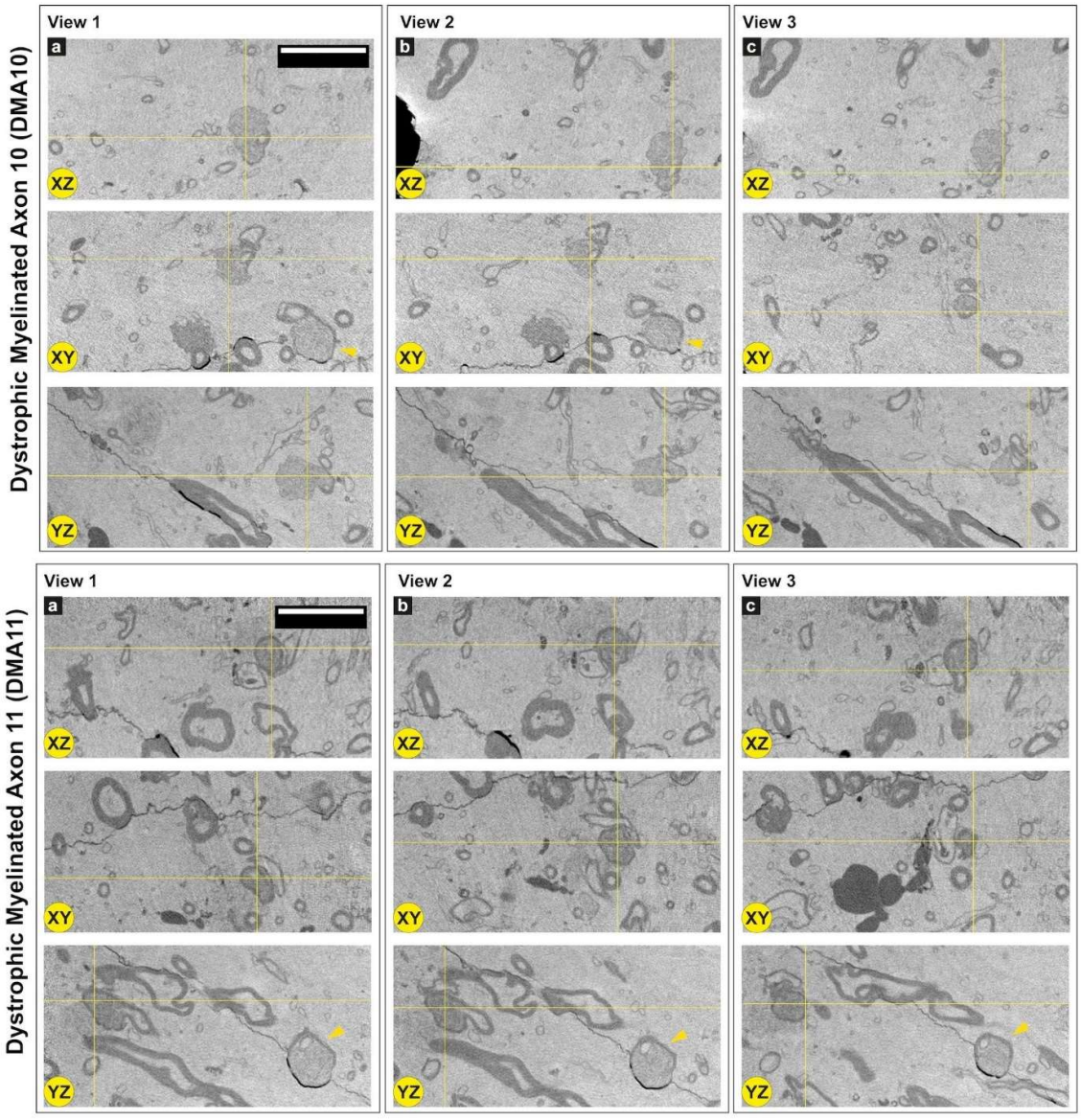

Supplementary Figure 2.2. Dystrophic myelinated axons (DMAs) by cryo-PXCT in Parkinson's diseased human brain. Single 2D orthoslices with inverted grayscale showing the appearance of four DMAs (indicated by the yellow crosses) in different planes (X-Z, X-Y, Y-Z) and different positions (Views 1, 2, 3) in the 3D tomogram. Yellow crosses indicate the position of the DMA in the different views and planes. Yellow arrowheads indicate other DMAs present in the same viewing frame. Other DMAs are shown in **Figures 2.7** and **Supplementary Figure 2.1**. Grayscale shown herein does not correspond directly to mass density as opposed to **Figure 2.3**. Scale bars: 10 µm.

References

1. Herculano-Houzel, S. The remarkable, yet not extraordinary, human brain as a scaled-up primate brain and its associated cost. *Proc. Natl. Acad. Sci.* **109**, 10661–10668 (2012).

2. Park, H.-J. & Friston, K. Structural and Functional Brain Networks: From Connections to Cognition. *Science* **342**, 1238411 (2013).

3. Nave, K.-A. & Werner, H. B. Myelination of the Nervous System: Mechanisms and Functions. *Annu. Rev. Cell Dev. Biol.* **30**, 503–533 (2014).

4. Suter, U. & Martini, R. Chapter 19 - Myelination. in *Peripheral Neuropathy (Fourth Edition)* (eds. Dyck, P. J. & Thomas, P. K.) 411–431 (W.B. Saunders, 2005). doi:10.1016/B978-0-7216-9491-7.50022-3.

5. Meyer, N. *et al.* Oligodendrocytes in the Mouse Corpus Callosum Maintain Axonal Function by Delivery of Glucose. *Cell Rep.* **22**, 2383–2394 (2018).

6. Philips, T. & Rothstein, J. D. Oligodendroglia: metabolic supporters of neurons. *J. Clin. Invest.* **127**, 3271–3280.

7. Funfschilling, U. *et al.* Glycolytic oligodendrocytes maintain myelin and long-term axonal integrity. *Nature* **485**, 517–521 (2012).

8. Morell, P. & Norton, W. T. Myelin. *Sci. Am.* **242**, 88–114 (1980).

9. Menon, V. Large-Scale Functional Brain Organization. in *Brain Mapping* 449–459 (Elsevier, 2015). doi:10.1016/B978-0-12-397025-1.00024-5.

10. Chevalier-Larsen, E. & Holzbaur, E. L. F. Axonal transport and neurodegenerative disease. *Biochim. Biophys. Acta BBA - Mol. Basis Dis.* **1762**, 1094–1108 (2006).

11. Su, J. H., Cummings, B. J. & Cotman, C. W. Identification and distribution of axonal dystrophic neurites in Alzheimer's disease. *Brain Res.* **625**, 228–237 (1993).

12. Adalbert, R. *et al.* Severely dystrophic axons at amyloid plaques remain continuous and connected to viable cell bodies. *Brain* **132**, 402–416 (2009).

13. Inglese, M. & Petracca, M. Imaging multiple sclerosis and other neurodegenerative diseases. *Prion* **7**, 47–54 (2013).

14. Lee, J. Y., Taghian, K. & Petratos, S. Axonal degeneration in multiple sclerosis: can we predict and prevent permanent disability? *Acta Neuropathol. Commun.* **2**, 97 (2014).

15. Friese, M. A. Widespread synaptic loss in multiple sclerosis. *Brain* **139**, 2–4 (2016).

16. Salzer, J. L. & Zalc, B. Myelination. *Curr. Biol.* **26**, R971–R975 (2016).

17. Canter, R. G., Penney, J. & Tsai, L.-H. The road to restoring neural circuits for the treatment of Alzheimer's disease. *Nature* **539**, 187–196 (2016).

18. Busche, M. A. & Konnerth, A. Impairments of neural circuit function in Alzheimer's disease. *Philos. Trans. R. Soc. B Biol. Sci.* **371**, (2016).

19. Zott, B., Busche, M. A., Sperling, R. A. & Konnerth, A. What Happens with the Circuit in Alzheimer's Disease in Mice and Humans? *Annu. Rev. Neurosci.* **41**, 277–297 (2018).

20. Blumenstock, S. & Dudanova, I. Cortical and Striatal Circuits in Huntington's Disease. *Front. Neurosci.* **14**, (2020).

21. Miller, B. R. & Bezprozvanny, I. Corticostriatal circuit dysfunction in Huntington's disease: intersection of glutamate, dopamine and calcium. *Future Neurol.* **5**, 735–756 (2010).

22. Ghiglieri, V. *et al.* Corticostriatal synaptic plasticity alterations in the R6/1 transgenic mouse model of Huntington's disease. *J. Neurosci. Res.* **97**, 1655–1664 (2019).

23. Miller, B. R., Walker, A. G., Barton, S. J. & Rebec, G. V. Dysregulated Neuronal Activity Patterns Implicate Corticostriatal Circuit Dysfunction in Multiple Rodent Models of Huntington's Disease. *Front. Syst. Neurosci.* **5**, (2011).

24. McGregor, M. M. & Nelson, A. B. Circuit Mechanisms of Parkinson's Disease. *Neuron* **101**, 1042–1056 (2019).

25. Kim, J. *et al.* Abnormal intrinsic brain functional network dynamics in Parkinson's disease. *Brain* **140**, 2955–2967 (2017).

26. Caligiore, D. *et al.* Parkinson's disease as a system-level disorder. *NPJ Park. Dis.* **2**, 16025 (2016).

27. Saxena, S. & Caroni, P. Selective Neuronal Vulnerability in Neurodegenerative Diseases: from Stressor Thresholds to Degeneration. *Neuron* **71**, 35–48 (2011).

28. Bamford, N. S. *et al.* Heterosynaptic Dopamine Neurotransmission Selects Sets of Corticostriatal Terminals. *Neuron* **42**, 653–663 (2004).

29. Cepeda, C., Wu, N., André, V. M., Cummings, D. M. & Levine, M. S. The corticostriatal pathway in Huntington's disease. *Prog. Neurobiol.* **81**, 253–271 (2007).

30. Surmeier, D. J., Ding, J., Day, M., Wang, Z. & Shen, W. D1 and D2 dopamine-receptor modulation of striatal glutamatergic signaling in striatal medium spiny neurons. *Trends Neurosci.* **30**, 228–235 (2007).

31. Bolam, J. P. & Pissadaki, E. K. Living on the edge with too many mouths to feed: Why dopamine neurons die. *Mov. Disord.* **27**, 1478–1483 (2012).

32. Taylor, A. M., Dieterich, D. C., Ito, H. T., Kim, S. A. & Schuman, E. M. Microfluidic Local Perfusion Chambers for the Visualization and Manipulation of Synapses. *Neuron* **66**, 57–68 (2010).

33. Tran, H. T. *et al.* Alterations in Sub-Axonal Architecture Between Normal Aging and Parkinson's Diseased Human Brains Using Label-Free Cryogenic X-ray Nanotomography. *Front. Neurosci.* **14**, (2020).

34. Galvin, J. E., Uryu, K., Lee, V. M.-Y. & Trojanowski, J. Q. Axon pathology in Parkinson's disease and Lewy body dementia hippocampus contains α-, β-, and γ-synuclein. *Proc. Natl. Acad. Sci.* **96**, 13450–13455 (1999).

35. Kotzbauer, P. T. *et al.* Fibrillization of α-synuclein and tau in familial Parkinson's disease caused by the A53T α-synuclein mutation. *Exp. Neurol.* **187**, 279–288 (2004).

36. Saha, A. R. Parkinson's disease -synuclein mutations exhibit defective axonal transport in cultured neurons. *J. Cell Sci.* **117**, 1017–1024 (2004).

37. Chung, C. Y., Koprich, J. B., Siddiqi, H. & Isacson, O. Dynamic Changes in Presynaptic and Axonal Transport Proteins Combined with Striatal Neuroinflammation Precede Dopaminergic Neuronal Loss in a Rat Model of AAV -Synucleinopathy. *J. Neurosci.* **29**, 3365–3373 (2009).

38. Burke, R. E. & O'Malley, K. Axon degeneration in Parkinson's disease. *Exp. Neurol.* **246**, 72–83 (2013).

39. Koch, J. C. *et al.* Alpha-Synuclein affects neurite morphology, autophagy, vesicle transport and axonal degeneration in CNS neurons. *Cell Death Dis.* **6**, e1811–e1811 (2015).

40. Sekigawa, A., Takamatsu, Y., Sekiyama, K. & Hashimoto, M. Role of α- and β-Synucleins in the Axonal Pathology of Parkinson's Disease and Related Synucleinopathies. *Biomolecules* **5**, 1000–1011 (2015).

41. Tagliaferro, P. & Burke, R. E. Retrograde Axonal Degeneration in Parkinson Disease. *J. Park. Dis.* **6**, 1–15 (2016).

42. Kouroupi, G. *et al.* Defective synaptic connectivity and axonal neuropathology in a human iPSC-based model of familial Parkinson's disease. *Proc. Natl. Acad. Sci.* **114**, E3679–E3688 (2017).

43. Shahmoradian, S. H. *et al.* Lewy pathology in Parkinson's disease consists of crowded organelles and lipid membranes. *Nat. Neurosci.* **22**, 1099–1109 (2019).

44. Mizutani, R. *et al.* Microtomographic Analysis of Neuronal Circuits of Human Brain. *Cereb. Cortex* **20**, 1739–1748 (2010).

45. Fonseca, M. de C. *et al.* High-resolution synchrotron-based X-ray microtomography as a tool to unveil the three-dimensional neuronal architecture of the brain. *Sci. Rep.* **8**, 12074 (2018).

46. Dyer, E. L. *et al.* Quantifying Mesoscale Neuroanatomy Using X-Ray Microtomography. *eNeuro* **4**, (2017).

47. Khimchenko, A. *et al.* Hard X-Ray Nanoholotomography: Large-Scale, Label-Free, 3D Neuroimaging beyond Optical Limit. *Adv. Sci.* **5**, 1700694 (2018).

48. Le Gros, M. A. *et al.* Soft X-Ray Tomography Reveals Gradual Chromatin Compaction and Reorganization during Neurogenesis In Vivo. *Cell Rep.* **17**, 2125–2136 (2016).

49. Pérez-Berná, A. J. *et al.* Structural Changes In Cells Imaged by Soft X-ray Cryo-Tomography During Hepatitis C Virus Infection. *ACS Nano* **10**, 6597–6611 (2016).

50. Wu, H. R. *et al.* Nanoresolution radiology of neurons. *J. Phys. Appl. Phys.* **45**, 242001 (2012).

51. Mokso, R., Cloetens, P., Maire, E., Ludwig, W. & Buffière, J.-Y. Nanoscale zoom tomography with hard x rays using Kirkpatrick-Baez optics. *Appl. Phys. Lett.* **90**, 144104 (2007).

52. Bartels, M., Krenkel, M., Cloetens, P., Möbius, W. & Salditt, T. Myelinated mouse nerves studied by X-ray phase contrast zoom tomography. *J. Struct. Biol.* **192**, 561–568 (2015).

53. Kuan, A. T. *et al.* Dense neuronal reconstruction through X-ray holographic nano-tomography. *Nat. Neurosci.* **23**, 1637–1643 (2020).

54. Holler, M. *et al.* X-ray ptychographic computed tomography at 16 nm isotropic 3D resolution. *Sci. Rep.* **4**, 3857 (2014).

55. Holler, M. *et al.* High-resolution non-destructive three-dimensional imaging of integrated circuits. *Nature* **543**, 402–406 (2017).

56. Faulkner, H. M. L. & Rodenburg, J. M. Movable Aperture Lensless Transmission Microscopy: A Novel Phase Retrieval Algorithm. *Phys. Rev. Lett.* **93**, 4 (2004).

57. Guizar-Sicairos, M. *et al.* Phase tomography from x-ray coherent diffractive imaging projections. *Opt. Express* **19**, 21345–21357 (2011).

58. Guizar-Sicairos, M. *et al.* Quantitative interior x-ray nanotomography by a hybrid imaging technique. *Optica* **2**, 259–266 (2015).

59. Diaz, A. *et al.* Three-dimensional mass density mapping of cellular ultrastructure by ptychographic X-ray nanotomography. *J. Struct. Biol.* **192**, 461–469 (2015).

60. Anonymous Reviewer *et al.* Author response: Recreating the synthesis of starch granules in yeast. doi:10.7554/eLife.15552.024.

61. Shahmoradian, S. H. *et al.* Three-Dimensional Imaging of Biological Tissue by Cryo X-Ray Ptychography. *Sci. Rep.* **7**, 6291 (2017).

62. Holler, M. *et al.* OMNY—A tOMography Nano crYo stage. *Rev. Sci. Instrum.* **89**, 043706 (2018).

63. Kremers, G.-J., Gilbert, S. G., Cranfill, P. J., Davidson, M. W. & Piston, D. W. Fluorescent proteins at a glance. *J. Cell Sci.* **124**, 157–160 (2011).

64. Shu, X. *et al.* A Genetically Encoded Tag for Correlated Light and Electron Microscopy of Intact Cells, Tissues, and Organisms. *PLoS Biol.* **9**, e1001041 (2011).

65. Manning, C. F., Bundros, A. M. & Trimmer, J. S. Benefits and Pitfalls of Secondary Antibodies: Why Choosing the Right Secondary Is of Primary Importance. *PLoS ONE* **7**, e38313 (2012).

66. Lam, S. S. *et al.* Directed evolution of APEX2 for electron microscopy and proximity labeling. *Nat. Methods* **12**, 51–54 (2015).

67. Emre, M. *et al.* Clinical diagnostic criteria for dementia associated with Parkinson's disease. *Mov. Disord.* **22**, 1689–1707 (2007).

68. Braak, H., Alafuzoff, I., Arzberger, T., Kretzschmar, H. & Del Tredici, K. Staging of Alzheimer disease-associated neurofibrillary pathology using paraffin sections and immunocytochemistry. *Acta Neuropathol. (Berl.)* **112**, 389–404 (2006).

69. Thal, D. R. The Development of Amyloid beta Protein Deposits in the Aged Brain. *Sci. Aging Knowl. Environ.* **2006**, re1–re1 (2006).

70. Braak, H., Ghebremedhin, E., Rüb, U., Bratzke, H. & Del Tredici, K. Stages in the development of Parkinson's disease-related pathology. *Cell Tissue Res.* **318**, 121–134 (2004).

71. McKeith, I. G. *et al.* Diagnosis and management of dementia with Lewy bodies: Third report of the DLB consortium. *Neurology* **65**, 1863–1872 (2005).

72. Rutala, W. A. & Weber, D. J. Guideline for Disinfection and Sterilization of Prion-Contaminated Medical Instruments. *Infect. Control Hosp. Epidemiol.* **31**, 107–117 (2010).

73. Holler, M. *et al.* OMNY PIN—A versatile sample holder for tomographic measurements at room and cryogenic temperatures. *Rev. Sci. Instrum.* **88**, 113701 (2017).

74. Tokuyasu, K. T. Application of cryoultramicrotomy to immunocytochemistry. *J. Microsc.* **143**, 139–149 (1986).

75. Peters, P. J., Bos, E. & Griekspoor, A. Cryo-Immunogold Electron Microscopy. *Curr. Protoc. Cell Biol.* **30**, (2006).

76. Huang, X. *et al.* Optimization of overlap uniformness for ptychography. *Opt. Express* **22**, 12634–12644 (2014).

77. Guizar-Sicairos, M. *et al.* High-throughput ptychography using Eiger: scanning X-ray nano-imaging of extended regions. *Opt. Express* **22**, 14859–14870 (2014).

78. Thibault, P. *et al.* High-Resolution Scanning X-ray Diffraction Microscopy. *Science* **321**, 379–382 (2008).

79. Thibault, P. & Guizar-Sicairos, M. Maximum-likelihood refinement for coherent diffractive imaging. *New J. Phys.* **14**, 063004 (2012).

80. Wakonig, K. *et al. PtychoShelves* , a versatile high-level framework for high-performance analysis of ptychographic data. *J. Appl. Crystallogr.* **53**, 574–586 (2020).

81. Diaz, A. *et al.* Quantitative x-ray phase nanotomography. *Phys. Rev. B* **85**, 020104 (2012).

82. van Heel, M. & Schatz, M. Fourier shell correlation threshold criteria. *J. Struct. Biol.* **151**, 250–262 (2005).

83. FEARNLEY, J. M. & LEES, A. J. AGEING AND PARKINSON'S DISEASE: SUBSTANTIA NIGRA REGIONAL SELECTIVITY. *Brain* **114**, 2283–2301 (1991).

84. García-Cabezas, M. Á., John, Y. J., Barbas, H. & Zikopoulos, B. Distinction of Neurons, Glia and Endothelial Cells in the Cerebral Cortex: An Algorithm Based on Cytological Features. *Front. Neuroanat.* **10**, (2016).

85. Fields, R. D. Myelin Formation and Remodeling. *Cell* **156**, 15–17 (2014).

86. Kuusisto, E., Parkkinen, L. & Alafuzoff, I. Morphogenesis of Lewy Bodies: Dissimilar Incorporation of α-Synuclein, Ubiquitin, and p62. *J. Neuropathol. Exp. Neurol.* **62**, 1241–1253 (2003).

87. Doorn, K. J. *et al.* Increased Amoeboid Microglial Density in the Olfactory Bulb of Parkinson's and Alzheimer's Patients. *Brain Pathol.* **24**, 152–165 (2014).

88. Tokuyasu, K. T. Immunochemistry on ultrathin frozen sections. *Histochem. J.* **12**, 381–403 (1980).

89. Peters, P. J. & Pierson, J. Chapter 8 Immunogold Labeling of Thawed Cryosections. in *Methods in Cell Biology* vol. 88 131–149 (Elsevier, 2008).

90. Zucca, F. A. *et al.* Neuromelanin organelles are specialized autolysosomes that accumulate undegraded proteins and lipids in aging human brain and are likely involved in Parkinson's disease. *Npj Park. Dis.* **4**, (2018).

91. Ettle, B., Schlachetzki, J. C. M. & Winkler, J. Oligodendroglia and Myelin in Neurodegenerative Diseases: More Than Just Bystanders? *Mol. Neurobiol.* **53**, 3046–3062 (2016).

92. Brück, D., Wenning, G. K., Stefanova, N. & Fellner, L. Glia and alpha-synuclein in neurodegeneration: A complex interaction. *Neurobiol. Dis.* **85**, 262–274 (2016).

93. Wakabayashi, K., Hayashi, S., Yoshimoto, M., Kudo, H. & Takahashi, H. NACP/alpha-synuclein-positive filamentous inclusions in astrocytes and oligodendrocytes of Parkinson's disease brains. *Acta Neuropathol. (Berl.)* **99**, 14–20 (2000).

94. Braak, H., Sastre, M. & Del Tredici, K. Development of α-synuclein immunoreactive astrocytes in the forebrain parallels stages of intraneuronal pathology in sporadic Parkinson's disease. *Acta Neuropathol. (Berl.)* **114**, 231–241 (2007).

95. Song, W. *et al.* The Parkinson disease-associated A30P mutation stabilizes α-synuclein against proteasomal degradation triggered by heme oxygenase-1 over-expression in human neuroblastoma cells. *J. Neurochem.* **110**, 719–733 (2009).

96. Bartzokis, G. Age-related myelin breakdown: a developmental model of cognitive decline and Alzheimer's disease. *Neurobiol. Aging* **25**, 5–18; author reply 49-62 (2004).

97. Rosas, H. D. *et al.* Diffusion tensor imaging in presymptomatic and early Huntington's disease: Selective white matter pathology and its relationship to clinical measures. *Mov. Disord.* **21**, 1317–1325 (2006).

98. Bartzokis, G. *et al.* Myelin Breakdown and Iron Changes in Huntington's Disease: Pathogenesis and Treatment Implications. *Neurochem. Res.* **32**, 1655–1664 (2007).

99. Todorich, B., Pasquini, J. M., Garcia, C. I., Paez, P. M. & Connor, J. R. Oligodendrocytes and myelination: The role of iron. *Glia* **57**, 467–478 (2009).

100. Puntarulo, S. Iron, oxidative stress and human health. *Mol. Aspects Med.* **26**, 299–312 (2005).

101. Grune, T., Jung, T., Merker, K. & Davies, K. J. A. Decreased proteolysis caused by protein aggregates, inclusion bodies, plaques, lipofuscin, ceroid, and 'aggresomes' during oxidative stress, aging, and disease. *Int. J. Biochem. Cell Biol.* **36**, 2519–2530 (2004).

102. Ward, R. J., Zucca, F. A., Duyn, J. H., Crichton, R. R. & Zecca, L. The role of iron in brain ageing and neurodegenerative disorders. *Lancet Neurol.* **13**, 1045–1060 (2014).

103. Braak, H., Rüb, U., Schultz, C. & Tredici, K. D. Vulnerability of cortical neurons to Alzheimer's and Parkinson's diseases. *J. Alzheimers Dis.* **9**, 35–44 (2006).

104. Braak, H. & Tredici, K. D. Potential Pathways of Abnormal Tau and α-Synuclein Dissemination in Sporadic Alzheimer's and Parkinson's Diseases. *Cold Spring Harb. Perspect. Biol.* **8**, a023630 (2016).

105. Simons, M. & Nave, K.-A. Oligodendrocytes: Myelination and Axonal Support. *Cold Spring Harb. Perspect. Biol.* **8**, a020479 (2016).

106. Bradl, M. & Lassmann, H. Oligodendrocytes: biology and pathology. *Acta Neuropathol. (Berl.)* **119**, 37–53 (2010).

107. Deng, J. *et al.* X-ray ptychographic and fluorescence microscopy of frozen-hydrated cells using continuous scanning. *Sci. Rep.* **7**, 445 (2017).

108. Howells, M. R. *et al.* An assessment of the resolution limitation due to radiation-damage in X-ray diffraction microscopy. *J. Electron Spectrosc. Relat. Phenom.* **170**, 4–12 (2009).

109. Eriksson, M., Veen, J. F. van der & Quitmann, C. Diffraction-limited storage rings – a window to the science of tomorrow. *J. Synchrotron Radiat.* **21**, 837–842 (2014).

110. Studer, D. *et al.* Capture of activity-induced ultrastructural changes at synapses by high-pressure freezing of brain tissue. *Nat. Protoc.* **9**, 1480–1495 (2014).

111. Anderson, J. P. *et al.* Phosphorylation of Ser-129 is the dominant pathological modification of alpha-synuclein in familial and sporadic Lewy body disease. *J. Biol. Chem.* **281**, 29739–29752 (2006).

112. Taylor, A. M. *et al.* A microfluidic culture platform for CNS axonal injury, regeneration and transport. *Nat. Methods* **2**, 599–605 (2005).

113. Moutaux, E., Charlot, B., Genoux, A., Saudou, F. & Cazorla, M. An integrated microfluidic/microelectrode array for the study of activity-dependent intracellular dynamics in neuronal networks. *Lab. Chip* **18**, 3425–3435 (2018).

114. Moutaux, E. *et al.* Neuronal network maturation differently affects secretory vesicles and mitochondria transport in axons. *Sci. Rep.* **8**, 13429 (2018).

115. Virlogeux, A. *et al.* Reconstituting Corticostriatal Network on-a-Chip Reveals the Contribution of the Presynaptic Compartment to Huntington's Disease. *Cell Rep.* **22**, 110–122 (2018).

116. Gladkov, A. *et al.* Design of Cultured Neuron Networks in vitro with Predefined Connectivity Using Asymmetric Microfluidic Channels. *Sci. Rep.* **7**, 15625 (2017).

117. Malishev, E. *et al.* Microfluidic device for unidirectional axon growth. *J. Phys. Conf. Ser.* **643**, 012025 (2015).

118. Lassus, B. *et al.* Glutamatergic and dopaminergic modulation of cortico-striatal circuits probed by dynamic calcium imaging of networks reconstructed in microfluidic chips. *Sci. Rep.* **8**, 17461 (2018).

119. Renault, R., Durand, J.-B., Viovy, J.-L. & Villard, C. Asymmetric axonal edge guidance: a new paradigm for building oriented neuronal networks. *Lab. Chip* **16**, 2188–2191 (2016).

120. Studer, D., Humbel, B. M. & Chiquet, M. Electron microscopy of high pressure frozen samples: bridging the gap between cellular ultrastructure and atomic resolution. *Histochem. Cell Biol.* **130**, 877–889 (2008).

121. McDonald, K. L. & Auer, M. High-Pressure Freezing, Cellular Tomography, and Structural Cell Biology. *BioTechniques* **41**, 137–143 (2006).

122. Tsang, T. K. *et al.* High-quality ultrastructural preservation using cryofixation for 3D electron microscopy of genetically labeled tissues. *eLife* **7**, e35524 (2018).

123. Plattner, H. & Bachmann, L. Cryofixation: A Tool In Biological Ultrastructural Research. in *International Review of Cytology* vol. 79 237–304 (Elsevier, 1982).

124. Studer, D., Graber, W., Al-Amoudi, A. & Eggli, P. A new approach for cryofixation by high-pressure freezing. *J. Microsc.* **203**, 285–294 (2001).

125. Blancard, C. & Salin, B. Plunge Freezing: A Tool for the Ultrastructural and Immunolocalization Studies of Suspension Cells in Transmission Electron Microscopy. *J. Vis. Exp. JoVE* (2017) doi:10.3791/54874.

126. Sun, R. *et al.* An efficient protocol of cryo-correlative light and electron microscopy for the study of neuronal synapses. *Biophys. Rep.* **5**, 111–122 (2019).

127. Liu, Y.-T., Tao, C.-L., Lau, P.-M., Zhou, Z. H. & Bi, G.-Q. Postsynaptic protein organization revealed by electron microscopy. *Curr. Opin. Struct. Biol.* **54**, 152–160 (2019).

128. Fernández-Busnadiego, R. *et al.* Insights into the molecular organization of the neuron by cryo-electron tomography. *J. Electron Microsc. (Tokyo)* **60**, S137–S148 (2011).

129. Tao, C.-L. *et al.* Differentiation and Characterization of Excitatory and Inhibitory Synapses by Cryo-electron Tomography and Correlative Microscopy. *J. Neurosci.* **38**, 1493–1510 (2018).

130. Tee, Y. H. *et al.* Cellular chirality arising from the self-organization of the actin cytoskeleton. *Nat. Cell Biol.* **17**, 445–457 (2015).

131. Strale, P.-O. *et al.* Multiprotein Printing by Light-Induced Molecular Adsorption. *Adv. Mater.* **28**, 2024–2029 (2016).

132. Engel, L. *et al.* Extracellular matrix micropatterning technology for whole cell cryogenic electron microscopy studies. *J. Micromechanics Microengineering* **29**, 115018 (2019).

133. Engel, L. *et al. Lattice micropatterning of electron microscopy grids for improved cellular cryo-electron tomography throughput*. http://biorxiv.org/lookup/doi/10.1101/2020.08.30.272237 (2020) doi:10.1101/2020.08.30.272237.

134. Toro-Nahuelpan, M. *et al.* Tailoring cryo-electron microscopy grids by photo-micropatterning for in-cell structural studies. *Nat. Methods* **17**, 50–54 (2020).

135. Walther, P. *et al.* STEM tomography of high-pressure frozen and freeze-substituted cells: a comparison of image stacks obtained at 200 kV or 300 kV. *Histochem. Cell Biol.* **150**, 545–556 (2018).

136. Watanabe, S. Flash-and-Freeze: Coordinating Optogenetic Stimulation with Rapid Freezing to Visualize Membrane Dynamics at Synapses with Millisecond Resolution. *Front. Synaptic Neurosci.* **8**, (2016).

137. Walther, P. & Ziegler, A. Freeze substitution of high-pressure frozen samples: the visibility of biological membranes is improved when the substitution medium contains water. *J. Microsc.* **208**, 3–10 (2002).

138. Lucas, M. S., Günthert, M., Bittermann, A. G., de Marco, A. & Wepf, R. Correlation of live-cell imaging with volume scanning electron microscopy. *Methods Cell Biol.* **140**, 123–148 (2017).

139. Schindelin, J. *et al.* Fiji: an open-source platform for biological-image analysis. *Nat. Methods* **9**, 676–682 (2012).

140. Heiligenstein, X. *et al.* The CryoCapsule: Simplifying correlative light to electron microscopy. *Traffic Cph. Den.* **15**, 700–716 (2014).

141. Santarella-Mellwig, R. *et al.* Correlative Light Electron Microscopy (CLEM) for Tracking and Imaging Viral Protein Associated Structures in Cryo-immobilized Cells. *J. Vis. Exp.* 58154 (2018) doi:10.3791/58154.

142. Kim, E., Kim, J.-Y. & Choi, H. An SU-8-based microprobe with a nanostructured surface enhances neuronal cell attachment and growth. *Micro Nano Syst. Lett.* **5**, (2017).

143. Weigel, S. *et al.* Surface Microstructures on Planar Substrates and Textile Fibers Guide Neurite Outgrowth: A Scaffold Solution to Push Limits of Critical Nerve Defect Regeneration? *PLoS ONE* **7**, e50714 (2012).

144. Seven, F. *et al.* Guiding neural extensions of PC12 cells on carbon nanotube tracks dielectrophoretically formed in poly(ethylene glycol) dimethacrylate. *RSC Adv.* **10**, 26120–26125 (2020).

145. Vitzthum, L. *et al.* Study of Na+/H+ exchange-mediated pHi regulations in neuronal soma and neurites in compartmentalized microfluidic devices. *Integr Biol* **2**, 58–64 (2010).

146. Park, J. W., Vahidi, B., Taylor, A. M., Rhee, S. W. & Jeon, N. L. Microfluidic culture platform for neuroscience research. *Nat. Protoc.* **1**, 2128–2136 (2006).

147. Zhou, T. *et al.* Neurons derived from PC12 cells have the potential to develop synapses with primary neurons from rat cortex. 9.

148. Wiatrak, B., Kubis-Kubiak, A., Piwowar, A. & Barg, E. PC12 Cell Line: Cell Types, Coating of Culture Vessels, Differentiation and Other Culture Conditions. *Cells* **9**, 958 (2020).

149. Martorana, F. *et al.* Differentiation by nerve growth factor (NGF) involves mechanisms of crosstalk between energy homeostasis and mitochondrial remodeling. 16 (2018).

150. Mahoney, M. J., Chen, R. R., Tan, J. & Mark Saltzman, W. The influence of microchannels on neurite growth and architecture. *Biomaterials* **26**, 771–778 (2005).

151. Dunn, G. A. & Heath, J. P. A new hypothesis of contact guidance in tissue cells. *Exp. Cell Res.* **101**, 1–14 (1976).

152. Blom, H. *et al.* Spatial Distribution of DARPP-32 in Dendritic Spines. *PLOS ONE* **8**, e75155 (2013).

153. Knott, G., Marchman, H., Wall, D. & Lich, B. Serial Section Scanning Electron Microscopy of Adult Brain Tissue Using Focused Ion Beam Milling. *J. Neurosci.* **28**, 2959–2964 (2008).

154. Narayan, K. & Subramaniam, S. Focused ion beams in biology. *Nat. Methods* **12**, 1021–1031 (2015).

155. Xu, C. S. *et al.* Enhanced FIB-SEM systems for large-volume 3D imaging. *eLife* **6**, e25916 (2017).

156. Varapnickas, S., Žukauskas, A., Brasselet, E., Juodkazis, S. & Malinauskas, M. Chapter 12.1 - 3D microoptics via ultrafast laser writing: Miniaturization, integration, and multifunctionalities. in *Three-Dimensional Microfabrication Using Two-Photon Polymerization (Second Edition)* (ed. Baldacchini, T.) 445–474 (William Andrew Publishing, 2020). doi:10.1016/B978-0-12-817827-0.00012-6.

157. Braun, A. & Maier, S. A. Versatile Direct Laser Writing Lithography Technique for Surface Enhanced Infrared Spectroscopy Sensors. *ACS Sens.* **1**, 1155–1162 (2016).

158. Guijt, R. M. & Breadmore, M. C. Maskless photolithography using UV LEDs. *Lab. Chip* **8**, 1402–1404 (2008).

159. Ito, K. *et al.* MPP+ induces necrostatin-1- and ferrostatin-1-sensitive necrotic death of neuronal SH-SY5Y cells. *Cell Death Discov.* **3**, 17013 (2017).

160. Risiglione, P. *et al.* High-Resolution Respirometry Reveals MPP+ Mitochondrial Toxicity Mechanism in a Cellular Model of Parkinson's Disease. *Int. J. Mol. Sci.* **21**, 7809 (2020).

161. Zeng, X. *et al.* An In Vitro Model of Human Dopaminergic Neurons Derived from Embryonic Stem Cells: MPP+ Toxicity and GDNF Neuroprotection. *Neuropsychopharmacology* **31**, 2708–2715 (2006).

162. Peng, J., Liu, Q., Rao, M. S. & Zeng, X. Using Human Pluripotent Stem Cell–Derived Dopaminergic Neurons to Evaluate Candidate Parkinson's Disease Therapeutic Agents in MPP^+ and Rotenone Models. *J. Biomol. Screen.* **18**, 522–533 (2013).

163. Guo, X. *et al.* Hydralazine Protects Nigrostriatal Dopaminergic Neurons From MPP+ and MPTP Induced Neurotoxicity: Roles of Nrf2-ARE Signaling Pathway. *Front. Neurol.* **10**, (2019).

164. Schwarz, H. & Humbel, B. M. Correlative Light and Electron Microscopy Using Immunolabeled Resin Sections. in *Electron Microscopy: Methods and Protocols* (ed. Kuo, J.) 229–256 (Humana Press, 2007). doi:10.1007/978-1-59745-294-6_12.

165. Flechsler, J. *et al.* 2D and 3D immunogold localization on (epoxy) ultrathin sections with and without osmium tetroxide. *Microsc. Res. Tech.* **83**, 691–705 (2020).

166. Lucocq, J. Quantitation of gold labelling and antigens in immunolabelled ultrathin sections. *J. Anat.* **184**, 1–13 (1994).

167. Yoshimura, T. *et al.* GlcNAc6ST-1 regulates sulfation of N -glycans and myelination in the peripheral nervous system. *Sci. Rep.* **7**, 42257 (2017).

168. Takeda, A. *et al.* Microglia mediate non-cell-autonomous cell death of retinal ganglion cells. *Glia* **66**, 2366–2384 (2018).

169. Thai, T. Q. *et al.* Rapid specimen preparation to improve the throughput of electron microscopic volume imaging for three-dimensional analyses of subcellular ultrastructures with serial block-face scanning electron microscopy. *Med. Mol. Morphol.* **49**, 154–162 (2016).

170. Nguyen, H. B. *et al.* Conductive resins improve charging and resolution of acquired images in electron microscopic volume imaging. *Sci. Rep.* **6**, 23721 (2016).

171. Hayworth, K. J. *et al.* Imaging ATUM ultrathin section libraries with WaferMapper: a multi-scale approach to EM reconstruction of neural circuits. *Front. Neural Circuits* **8**, (2014).

172. Lattner, A. D., Miene, A. & Herzog, O. A Combination of Machine Learning and Image Processing Technologies for the Classification of Image Regions. in *Adaptive Multimedia Retrieval* (eds. Nürnberger, A. & Detyniecki, M.) 185–199 (Springer, 2004). doi:10.1007/978-3-540-25981-7_13.

173. Sharma, A., Gupta, A. & Jaiswal, V. Solving Image Processing Critical Problems Using Machine Learning. in *Machine Learning for Intelligent Multimedia Analytics: Techniques and Applications* (eds. Kumar, P. & Singh, A. K.) 213–248 (Springer, 2021). doi:10.1007/978-981-15-9492-2_11.

174. Horwath, J. P., Zakharov, D. N., Mégret, R. & Stach, E. A. Understanding important features of deep learning models for segmentation of high-resolution transmission electron microscopy images. *Npj Comput. Mater.* **6**, 108 (2020).

175. Masubuchi, S. *et al.* Deep-learning-based image segmentation integrated with optical microscopy for automatically searching for two-dimensional materials. *Npj 2D Mater. Appl.* **4**, 3 (2020).

176. Zhou, T., Ruan, S. & Canu, S. A review: Deep learning for medical image segmentation using multi-modality fusion. *Array* **3–4**, 100004 (2019).

177. Erickson, B. J., Korfiatis, P., Akkus, Z. & Kline, T. L. Machine Learning for Medical Imaging. *RadioGraphics* **37**, 505–515 (2017).

178. Ming, Y., Hasan, M. F., Tatic-Lucic, S. & Berdichevsky, Y. Micro Three-Dimensional Neuronal Cultures Generate Developing Cortex-Like Activity Patterns. *Front. Neurosci.* **14**, 563905 (2020).

179. Chen, C., Rengarajan, V., Kjar, A. & Huang, Y. A matrigel-free method to generate matured human cerebral organoids using 3D-Printed microwell arrays. *Bioact. Mater.* **6**, 1130–1139 (2021).

180. Jeong, G. S., Jun, Y., Song, J. H., Shin, S. H. & Lee, S.-H. Meniscus induced self organization of multiple deep concave wells in a microchannel for embryoid bodies generation. *Lab. Chip* **12**, 159–166 (2011).

181. Shi, M. *et al.* Glia Co-Culture with Neurons in Microfluidic Platforms Promotes the Formation and Stabilization of Synaptic Contacts. *Lab. Chip* **13**, 3008–3021 (2013).

182. Raimondi, I., Tunesi, M., Forloni, G., Albani, D. & Giordano, C. 3D brain tissue physiological model with co-cultured primary neurons and glial cells in hydrogels. *J. Tissue Eng.* **11**, 2041731420963981 (2020).